Purdue University
Purdue e-Pubs

Department of Electrical and Computer Engineering Technical Reports | Department of Electrical and Computer Engineering

10-1-1984

Amorphous Silicon Thin Film Transistor Fabrication and Models

G. W. Neudeck
Purdue University

Zhi Li
Purdue University

T. C. Lee
Purdue University

Follow this and additional works at: https://docs.lib.purdue.edu/ecetr

Neudeck, G. W.; Li, Zhi; and Lee, T. C., "Amorphous Silicon Thin Film Transistor Fabrication and Models" (1984). *Department of Electrical and Computer Engineering Technical Reports.* Paper 528.
https://docs.lib.purdue.edu/ecetr/528

This document has been made available through Purdue e-Pubs, a service of the Purdue University Libraries. Please contact epubs@purdue.edu for additional information.

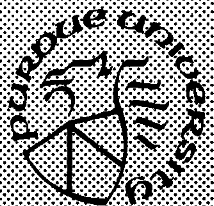

Amorphous Silicon Thin Film Transistor Fabrication and Models

G.W. Neudeck
Zhi Li
T.C. Lee

TR-EE 84-44
October 1984

School of Electrical Engineering
Purdue University
West Lafayette, Indiana 47907

Partial support by NSF-MRL and Delco Electronics

AMORPHOUS SILICON THIN FILM TRANSISTOR FABRICATION AND MODELS

by

G. W. Neudeck

Zhi Li

T. C. Lee

TR-EE 84-44

October 1984

Partial Support by NSF-MRL and Delco Electronics

TABLE OF CONTENTS

Page

LIST OF TABLES v

LIST OF FIGURES vi

ABSTRACT x

CHAPTER 1 - INTRODUCTION 1

1.1 Definition of Amorphous Semiconductors 2
1.2 Fabrication of Amorphous Silicon 4
1.3 Purpose of the Report 9
1.4 Organization of This Report 12

CHAPTER 2 - REVIEW OF THE LITERATURE 14

2.1 Amorphous Silicon : Structure, Density of State Model, Hopping Conduction in Localized States at the Fermi Energy 15
[A] Structure 15
[B] Density of States (DOS) Models 20
[C] Hopping Conduction in Localized States at the Fermi Energy ... 25
2.2 Reduction of the Localized States in the Pseudogap 27
[A] Thermal Annealing and Crystallization 28
[B] Passivation with Dangling Bond Terminators 30
2.3 Hydrogen in Amorphous Silicon 32
[A] Preparation of Hydrogenated Amorphous Silicon 32
[B] Content and Stability of Hydrogen in the Amorphous Silicon 34
[C] The Role of Hydrogen 35
[D] Structure of Hydrogenated Amorphous Silicon 38
2.4 Doping of Amorphous Silicon 41
2.5 Theoretical Analysis of Field Effect Conductance Modulation 43
[A] Space Charge Region 46
[B] Relation between the Band Bending and the Gate Voltage 47
[C] Conductance Modulation 50

Page

2.6 Major Applications of Amorphous Silicon 52
[A] Amorphous Silicon Solar Cells 53
[B] Amorphous Silicon Thin Film Transistors 56
[C] Amorphous Silicon Image Sensors 62
[D] Amorphous Silicon Charge Coupled Devices 64

CHAPTER 3 - EXPERIMENTAL PROCEDURES 67

3.1 Sample Preparation 70
[A] Substrate Fabrication 70
[B] Amorphous Silicon Film Fabrication 73
I. Evaporation Facilities 73
II. Film Evaporation Procedures 78
[C] Drain and Source Contacts 80
3.2 Experiment Measurements 82
3.3 Field Effect Measurements 85
3.4 Hydrogen Ion Implantation and Thermal Activation 88

CHAPTER 4 - EXPERIMENTAL RESULTS AND ANALYSIS . OF THE DATA 90

4.1 Results of Some Experiment Measurements 93
4.2 Amorphous Silicon with Vacuum Annealing and Theamal Etching at 400°C 98
4.3 Hydrogenation Implants versus Nonhydrogenation 102
4.4 Field Effect Conductance Change after Hydrogenation 105
4.5 Influence of Implantation Dosage on the Reduction of Localized States 108
4.6 Hydrogen Effusion 116
4.7 Effect of Pre-Implant in situ Thermal Annealing on the Reduction of Localized States 119
4.8 Some Discussions on Surface States 126

CHAPTER 5 - A-SI:H TFT 129

5.1 General Analysis for Characteristics of A-Si:H TFT 130
5.1.1 General Expression for Drain Current 130
5.1.2 Determination of the Electric Field Strength partion u(x,y)/partionx 133
5.1.3 Determination of Surface Potention u^s (y) 134
5.1.4 Localized State Density Distribution N(E) 135

Page

5.2 Approximate Analysis for Characteristics of A-Si:H TFT 137
5.2.1 Simple Theory 137
5.2.2 An Approximative Theoretical Analysis 138
[A] Uniform Localized State Density Distribution Case 139
[B] Exponential Localized-State-Density Distribution case 141
5.3 Experimental Results 147
5.4 Discussion of Results 157

CHAPTER 6 - CONCLUSIONS AND RECOMMENDATION FOR FUTURE RESEARCH 160

6.1 Conclusions 160
6.2 Recommendations for Future Research 162

LIST OF REFERENCES 165

APPENDICES 185

Appendix 1 185
Appendix 2 186

LIST OF TABLES

Table | Page

4.1 Summary of fabrication parameters and Density of Localized States near the Fermi level of a-Si samples 115b

4.2 Summary of effects of *in situ* thermal anneal and hydrogen implant dosage on the Density of Localized States of a-Si samples 125

LIST OF FIGURES

Figure Page

1.1 Experimental Setup for Post-Hydrogenation of CVD A-Si Films 8

2.1 First neighbor peak of the radial distribution function for evaporated a-Si and glow discharged a-Si:H 16

2.2 A continuous random network (CRN) model of a-Si containing a dangling bond 18

2.3 Hypothetical construction of an a-Si lattice showing the existence of a lone broken bond 18

2.4 Schematic representation of possible defects in crystalline (top) and amorphous silicon (bottom) 19

2.5 Density of states in the conduction band of a noncrystalline material, showing the band tailing states 22

2.6 Schematic density of states diagrams for amorphous semiconductors (a) the CFO model, (b) the Davis-Mott model 23

2.7 Band tail overlapping of CFO model 23

2.8 Variation of spin density in evaporated a-Si versus deposition temperature (T_s) or annealing temperature (T_A) 29

2.9 Temperature dependence of conductivity for undoped glow discharged specimen (i) after crystallization, (ii) results of Pearson and Bardeen 29

2.10 Bond pattern (a) before, and (b) after introduction of a pair of hydrogen atoms 30

2.11 A localized center giving a single level in the gap.

Figure Page

The addition of an other electron makes a bonding or antibonding level which lies outside of the gap. 36

2.12 Local Si-H vibrations for SiH, SiH_2, and SiH_3 groups 39

2.13 Two dimensional sketches of structural models for a-Si:H. The H atoms are denoted by hollow circles, and Si by solid circles.....40

2.14 Simplified CFO model.....44

2.15 Band diagram for the surface of the amorphous material near the insulator with a positive gate voltage.....45

2.16 Schematic diagram of various solar cell structure.....55

2.17 Cross section and top views of a completed a-Si TFT.....57

2.18 (a) Equivalent circuit of TFT-aided LCD picture element, (b) picture element layout for TFT-aided LCD.....59

2.19 Thin film transistor in the inverted gate configuration. The channel length is L and the channel width is Z.....60

2.20 The schematic of a dual-gate a-Si:H TFT.....60

2.21 The cross-sectional view of a fabricated E/D inverter.....61

2.22 An equivalent circuit of the proposed E/D type inverter.....61

2.23 The transfer characteristics of the E/D type inverter.....61

2.24 The unit cell structure of a proposed a-Si image sensor.....63

2.25 Equivalent circuit of the unit cell of the a-Si image sensor.....63

2.26 The cross-sectional view of a proposed a-Si CCD's with a four phase clock pulse.....65

2.27 Schematic motion of electrons in the proposed a-Si CCD's (a) electrode A at a high level, (b) both electrodes A and B

Figure Page

are at a high level, (c) B remains at a high level while A falls to a low level 65

3.1 Cross section of a field effect structure with a buried N^+ layer as a gate 68

3.2 Cross section of an inverted gate field effect structure 69

3.3 Capacitance-voltage plot for the bias temperature (BT) stressing test of a MOS capacitor, 33*-(3) : (1) initial curve, (2) after 5 min., @+35 V, 150°C BT stressing, (3) after 5 min., @-35 V, 150°C BT stressing 72

3.4 Schematic representation of vacuum evaporation apparatus 74

3.5 Identification of parts of the E-gun source 77

3.6 An interdigital finger pattern for field effect measurements 83

3.7 Circuit used for field effect measurements 87

4.1 Schematic representation of the locations of eight devices on a wafer 92

4.2 X-xay Diffraction Patten of : a) 9 Micron A-Si Film Deposited on Ag coated Quartz Substrate, b) Ag Coated Quartz Substrate 94

4.3 Residual Gas Analysis: (a) Before Evaporation, (b) During the Annealing Cycle 96

4.4 Effect of Annealing on the Conductance Change due to Field Effect 99

4.5 Source-Drain Current as A Function of Time with and without Thermal Etching 100

4.6 Field Effect Conductance Change with and without Thermal Etching101

4.7 Field effect data of nonhydrogenated device 31*-(2)-[8] and hydrogenated device 31*-(2)-[3] with implant dosage $5x10^{16}/cm^2$ 103

Figure | Page

4.8 Field effect data of device 37*-(1)-[3] with hydrogen implant dosage $1.5 \times 10^{17}/cm^2$ 106

4.9 Effect of four different ion implantation dosage of hydrogen on field effect curves in amorphous silicon 109

4.10 Flow chart of computer program to analyze field effect data....114

4.11 Effect of ion implantation dosage of hydrogen on density of localized states near E_F of amorphous silicon thin film 115

4.12 Field effect curves of three devices with fixed thermal activation temperature (230°C) but different annealing times of 1, 2, and 4 hours 117

4.13 Field effect data of two devices with same implantation dosage ($1 \times 10^{17}/cm^2$) but different thermal activation temperature (230°C and 290°C) 118

4.14 Field effect data for three devices with the same implant dosage ($5 \times 10^{16}/cm^2$) but with different *in situ* thermal annealing conditions....121

4.15 Field effect data of device 39*-(2)-[3] 123

4.16 Density of localized states in the band gap for film 39*-(2)-[3] after hydrogenated to a dose of $1 \times 10^{17}/cm^2$....124

4.17 Surface states distribution at the Si-SiO_2 interface of a MOS capacitor, 33*-(3) 128

5.1 Schematic Diagram of an A-Si:H TFT....131

5.2 Experimental and Calculated Drain Characteristics for an A-Si TFT 148

5.3 The Drain Current vs Gate Voltage for Fixed Values of V_D 149

5.4 The Drain Characteristics for Sample S52....151

5.5 Experimental Drain Current vs Gate Voltage for Sample 30*-(1)-[1], V_D=1.5V....152

Figure Page

5.6 Experimental and Calculated[eq.(5.3.2)] Drain Characteristics for Sample 30^*-(1)-[1], V_D=10 to 100V 153

5.7 Experimental and Calculated[eq.(5.3.2)] Drain Characteristics for Sample 30^*-(1)-[1], V_D=1 to 10V 154

5.8 Experimental and Calculated[eq.(5.3.3)] Drain Characteristics for Sample 30^*-(1)-[1], V_D=10 to 100V 155

5.9 Experimental Drain Characteristics for Sample 30^*-(1)-[1], $V_G < V_{th}$ 155b

5.10 Drain Current vs Gate Voltage for Two Samples: A, From Reference 141;B, For Sample 39^*-(2)-[3] 157

ABSTRACT

One of the primary purposes of this research was to develop techniques to improve the quality of vacuum evaporated amorphous silicon (a-Si), i.e. lower the density of localized states in the mobility gap. The electron beam evaporation of amorphouss silicon and hydrogenation by ion implanting has proved promising. This technique permits independent control of amorphous silicon disorder and the hydrogenation level, thereby separating the process of hydrogenation from that of film deposition. Electrical measurement of field effect conductance changes was used as a probing tool to monitor changes in the properties of a-Si before and after hydrogenation. Field effect data was transcribed by a computer program to determine the density of localized states.

Amorphous silicon films were prepared by electron beam evaporation of a high purity silicon onto the surface of a thermally oxidized crystalline silicon substrate. The films were deposited at a fixed rate in a high vacuum. Immediately after deposition, some films were subjected to *in situ* thermal anneal and some films were not. A comparison of the results of these two cases revealed the porous nature of evaporated a-Si. Hydrogen incorporation into a-Si films was performed by ion implantation followed by a low temperature thermal activation of the hydrogen.

After hydrogenation, a field effect conductance change of four orders of magnitude was observed on the devices which were not *in situ* thermally annealed. A comparison before and after hydrogenation demonstrates that almost three orders of magnitude reduction (from about 10^{22} to about 10^{19}/cm^3-eV) in the density of localized states near the Fermi level (N_T^F) was achieved. Varying the hydrogen implantation dosage between 1×10^{16} to 1.5×10^{17}/cm^2, with all other sample preparation procedures fixed, caused a decrease in N_T^F from 8.6×10^{20} to 1×10^{19}/cm^3-eV.

The effect of *in situ* thermal annealing prior to hydrogen implantation was also investigated. By performing a 400°C anneal for four hours immediately following film deposition the film porosity was greatly reduced. The film was then implanted with hydrogen to a total dose of 1×10^{17}/cm^2. A field effect conductance change of six orders of magnitude was observed which yielded a N_T^F of 4×10^{17}/cm^3-eV, approaching that of glow discharge produced films.

The second purpose of the research was to develop modeling techniques for the a-Si:H TFT. Despite rapid progress in the TFT performence, the theoretical basis to determine static- and dynamic-characteristics of TFTs has not yet been determined mainly because the influence of the localized states on TFT operation is very complicated.

The theoretical expression of drain current as a function of gate bias and drain voltage was derived. To use the theoretical expressions, the localized state density distribution N(E) must be known. A derived yet practical formula for the N(E) did not exist. A common way is to use the experiment of field effect conductance change to determine the N(E). With the data theoretical expressions the localized state density N(E) could be calculated by using a numerical technique, but it is cumbersome and connot be determined uniquely.

As a design tool for devices and circuits, a simple theory which can express concisely the TFT characteristics is very important. In this report, several models for N(E) are listed. Approximate analyses for characteristics of a-Si:H TFT are derived. In two special cases, i.e. uniform localized state density distribution and exponential localized distribution, some useful approximate expressions was obtained. Compared with the experiment data, the uniform density distribution of localized state model is a good approximate expression for alarge density discribution of localized states near Fermi level. The exponential model is a good approximate expression for lower density distribution of localized states near Fermi level.

CHAPTER 1

INTRODUCTION

We live in an electronic era of technological advances based to a large extent on crytalline semiconductor devices. The marvels of modern semiconductor technology follow from sound physical knowledge and metallurgical control of single crystal materials. While semiconductor phenomena are not unique to crystals, active devices almost always involve single crystals. Amorphous semiconductors, with the well-established crystalline foundations as a departure point, offer new frontiers for research and hopefully, promise for technological developments.

Considerable effort has been expended in trying to understand and predict the electronic, optical, and physical properties of amorphous semiconductors. Remarkable progress has been made in these areas, interrelating the basic characteristics and in some instances applying the results in the realization of device technologiss. Its potential application is in producing large area, low cost solar cells for energy conversion. Other a-si devices recently explored are thin film transisters[1-4], charge coupled devices(CCD)[5], image sensors[6], and

liquid crystal dispay(LCD) driver devices[3,4].

1.1 Definition of Amorphous Semiconductors

The mechanisms involved in the formation of crystalline or noncrystalline states by condensation from vapor and liquid phases primarily depend on the time that atoms or clusters of atoms interact to from bonds in metastable and stable structures. Crystallization is the long-range ordering of atoms in a periodic solid-phase lattice near equilibrium conditions. Amorphous and polycrystalline semiconductors are noncrystalline.

Amorphous semiconductors are noncrystalline, but crystalline state bonds still predominate in amorphous solids. They lack long-range periodic ordering of their constituent atoms. That is not to say that amorphous semiconductors are completely disordered on the atomic scale. Local chemistry provides almost rigorous bond-length, and to a lesser extent, band-angle constraints on the nearest-neighbor environment. Amorphous semiconductors contain covalently bonded atoms arranged in an open network with correlations in ordering up to the third or fourth nearest neighbors, ie they have short-range order. The short-range order is directly responsible for observable semiconductor properties such as optical absorption edges and activated electrical conductivities.

Amorphous semiconductors are not polycrystalline materials. Polycrystalline semiconductors are composed of grains with each grain containing a periodic arry of atoms surrounded by a layer of interconnective or

boundary atoms. The grains, or crystallines, are formed by independent nucleation and growth processes randomly oriented and spaced with respect to one another. An amorphous semiconductor can be transformed to the polycrystalline state, but not the reverse. The irreversibility indicates that the crystalline state has a lower lattice energy. Indeed, the polycrystalline state, too, will transform to a single-crystal state by the reduction of internal surface(grain boundary) energy. We can also infer that the transition from amorphous to polycrystalline state occurs by the reduction of internal surface energy. Howeever, in both case the internal surfaces are reduced or minimized, but not necessarily eliminated.

Amorphous semicondutors, while forming a single area of study with some unifying ideas, often is divided into two subfields, the tetrahedrally coordinated silicon-like materials and the chalcogenide glasses. Arsenic, from column 5 of the periodic table, forms a bridge between the two classes of materials.

The terms "glassy" or "vitreous" are often used synonymously for "amorphous" or "noncrystalline". However, in some fields of study, glassy or vitreous connotes the technical preciseness of a definable thermodynamic phase. The existence of a glass state, with its glass transition temperature, has been documented for some chalcogenides, but not for the tetrahedrally bonded amorphous semiconductors. For chalcogenide glasses, this is reflected in the ability to prepare them from a semicondutor melt by rapid cooling(quenching) to temperatures below the glass transition temperature. For silicon and the like, quenching from the melt, which in this case is metallic with a different short-range order then the desired semiconductor, generally cannot be done rapidly enough to freeze in an amorphous atomic arrangement. polycrystallinity is the more common result.

Once prepared, a material is empirically defined to be amorphous if its diffraction patten consists of diffuse ring(halos) rather then sharply defined Bragy ring or spots characteristic of polycrystalline or single crystal solids. While mixtures of amorphous and crystalline materials can exist, there does not seem to be a continuous transition from one to the other. The conversion from amorphous to crystalline takes place by nucleation and growth rather then by homogeneous atomic rearrangement.

1.2 Fabrication of Amorphous Silicon

Amorphous semiconductors that cannot be prepared dirctly from the melt are usually fabricated in the form of thin films by an atomic deposition procedure such as vacuum evaporation, sputtering, chemical vapor deposition, plasma decomposition of gases, or electroplating. Ion bombardment of crystals is also used to leave an amorphous layer in the collision train of the ions.

The electrical and optical properties of the materials are directly influenced by the density of the localized elctronic states[7], which differentiates amorphous silicon from crystalline silicon. A prerequisite for fabricating successful devices in a-si is to have a low density of localized states, otherwise the Fermi level is pinned or nearly pinned at a fixed energy level.

It is known that hydrogenated amorphous silicon films(a-Si:H) have a lower density of localized states in the mobility gap[8] then non-hydrogenated films. Consequently the technigues of hydrogen incorporation and the effects of

hydrogen in reducing the localized states are of considerable interest and have been the main stream of basic materials research in a-si.

Hydrogenated amorphous silicon was first deposited from a glow discharge in silane(SiH_4) generated by an external r-f coil[9]. These r-f electrodeless discharge systems usually operate within a frequency range of 0.5—13.5 MHz and at SiH_4 pressures of 0.1—0.2 torr. The discharge chambers are generally small(on the order of 7 cm in diameter), and the samples are usually positioned horizontally on a heated pedestal. The best quality film are abtained with substrate temperatures in the range of 200° — 400°C. The SiH_4 flow rates are typically in the range of 0.2—5.0cm^3/min, and the deposition rates are usually in the range of 100 — 1000 Å/min. The deposition rate increases rapidly with increasing power and pressure, but the film quality starts to degrade at high deposition rates. These r-f electrodeless systems have the advantage of external electrodes, so that contamination of the films by sputtering is minimized. However, these systems are relatively small, and the uniformity of the film is generally poor.

Radio frequency capacitive discharge systems employ parallel plate electrodes inside the discharge chamber and are similar to the systems used for sputter-deposition[10]. The capasitive discharge systems generally operate at 13.5 MHz and at SiH_4 pressures in the range of 5—250 mtorr. The film uniformity is excellent, and some systems can accommodate substrates 1 ft^2 in area. The SiH_4 flow rates are typically 10—50 cm^3/min and depend on the size of the system as well as on the pressure and power. The power densities are usually in the range of 0.1—2.0 W/cm^2, and the deposition rates are in the range of 50—500Å/min.

Deposition of a-Si:H has also been done by means of a DC glow discharge in SiH_4[11]. Deposition rates in the range of 0.1—1.0 μm/min cccan be obtained by varying the current density to a cathodic substrate from 0.2 to 2.0 mA/cm^2 in ~1.0 torr of SiH_4. Cathodis films are bombarded by energetic positive ions during the deposition, and bombardment damage can degrade the film quality at high voltages and low pressures. Film uniformity is good if the substrate dimensions are much larger than the Crookes dark space(a dark region in the glow discharge near the cathode).

Another technique that has been used to deposit a-Si:H is sputtering in an atmosphere of Ar and H_2[12]. In this approach a polycrystalline silicon target is sputtered in an r-f capasitive discharge system. The substrate is placed on a heated counterelectrode located opposite the target electrode. This technique has the advantage of being able to control the hydrogen content of the films by varying the partial pressure of H_2. However, preliminary results obtained at RCA Laboratories indicate that the film quality is inferior to that obtained in a SiH_4 discharge.

Chemical vapor deposition(CVD) has also been used to deposit a-Si:H. The non-doped CVD a-Si was deposited by thermal decomposition of SiH_4 at 550—600°C[13]. The CVD a-Si obtained exhibits no detectable vibrational absorption in the infrared due to Si-H bonds and incorporates silicon dangling bonds amounting to approximately $1x10^{19}$ cm^{-3}. When CVD a-Si:H films are deposited on a substrate at temperatures between 380 and 450°C in Si_2H_6[14], infrared transmission spectra showed the following results: (1) At lower temperature both SiH_2 and SiH bonds are evident. (2) As the temperature increases, SiH_2 bonds disappear and only SiH bonds remain. (3) From the IR spectra it appears that with increasing temperature the H content is reduced.

Post-hydrogenation of CVD a-Si can be used to eliminate the electron spin density, which implier bond-gap states. Annealing in a hydrogen plasma has been developed for CVD a-Si[15]. Undoped a-Si films were obtained by the chemical vapor deposition of SiH_4 at a temperature of 650° C. The experimental setup for hydrogen plasma annealing is shown in Figue 1.1 The pressure of hydrogen, the substrate temperature, r-f power, and annealing time were 0.6 Torr, 350° C, 40W(frequency : 13.56MHz), and 60 minutes, respectively. The hydrogen plasma was maintained until the substrate temperature fell below 250^0 C to avoid an effusion of the hydrogen atoms out of the films during cooling. The following conclusions are drawn on the results of post-hydrogenated CVD a-Si: (1) The electronic properties are closely connected with the hydrogen distribution, which is described by a complementary error function. (2) The hydrogen penetration depth is estimated to be 0.5 μ, where the spin density is reduced from $1x10^{19}$ cm^{-3} to $7x10^{16}$ cm^{-3}

Another important method to obtain a-Si is by electron-beam evaporation. The typical procedures are that the vacuum, substrate temperature and rate of evaporation are 10^{-8} torr, 200° C, and 1—5 Å/sec respectively. After a-Si is deposited, it is kept in a high vacuum(10^{-8} and annealed for 4 hours at 400° C. The density of localized state was measured to be $6x10^{19}/CM^3$—eV.

Hydrogened a-Si, made by electron beam evaporation, has been produced[16] by annealing in a hydrogen gas ambient at 400° C for 1 hour. This step has a decision benefit for the augmentation of the photovoltaic performance. On the other hand, by using hydrogen pplasma annealing as described in a-Si literature[17], nonone has been able to obtain the same degree of benefit. A point of departure in this approach is the use of molecular hydrogen instead of plasma[17], or atomic hydrogen[18] for hydrogenation. The

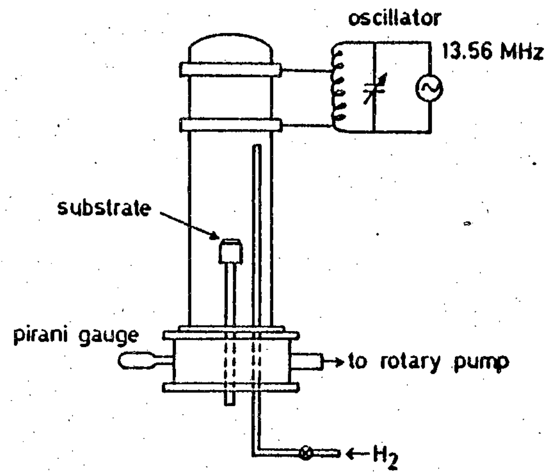

Figure 1.1 Experimental setup for post-hydrogenation of CVD a-Si films (from Reference 15)

hydrogen content after this annealing treatment is found to be, from nuclear reaction analysis[19],about 1 to 3% of the silicon content. This value is rather low in comparison with published data of as high as 30%[17]. Whether this low value is due to the hydrogenation being incomplete, or alternatively the a-Si has less defective states to bond with hydrogen, is an important problem.

1.3 Purpose of the Report

To date, the best device electrical performances have been achieved with glow discharge deposited a-Si:H films which have a low density of localized states in the energy gap [20-23]. Yet the properties of the deposited specimens are critically dependent on a number of variables such as substrate temperature, type of discharge, discharge power, SiH_4 pressure, and SiH_4 flow rate. Complex surface reactions which involve electrons and positive ion fragments such as SiH, SiH_2, and SiH_3 take place during film growth. This behavior indicates that the density of gap states is strongly influenced by the deposition conditions. Hydrogen incorporation by this method is determined by the detailed plasma conditions at the specimen surface during deposition. The inherent complexity of the glow discharge process and the interrelations among the deposition parameters make it difficult to study the basic material properties of films prepared by this technique. Because of such a complex deposition process, which interweaves with the reactor design or operating parameters, what critical specifications are needed to uniquely define a silane

decomposition system is still uncertain and unsolved. In another words, the experimental control of the plasma condition and surface reactions during deposition, to obtain well defined and reproducible electronic properties, remains a major problem. Hence the samples produced by this technique tend to have poor uniformity from run to run due to the complexity of the reaction process. Therefore it is not surprising that different characteristics of a-Si:H, produced by this method, are observed at different laboratories. For instance, Goodman [24] found that the density of localized states at the Fermi energy is lower when depositing at the substrate temperature (T_s) of 160°C than for the films depositing at T_s = 280°C. But the other published results indicates that 250°C $< T_s <$ 300°C is the optimum range for producing high quality films with a low density of localized states [8,25]. Even in the same Chicago group, Goodman's results [24] disagreed with Tsai's results [25] on the substrate temperature effect. Moreover, in the fabrication of a-Si:H films, two important factors, namely the degree of disorder and the hydrogen content cannot be independently controlled in glow discharge or sputter deposited films.

In this research a technique is reported for the deposition of a-Si and its subsequent hydrogenation, which permits independent control of a-Si disorder and the hydrogenation level. In addition, this technique serves to minimize the number of fabrication parameters thereby facilitating the study of hydrogenation phenomenon. With the number of fabrication parameters minimized, the technique is greatly simplified compared with the inherent complexity of the glow discharge process. Samples with excellent uniformity from device to device and from wafer to wafer were obtained. This uniformity will be demonstrated in the I_{DS} vs. V_G figures of Chapter 4.

The device structure used in this research is similar to the MOSFET with a thin film of amorphous silicon for the semiconductor which was produced by electron beam evaporation in a high vacuum. Hydrogen is incorporated into the film by ion implantation and therefore can be quantitatively controlled. This is followed by a low temperature thermal anneal to activate the implanted hydrogen. A comparison of electrical properties of the evaporated films before and after hydrogenation provides valuable information on the effects of hydrogenation, independent of deposition parameters. The hydrogen content can be easily controlled by this technique as compared to the technique involving exposure of evaporated a-Si to an atomic hydrogen plasma [26], glow discharge decomposition of silane [20-23], sputtering deposition in the presence of hydrogen [27], and chemical vapor deposition (CVD) [28].

The electrical properties of a-Si thin films produced by the above methods are heavily dependent upon the fabrication parameters [7] such as the deposition conditions, nature of the substrate, post-deposition heat treatments, and the hydrogenation techniques. Therefore it is necessary to determine what parts of the observed experiment are due to fabrication, what parts are intrinsic to amorphous materials, and what parts are due to hydrogenation effects. In this research all the fabrication conditions were fixed. Only the ion implantation dosage of hydrogen is varied once an annealing procedure is established.

The field effect measurement of the conductance change was employed in this research as a probing tool to study the characteristic changes of the a-Si upon hydrogenation. These measurements were performed on the devices which were subjected to a thermal anneal *in situ* immediately following a-Si film deposition and also on the devices which were not annealed *in situ*. Comparing

the results of these two cases gave valuable information about the porous nature of evaporated a-Si films and the effectiveness of the hydrogenation process. The effect of hydrogen in reducing the density of localized states was quantified by varying the implant dosage. Analyses of the field effect data indicated that the density of localized states near the Fermi level (N_t^F) decreased as the implant dosage was increased with all other experimental procedures fixed.

1.4 Organization of This Report

Chapter 2 presents a review of the relevant literature on a-Si and a-Si:H. The review includes a summary of generally known properties, hydrogenation, and doping of a-Si. The theoretical analysis of field effect conductance modulation and a brief discussion of the major applications of a-Si are also presented. Detailed experimental procedures are described in Chapter 3 which includes the sample preparation, field effect measurement procedures, ion implantation and thermal activation. Chapter 4 contains the experimental results of hydrogenation versus nonhydrogenation, field effect conductance change after hydrogenation, influence of implantation dosage on the reduction of localized states, hydrogen effusion, the effect of a pre-implant *in situ* thermal anneal on the reduction of localized states, and a discussion of surface states. In Chapter 5, the a-Si:H TFT is discussed, which includes the theoretical analysis, the approximative theoretical analysis, and a brief

discussion of some experiment results. Conclusions drawn from this research are in Chapter 6 which also includes some recommendations for future research. Two appendices are also included as part of this report. Appendix 1 presents the initial wafer cleaning procedures. Appendix 2 illustrates the procedures to run the computer program and the program which is used to determine the density of localized states in the mobility gap from experimental data.

CHAPTER 2

REVIEW OF THE LITERATURE

Prior to 1970, very little research was performed on amorphous materials. Since then more research has been involved in this field and most of the published results are experimentally oriented. Only few papers have dealt with any theoretical work. Up to the present a concise and complete theory of amorphous materials, which can explain all the observed experimental facts, has to be made available.

Several good reviews on amorphous semiconductors have been written by Davis and Mott [29], Adler [7], Knights and Lucovsky [30], or edited by Brodsky [31]. The review in this chapter is only concerned with the literature on amorphous silicon. The review includes some generally known properties of intrinsic a-Si, hydrogenated a-Si, doped a-Si, field effect conductance modulation, and a brief discussion of some major applications of a-Si.

2.1 Amorphous Silicon : Structure, Density of States Models, Hopping Conduction in Localized States at the Fermi Energy

[A] Structure

Silicon, an element in column IV of the periodic table, tends to bond tetrahedrally. In its lowest entropy state, silicon crystallizes in the "diamond" structure, in which it is most stable.

Amorphous semiconductors that cannot be prepared directly from melt-quenching are usually fabricated in the form of thin films by an atomic deposition procedure. Among the fabrication methods of amorphous semiconductors, several important and commonly used methods for the preparation of a-Si are vacuum evaporation, r.f. sputtering, chemical vapor deposition (CVD), and glow discharge decomposition of silane (SiH_4) gas. X-ray diffraction studies [32,33] have confirmed the amorphous nature of these films. Further studies of X-ray, electron, or neutron diffraction data [34-37] yield a radial distribution function (RDF), the Fourier transform of the scattered radiation, which is the average density of atoms at a given distance from any other reference atom. The RDF shows that the first interatomic distance and the coordination number in a-Si are of the tetrahedral arrangement. The average bond length is 2.38 Å as shown by Figure 2.1.

To date, the most widely accepted continuous random network model (CRN) of the ideal amorphous silicon structure is that of Polk [38]. The Polk model is a "ball and stick" model containing 440 atoms. Each atom in the model has four immediate neighbors arranged in a distorted tetrahedral geometry in the sense that bonds may be slightly bent or stretched. The short-

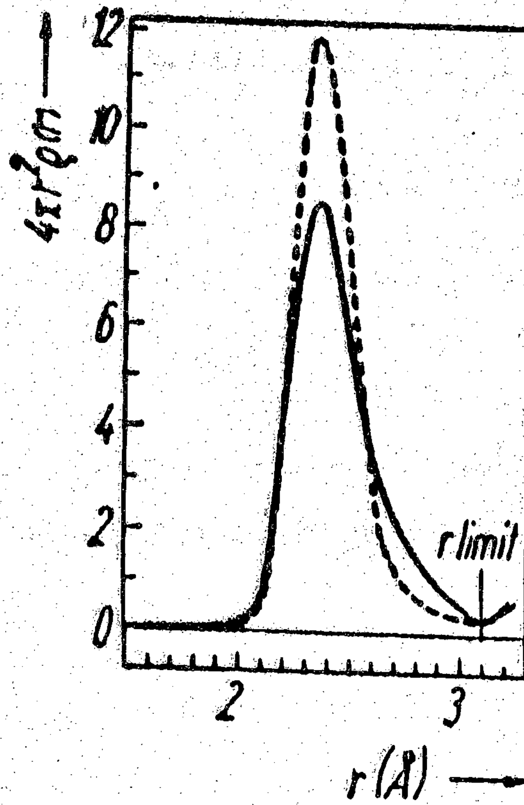

Figure 2.1 First neighbor peak of the radial distribution function for evaporated a-Si and glow discharged a-Si:H (from Reference 34)

range order is preserved to a distance of the first nearest neighbor. Beyond the second and third nearest neighbors, the structure gradually loses the long-range periodicity due to the slight bond stretching and bond angle deviation. In the model, the bond angles are distributed about their average value of $109^\circ 28'$ with an average deviation of $\pm 10^\circ$ and a maximum deviation of $\pm 20^\circ$. The maximum bond stretching is 16%. The density of this structure was found by Polk to be about 93% that of a corresponding crystal lattice. Available published densities [39] for amorphous and crystalline silicon are 2.35 and 2.42 gm/cm^3 respectively, yielding a density ratio of approximately 97%. In addition to the sixfold rings of crystalline silicon, the model also displays fivefold and sevenfold rings. Polk's model represents an ideal structure for the amorphous state, a low energy metastable structure which can be extended indefinitely with no internal unsatisfied bonds. It is a structure toward which fabricated amorphous films approach.

The above idealized network structure gives an image of no dangling bonds. Each atom is satisfied by its chemical valence bonding requirements. In the real world, defects (a lone broken bond or "dangling bond") always exist in amorphous materials. These imperfections exist even in the crystalline materials. Figure 2.2, 2.3, and 2.4 visualize the CRN model and some possible defects.

The a-Si films produced by vacuum evaporation method contain large numbers of voids, defects and other imperfections (thermal strains, density fluctuations) [12]. Evidence of the presence of microvoids in a-Si is found in the work of Moss and Graczyk [40] and also Brodsky [32]. Low angle electron scattering data of Moss and Graczyk clearly indicate the presence of voids in the films. Brodsky observed the large electron spin resonance (ESR) signal

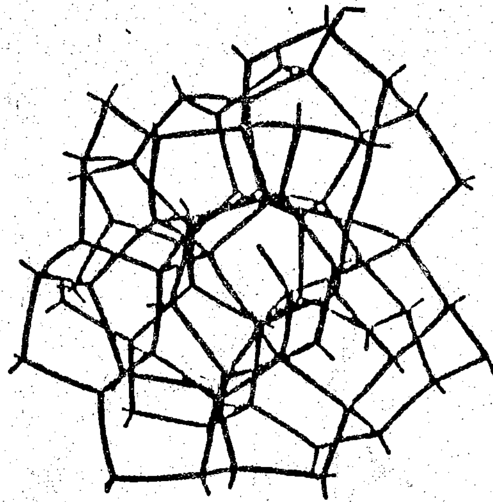

Figure 2.2 A continuous random network (CRN) model of a-Si containing a dangling bond (from Reference 31)

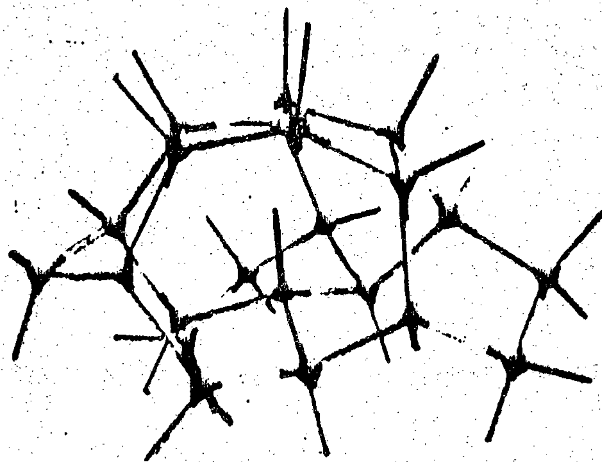

Figure 2.3 Hypothetical construction of an a-Si lattice showing the existence of a lone broken bond (from Reference 31)

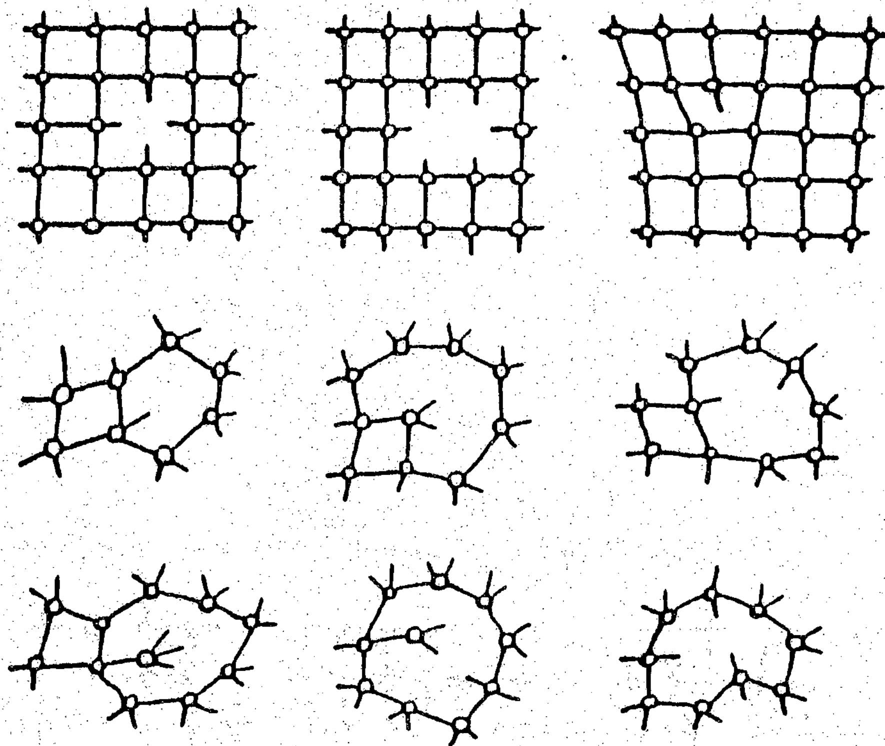

Figure 2.4 Schematic representation of possible defects in crystalline (top) and amorphous silicon (bottom) (from Reference 31)

which is attributed to the unpaired electron spins from dangling bonds on the void edges. There will be more discussions on the subject of microvoids in evaporated a-Si later in Chapter 4 section 4.6.

[B] Density of States (DOS) Models

Knowledge of the density of states function and the mobility of the states in amorphous materials is essential in the understanding of the electrical transport and other properties of these materials. A good introduction on the theory of electronic states in amorphous semiconductors was given by Kramer and Weaire [41], while an introduction to the localized states in the mobility gap and defects in amorphous semiconductors was written by Davis [42]. The whole subject of the theory of states in a-Si is still in its infancy. The purpose of this section is only to qualitatively review the important features of several density of states models.

Due to the absence of long range order in amorphous semiconductors, a rigorous quantitative solution of the Schrodinger equation does not exist. However, the model of "purely topological disorder", as represented by the Hamiltonian used by Thorpe and Weaire, allows a discussion of the behavior of bands and band gaps in tetrahedrally bonded amorphous semiconductors. The Anderson Hamiltonian represents "pure compositional disorder" and is the key model for the understanding of electron localization in disordered systems. Weaire and Thorpe [43,44] demonstrated that by quantum mechanically manipulating the matrix elements of the Hamiltonian, an energy gap exists in the "ideal" random structure which is defined as an amorphous solid with no

impurities, no defects, and no dangling bonds. However, due to the deviated distribution of the bond angles and interatomic distances, some kind of electronic energy states (so-called "intrinsic" states) do exist in the gap. These gap states are fewer in number but nonzero as compared with those in the conduction band and valence band in which are named extended states. The carrier mobility [45] in the gap states is far less (several orders of magnitude) than that in the extended states.

The energy separating the gap states and extended states is called the mobility edge, hence this pseudogap is named the mobility gap. The intrinsic gap states are believed to be the band tailing states prolonged from the extended states into the energy gap as Figure 2.5 illustrates. While based on Anderson's Localization Theory [46], Mott [47] also demonstrated that the spatial fluctuations in the potential caused by the configurational disorder in amorphous materials may lead to the formation of localized states which forms a tail above the valence and below the conduction bands.

As mentioned in the last section, fabricated a-Si films contain a large number of defects and dangling bonds which make them depart from an idealized structure and result in additional electronically active states in the pseudo energy gap. These defect-caused localized gap states are named "extrinsic" states to be distinguished from the band tailing-caused "intrinsic" states. The states in the pseudo energy gap are called localized in the sense that an electron placed in a region will not diffuse at zero temperature to other regions with corresponding potential fluctuations. Their quantum mechanical wave function has a finite region of influence as compared to an extended state.

Figure 2.6 illustrates two of the density of states models proposed for the band structure of amorphous semiconductors known as the Cohen-Fritzsche-

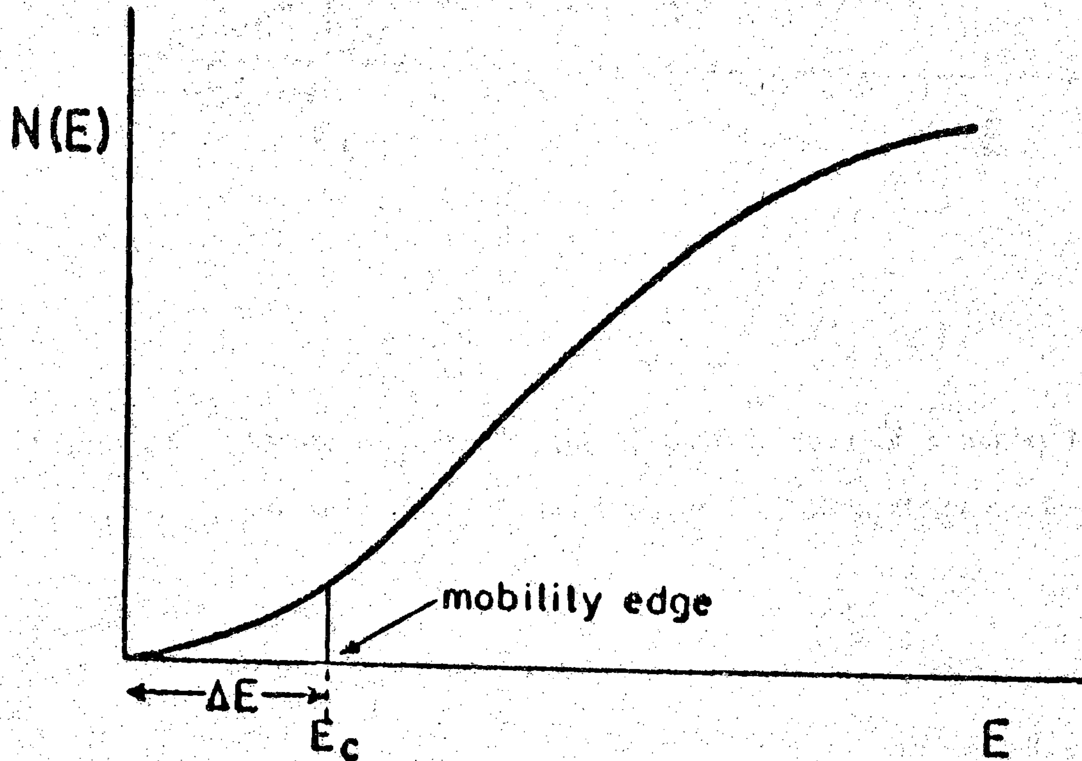

Figure 2.5 Density of states in the conduction band of a noncrystalline material, showing the band tailing states (from Reference 59)

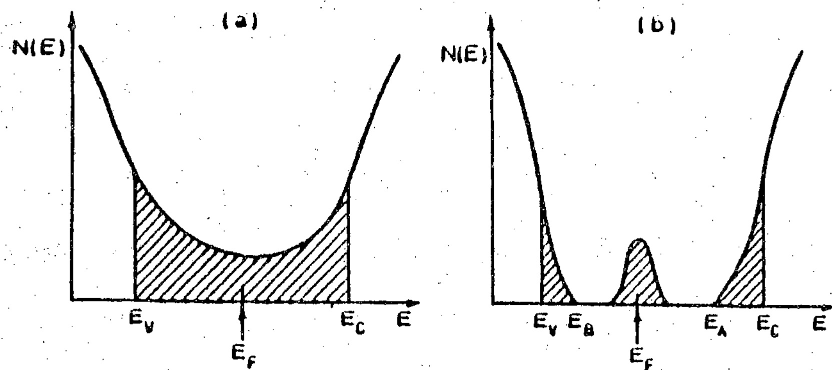

Figure 2.6 Schematic density of states diagrams for amorphous semiconductors (a) the CFO model, (b) the Davis-Mott model (from Reference 31)

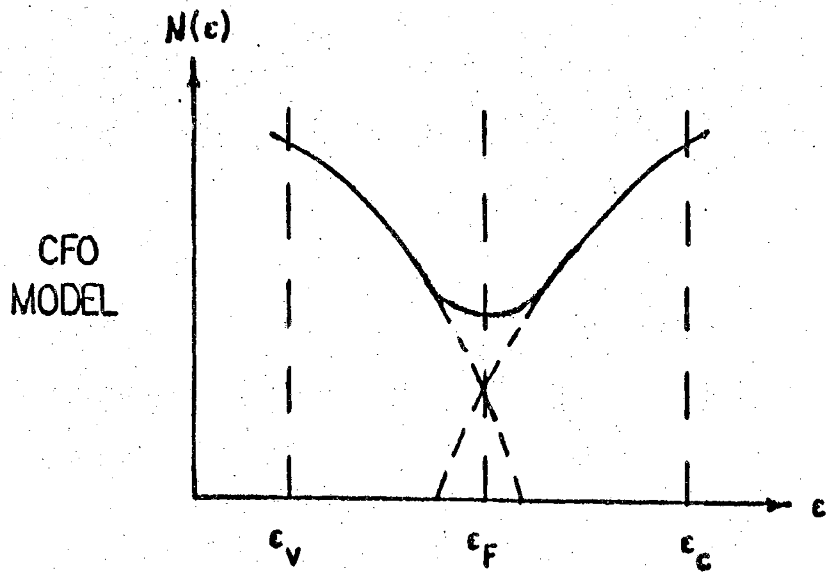

Figure 2.7 Band tail overlapping of CFO model

Ovshinsky model [48] (CFO model) and the Davis-Mott model [49]. Recently a different model, called the small-polaron model, was proposed by Emin [50]. It should be noted that preparation methods and conditions have been shown to have a great influence on the number of localized density of states in amorphous silicon [23,9,51,52]. All the experimental data obtained from field effect [8,23,53,54], noise [55], and photoconductivity measurement [56] support CFO model for amorphous silicon.

If the system disorder is sufficiently high, then the tail states of the conduction and valence bands extend so deep into the mobility gap that they eventually overlap each other. In the CFO model, the localized states are believed to be due to the overlapping of the conduction and valence band tails, leading to an appreciable density of states in the middle of the gap (see Figure 2.7). As a consequence of band overlapping, some electrons in the tail states of the valence band have higher energies than those from the tails of conduction band. Such electrons from the top of the tail states of valence band fall into the lower tail states of conduction band. The Fermi level, E_F, thus falls close to the middle of the quasi energy gap where the total density of states reaches the minimum value. Assume the tail states of the conduction band are of the acceptor type (i.e. neutral when empty and negatively charged when being filled), and the tail states of valence band are of the donor type (i.e. neutral when filled and positively charged when empty). The redistribution of the electrons mentioned above gives rise to the empty positive charges in the tails of valence band which are neutralized in equal number by the associated negative charges from the tail states of filled conduction band.

In the Davis-Mott model, the band tails are not extensive but rather narrow and extend only a few tenths of an electron volt into the quasi gap.

These localized states are associated with the absence of long-range order i.e. intrinsic states. Furthermore, there exists a band of compensated levels near the middle of the gap that can pin the Fermi level. This band, referred to as the J-band, originates from defects in the random network, e.g. dangling bonds, vacancies etc. Experimental data on chalcogenide glasses [57], which are amorphous materials involving S, Se, and Te, showed that Mott's model is preferable.

[C] Hopping Conduction in Localized States at the Fermi Energy

A short note should be made on the conduction in localized states near the Fermi energy which is unique in amorphous materials. The interpretation of electrical transport data is closely interwoven with the energy distribution of the density of states. On the basis of the CFO model, there can be two processes leading to conduction in amorphous semiconductors.

At elevated temperatures, charge carriers can be excited beyond the mobility edge into the extended states. The current transport in the extended states is similar to usual band conduction in crystalline semiconductors but with much smaller carrier mobilities compared with those of crystalline semiconductors.

At low but finite temperatures, the conduction mechanism is dominated by the low mobility hopping conduction in the localized states near the Fermi energy. The carriers can jump from localized sites to other sites through a phonon assisted tunneling process. This transport, known as "thermally activated hopping" or "variable range hopping" is similar to impurity band

conduction observed in heavily doped and highly compensated semiconductors at low temperatures [58]. A full and lengthy treatment on the temperature dependence of the hopping conductivity at E_F has been given by Mott [59] and a review article on this subject has recently been published by Overhof [60] and Nagels [61].

Later in Chapter 4, the analyses of the field effect experimental data on the "as-fabricated" films showed no field effect conductance changes. It is believed that hopping in localized states at E_F dominates the conduction mechanism in these cases. The hopping conduction formula derived by Mott will be used to estimate the initial density of states near E_F on the "as-fabricated" films. It must be mentioned that Mott's derivation implies a number of simplifying assumptions of which some are controversial. The final hopping conductivity (σ) derived by Mott [59] is cited as follows :

$$\sigma=\sigma_0(T)\exp(-A/T^{1/4})$$

where

$$\sigma_0(T)=\frac{e^2}{2(8\pi)^{1/2}}(\nu_{ph})[N(E_F)/\alpha kT]^{1/2}$$

$$A=2.1[\frac{\alpha^3}{kN(E_F)}]^{1/4}$$

ν_{ph} : phonon frequency $\sim 10^{13}$/sec

α : rate of fall-off of the wave function at a site

$\alpha^{-1} \sim 10$ Å

$N(E_F)$: density of states at the Fermi level

e : absolute value of electron charge, $1.6\text{x}10^{-19}$ coulombs

T : absolute temperature in Kelvin

k : Boltzmann's constant, 8.62×10^{-5} eV/°K

It should be noted that the temperature dependence of σ has been confirmed experimentally [59]. However many other functions also fit the data.

2.2 Reduction of the Localized States in the Pseudogap

As mentioned in the section 2.2[A], a large number of defects and dangling bonds exist in "intrinsic" amorphous silicon as indicated by a detectable electron spin resonance (ESR) signal. A dangling bond, with its electron energy level lying in between the valence states and conduction states, contributes to optical absorption and electrical conduction processes and hence masks many interesting semiconductor phenomena. Further, a large density of fast nonradiative recombination centers, originating from the mobility gap states, makes photoconductivity or photoluminescence uninterestingly small in pure amorphous silicon. Finally, the Fermi level can not be moved significantly due to the large number of gap states when conventional impurities (phosphorus or boron) are incorporated. In other words, we have serious difficulties in doping such defect-rich amorphous silicon. As indicated in Chapter 1, the gap states have to be reduced in order to improve the quality of a-Si films for device applications. In this section, two commonly used methods to reduce the gap states, namely thermal annealing and passivation with dangling bond terminators, are reviewed.

[A] Thermal Annealing and Crystallization

Traditional thermal annealing [53,54] has the effect of healing the dangling bonds, removing the voids and reducing the dislocations by reconstruction and rearrangement of the amorphous network. Therefore thermal annealing has the effect of reducing the "extrinsic" gap states. Annealing at elevated temperatures increases resistivity by orders of magnitude. The clearing up of the gap states by thermal annealing or with an elevated deposition temperature is also demonstrated by the reduction of ESR signals as Figure 2.8 shows. More recently it was established that under clean conditions without contaminates, the annealing effects are limited and that a-Si will crystalize before all the dangling bonds are removed [62]. Further discussion on removing the voids in evaporated a-Si by *in situ* thermal annealing immediately after film deposition is given in Chapter 4, section 4.6. Incidentally, Pierce and Spicer [51] determined the deposition conditions necessary for the fabrication of vacuum evaporated a-Si with a structure close to the ideal amorphous structure, which seems to exist though in concept only. These conditions include : 1) deposition pressure less than 5×10^{-6} torr, 2) evaporation rates in the range of 2 to 5 Å/sec, 3) large evaporator to substrate distance (greater than 20 cm.), and 4) annealing or deposition on a substrate maintained at an elevated temperature (within 100°C of the crystallization temperature). It should be pointed out that when the films are subjected to high temperature processing and if there is a thermal mismatch between the substrate and the film, then thermal strains can be left in the film.

In an even higher annealing temperature range, about 600°C to 700°C, the amorphous silicon will transform to a polycrystalline structure. The grain size in the polycrystalline structure increases with annealing temperature. Figure

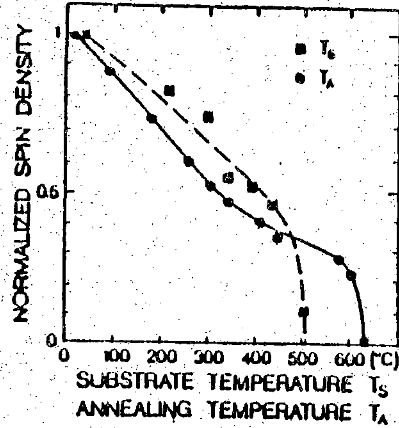

Figure 2.8 Variation of spin density in evaporated a-Si versus deposition temperature (T_s) or annealing temperature (T_A) (from Reference 31)

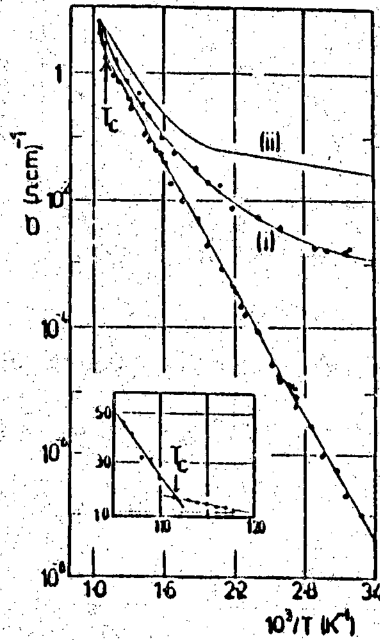

Figure 2.9 Temperature dependence of conductivity for undoped glow discharged specimen (i) after crystallization, (ii) results of Pearson and Bardeen (from Reference 31)

2.9 illustrates that the crystallization temperature is about 620°C. In these experiments, the temperature was raised from room temperature to about 700°C. The results show a well defined activation energy up to a temperature T_c indicated in the graph. More clearly shown by the inset, a discontinuity in gradient occurs at T_c. When heating to $T > T_c$, an irreversible change in the conductivity has been produced. Curve (i) in Figure 2.9 was obtained after heating the sample to 700°C and allowing it to cool. Conductivity has increased by over four orders of magnitude at room temperature and the X-ray pattern shows that the specimen has been crystallized. For comparison, curve (ii) was obtained by Pearson and Bardeen [63] on a specimen of polycrystalline silicon. Grigorovici [64] also reports that at high temperatures the thermoelectric effect in a-Si approaches the values of crystalline silicon. This indicates that the conduction process at high temperature is similar to that in the corresponding crystalline structure.

[B] Passivation with Dangling Bond Terminators

The electrical properties of a-Si prepared by vacuum evaporation [32,65] and inert gas (Argon) sputtering [32] were found to be similar [66] but were quite different from those prepared by the r.f. glow discharge decomposition of silane (SiH_4) gas [66-68]. Evaporated and sputtered films were found to have considerably lower room temperature d.c. resistivities than those of r.f. glow discharge films [66]. Also field effect measurements showed that glow discharge films have a density of gap states two or three orders of magnitude less than that found in evaporated and sputtered films. It is believed that during glow

discharge of silane gas, a substantial amount of hydrogen is incorporated into the a-Si film to form the silicon alloy or silicon matrix : $Si_{1-x}H_x$ (i.e. SiH, SiH_2 or SiH_3) [69-72]. The hydrogen atoms act as terminators to "passivate" the dangling bonds and hence provide a method to reduce the gap states other than thermal annealing. One disadvantage of hydrogenated a-Si is the hydrogen evolution when the film is thermally treated above 350°C, but below the crystallization temperature.

Besides hydrogen, several other species such as chlorine [73] and fluorine [74,75] have been considered as good candidates for terminators of dangling bonds. It is found that the bond energy of fluorine with silicon is about 1.6 times as large as that of hydrogen-silicon, which indicates that fluorine forms a single bond with silicon more tightly than hydrogen. More precisely, the bond strength of H-Si is 71.4 Kcal/mole and that of F-Si is 116 Kcal/mole [76]. Published reports [74,75] indicate that fluorine has remained in the a-Si film and kept their bonds with Si even after an annealing at 600°C (hence the name heat-resisting). In this sense, fluorine provides an alternative candidate for the dangling bond terminator which is more thermally stable than hydrogen.

A considerable amount of research effort has been centered on the hydrogenation of amorphous semiconductors. A good review on this subject was written by Knights and Lucovsky [30]. This subject, being the core of this research and report, is so important that it deserves a whole section.

2.3 Hydrogen in Amorphous Silicon

[A] Preparation of Hydrogenated Amorphous Silicon

The preparation techniques used to date to produce hydrogenated amorphous silicon fall into three broad classes : 1) Decomposition or reaction of a hydrogen-containing compound, 2) Addition of hydrogen during a physical deposition process, 3) Diffusion of hydrogen into a material deposited by some other technique.

In the first class, there includes glow-discharge (or plasma) decomposition of hydrides (silane), pyrolysis (thermal decomposition, similar to chemical vapor deposition) of hydrides, and reduction of halides. The amount of hydrogen in the deposited film is controlled by the reaction chemistry and is not an independent variable. Hence independent control of this property is not possible. Studies of the reactive species generated during the decomposition of silane [77] indicate that the dominant species in gas-phase reactions are the SiH, SiH_2, and SiH_3. Isolated silicon atoms are not present in any appreciable concentration. This is in strong contrast to the physical deposition techniques such as evaporation and sputtering that fall into the second class. In the plasma decomposition of silane method, substrates are typically placed on a surface whose temperature can be controlled within the range 25 to 600°C. Deposition reactor designs can be classified by the type of electrical excitation used; direct current (d.c.) or radio-frequency (r.f.). In the case of r.f. excitation, the reactor designs can further be classified by how the excitation is coupled into the plasma; inductive or capacitative. The growth of the films is expected to proceed through nucleation, growth, and coalescence of islands. The

deposition process is a surface reaction which is strongly affected by the deposition system parameters.

The second class comprises reactive sputtering and evaporation. In these techniques the hydrogen partial pressure at the growing surface can be controlled. The primary participants in deposition process are most probably atomic, e.g. silicon and hydrogen. In the method of reactive sputtering in hydrogen, both hydrogen partial pressure and argon pressure have been shown to be important variables in determining film properties [78]. Bias may also be a factor although little has been reported about its effect.

The third class of techniques involves the exposure of a predeposited thin film to atomic hydrogen. The major difference between this and the other classes is that the structure of the material is determined prior to hydrogenation. Independent control of hydrogen content can be achieved. Using films deposited in ultra high vacuum, Kaplan [26] exposed the deposited films to an atomic hydrogen plasma while the films were heated to 500 to 550°C. Pankove [79] rehydrogenated a plasma-deposited film from which most of the hydrogen had been driven off. Recovery of photoluminescence to ~50% of that of the original film was achieved. One limitation of the preparation method of class three seems to be the requirement that the material be heated, so that it is in an annealed state as it is being hydrogenated.

In this research, a new technique of hydrogenation is developed by ion implantation of hydrogen into a-Si produced by electron-beam vacuum evaporation. It allows independent control of hydrogen content and material disorder. This facilitates the study of the hydrogenation phenomenon. This preparation technique can be classified into class three. Since ion implantation is a low temperature process and the temperature of post-implant thermal

activation is only 230°C, the limitation of class three does not apply to this method.

[B] Content and Stability of Hydrogen in the Amorphous Silicon

By far the largest hydrogen content (~58 at.%) is found in plasma deposited material [80]. Hydrogen content in the film produced by this technique depends strongly upon the fabrication conditions, e.g. substrate temperature, r.f. power, and silane concentration etc. All these system parameters interweave to each other. The largest reported hydrogen content in reactive sputtering produced a-Si is 25 at.% [80]. This reflects primarily the fact that hydrogen has to be removed from the starting material in plasma deposition as opposed to being added in the other techniques.

Fritzsche and his coworkers [22,81] were first to investigate the stability of hydrogenated a-Si produced by plasma deposition. Using a hydrogen evolution technique they observed the following results. 1) Hydrogen did not effuse at temperatures below the deposition temperature. 2) Depending on the deposition parameters, the hydrogen could effuse out in two distinct temperature regions. One centered at approximately 350°C and the other at ~ 680°C just below the crystallization temperature. Fritzsche's group suggested that these results indicated two different environments for the hydrogen and proposed that these sites might be SiH_2 and SiH sites identified in Infrared Spectroscopy. There is some correlation between defect structures and hydrogen bonding configurations which will be further illustrated in section D. It seems likely from this and other observations [82] that defect structures may be the

strongest influence in evolution patterns.

Other researchers also observed the evolution phenomenon of hydrogen and the subsequent increase in the density of localized states in a-Si [82-84]. It was also observed that the de-hydrogenated a-Si film could be re-hydrogenated by exposing the de-hydrogenated film to a hydrogen plasma [26,69].

[C] The Role of Hydrogen

It is now widely recognized that a primary role for hydrogen in a-Si:H films is that of a defect "passivant". The hydrogen atoms act as terminators to "passivate" or "compensate" the dangling bonds in a-Si, hence reduce the density of localized states in the mobility gap [20,21,22]. Figure 2.10 and Figure 2.11 illustrate the role played by hydrogen in the passivation action.

Direct evidence of the neutralization of the dangling bonds by forming bonds with the hydrogen atoms is given by the disappearance of the ESR signal in hydrogenated a-Si as compared to pure amorphous silicon [85,86]. The ESR signal originates from the unpaired electrons which are produced by dangling bonds. An additional piece of direct evidence concerning the role played by hydrogen is from the work of Kaplan et al. [26] on hydrogenated a-Si which is produced by evaporation. By exposing the ultra high vacuum (UHV) evaporated amorphous silicon to an atomic hydrogen plasma, Kaplan demonstrated that hydrogen bonds with silicon in a single Si-H configuration that produces an ESR signal reduction very similar to that observed for hydrogenated material produced by sputtering. There is ample evidence that atomic hydrogen, by forming a bond with a dangling bond, is responsible for

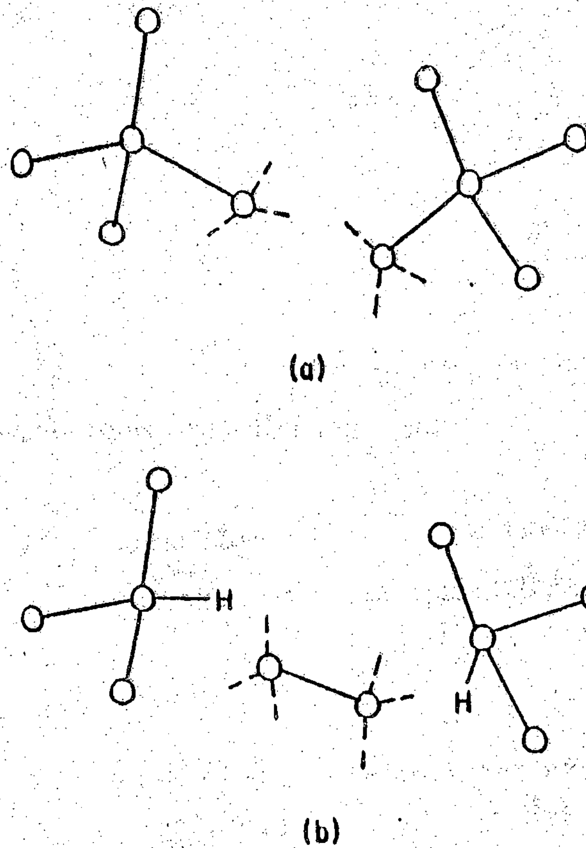

Figure 2.10 Bond pattern (a) before, and (b) after introduction of a pair of hydrogen atoms (from Reference 36)

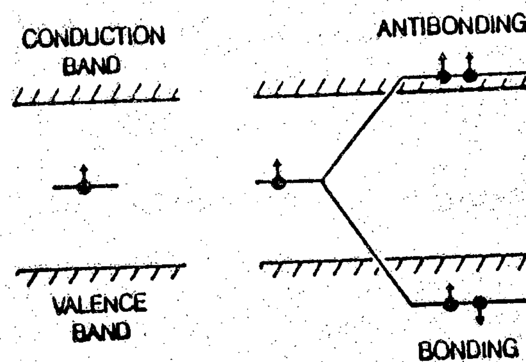

Figure 2.11 A localized center giving a single level in the gap. The addition of an other electron makes a bonding or antibonding level which lies outside of the gap. (from Reference 31)

the observed reduction of the electron spin density in amorphous silicon.

Effects consistent with the reduction of defect densities by hydrogen are widely observed in the transport properties of hydrogenated amorphous semiconductors. In evaporated or sputtered a-Si which is unhydrogenated, a combination of d.c. and a.c. conductivity measurements indicate that the primary conduction mechanism, at low temperatures, is variable range hopping in the localized states ($\sim 10^{20}$ /cm^3-eV) at the Fermi level [87]. The first report that hydrogen did in fact alter transport properties in an amorphous semiconductor was made by Lewis et al. [27,88]. As hydrogen was introduced to the sputtering gas, the room temperature conductivity of a-Ge films was found to drop by several orders of magnitude and the conductivity then showed an activated behavior consistent with carrier motion in extended states. This effect was attributed directly to the saturation of dangling bonds with hydrogen, thus removing localized states from the gap. Subsequently similar behavior has been reported by the Harvard group [89] for a-Si:H. Similar effects have also been reported for materials produced by d.c. reactive sputtering [90] and by plasma hydrogenation of evaporated films [26].

It is interesting to note that hydrogen, in addition to passivating gap states, also plays an active role in enlarging the quasi bandgap by alloying with Si [91]. Producing a-Si by sputtering in the presence of hydrogen gas, Anderson [89] was able to make a-Si:H films with activation energies as high as 0.95 ev. A number of studies have been centered on the properties of hydrogenated a-Si, including the thermally activated conductivity, optical absorption edge [92], photoluminescence [26,93], electroluminescence, and photoconductivity.

[D] Structure of Hydrogenated Amorphous Silicon

A comparative study of atomic scale structure for both a-Si and glow discharge produced a-Si:H has been done by Barna [94]. It was an electron diffraction study which showed that the radial distribution function (RDF) of a-Si is not drastically perturbed by the introduction of hydrogen, except that an additional peak at 5 Å was observed on a-Si:H. This peak also appears in RDF's of random network model structures. Therefore there is a higher degree of local order in the plasma deposited material than pure a-Si.

To investigate the local environments at the H sites, a number of groups [69-71] have studied the infrared absorption and Raman scattering of a-Si containing substantial amounts of bonded hydrogen. The material was described as a Si-H binary alloy, a-$Si_{1-x}H_x$. Spectroscopic studies of the local atomic structure in these binary alloys yield evidence for multiple as well as single H-atom attachment. Figure 2.12 illustrates the atomic motions of the vibrational modes used to investigate the structure of hydrogenated amorphous silicon. Films deposited on substrates held at 200°C or higher generally show absorptions and vibration modes corresponding to SiH, SiH_2, and $(SiH_2)_n$ groups, with no evidence for SiH_3. However, SiH_3 groups are clearly evident at samples produced on room temperature substrates.

Figure 2.13 further shows the sketches of a theoretical study by Chin et al.[95] on the bonding configurations in hydrogenated amorphous silicon. The H-bonding configurations considered include the following : 1) monohydride; SiH, 2) dihydride; SiH_2, 3) trihydride; SiH_3, 4) broken-bond model; a broken Si-Si bond with two H atoms inserted i.e. SiHHSi, 5) $(SiH_2)_2$; a special case of the polymeric form $(SiH_2)_n$, 6) bridge model; SiHSi, 7) ring-center model; H atom at the center of a six-member ring, 8) interstitial H atom. The method

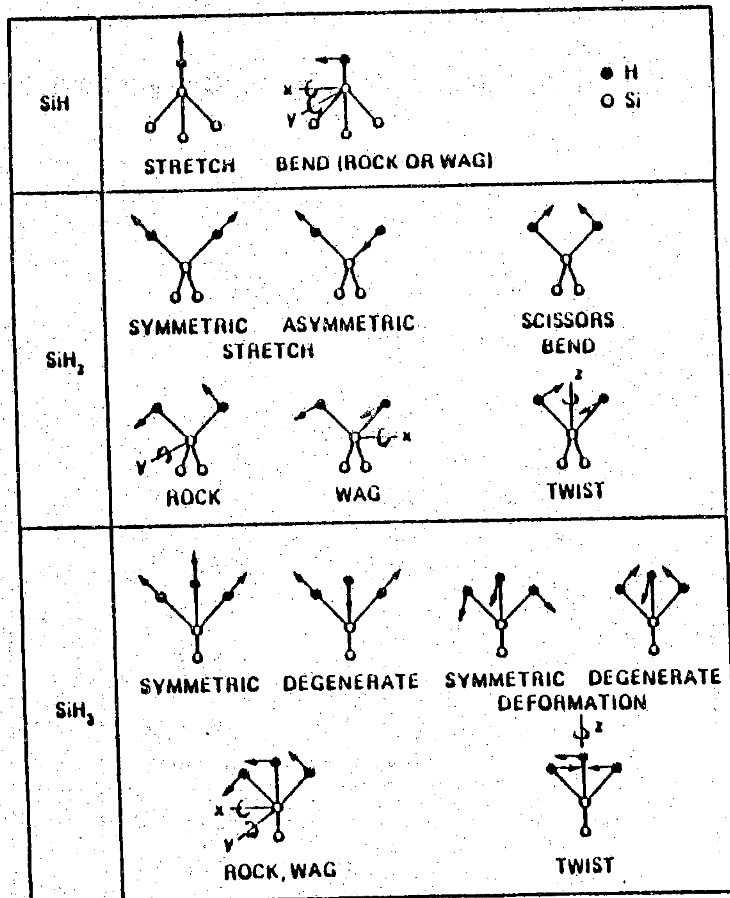

Figure 2.12 Local Si-H vibrations for SiH, SiH_2, and SiH_3 groups (from Reference 31)

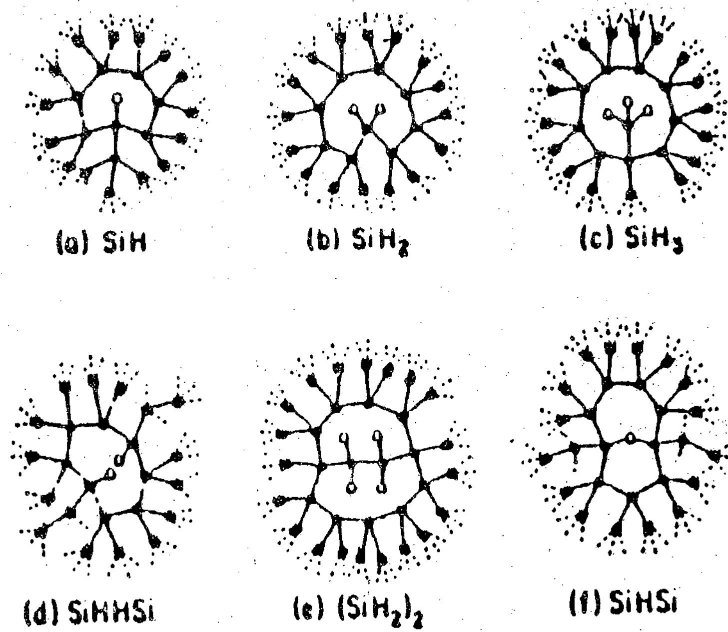

Figure 2.13 Two dimensional sketches of structural models for a-Si:H. The H stoms are denoted by hollow circles, and Si by solid circles. (from Reference 95)

they used is a linear combination of atomic orbitals (LCAO) for first principles calculation [96,97] of electronic energy of a-Si. The conclusions drawn from this study are as follows. In the cases of the SiH, SiH_2, SiH_3, SiHHSi and $(SiH_2)_2$ configurations, the theoretical results are consistent with the observed photoemission experiments. But a distinct discrepancy is found between theoretical results and photoemission spectra for the SiHSi bridge model, ring-center model, and the interstitial model. Therefore these three models are not appropriate for the major constituents in a-Si:H.

2.4 Doping of Amorphous Silicon

Based upon what was learned experimentally, it was established that with the incorporation of hydrogen into a-Si films, the density of localized states in the material could be reduced drastically. The next question to ask is the possibility of doping a-Si into n-type or p-type for solid state device applications, analogous to substitutional doping of crystalline silicon. Nonhydrogenated a-Si, prepared by sputtering or evaporation, usually possesses a large density of localized states, 10^{19} to $10^{20}/cm^3$-eV or greater. Even large densities of pentavalent or trivalent impurities would not move the Fermi level by more than a few kT [98], since any generated excess carriers would be absorbed by the defect states. In another words, the density of localized states is far too high to allow much change in the Fermi level position and consequently in the electrical properties. That is the reason for the insensitive

behavior to doping of nonhydrogenated a-Si produced by evaporation or sputtering method. However, glow discharge deposited films, with hydrogen incorporation, were shown to have low density of localized states, $10^{17}/cm^3$-eV or less [98]. Therefore it was possible to substitutionally dope a-Si prepared by the r.f. decomposition of silane.

Spear and LeComber [98] succeeded in demonstrating that in glow discharge produced a-Si the Fermi level could be moved from 0.6 to about 0.15 ev below conduction band by addition of a small amount of PH_3 gas to the SiH_4 source during the glow discharge deposition process with the substrate held at a temperature between 500 and 600°K. Meanwhile the Fermi level could be relocated to about 0.2 ev above valence band by adding diborane (B_2H_6) to the silane gas. They demonstrated that the "intrinsic" conductivity of about 10^{-12} mhos/cm can be increased to 10^{-2} mhos/cm on both the n-type and p-type materials.

By using mixtures of arsine and silane, Knights [10] showed that glow discharge deposited a-Si can also be doped with As donors. The Harvard group [99] showed that it is also possible to dope r.f. sputtered a-Si by the addition of either phosphine or diborane to the argon-hydrogen sputtering gas. In this way, the room temperature conductivity of films could be increased from 2×10^{-10} to 4×10^{-6} mhos/cm by adding phosphine.

Spear and LeComber [100] made a comment about the efficiency of gas phase doping in a-Si which concluded that about one third of the incorporated phosphorus atoms act as donors. Additional valence bonds of the remaining phosphorus atoms are most probably accommodated into the random network. The same seems to apply to doping with boron.

2.5 Theoretical Analysis of Field Effect Conductance Modulation

Field effect experiment measures the current change from the source to drain due to an applied transverse electrical field. This technique gives more detailed information about the distribution of localized states than other measurement techniques. In this section, the relationship between field effect conductance modulation and the density of localized states is reviewed. The review is based upon the theoretical analysis done by Neudeck and Malhotra [54] which includes several simplifying assumptions. In Chapter 4, section 4.4, a computer program [101,102] developed by the Chicago group is used to analyze the field effect experimental data. The theory behind this computer program is basically the same as that of Neudeck and Malhotra. However this computer program numerically solves Poisson's equation for a given density of states distribution, N(E), instead of using approximate solutions. The computer program also uses the finite temperature statistics on the Fermi-Dirac function. The method to run this cumbersome program is given in the Section 4.4 of Chapter 4 and also in Appendix 2.

The density of states model used for the analysis is shown in Figure 2.14 at 0°K. The choice of the type of states above and below E_F is arbitrary. Any combination of acceptor and donor states, which satisfies the charge neutrality condition will also give identical results. Figure 2.15 illustrates the energy band diagram with a positive gate voltage. Some definitions which are used in the calculations of the characteristics of the space charge in the semiconductor are given below :

1) x is the distance into the semiconductor from the semiconductor

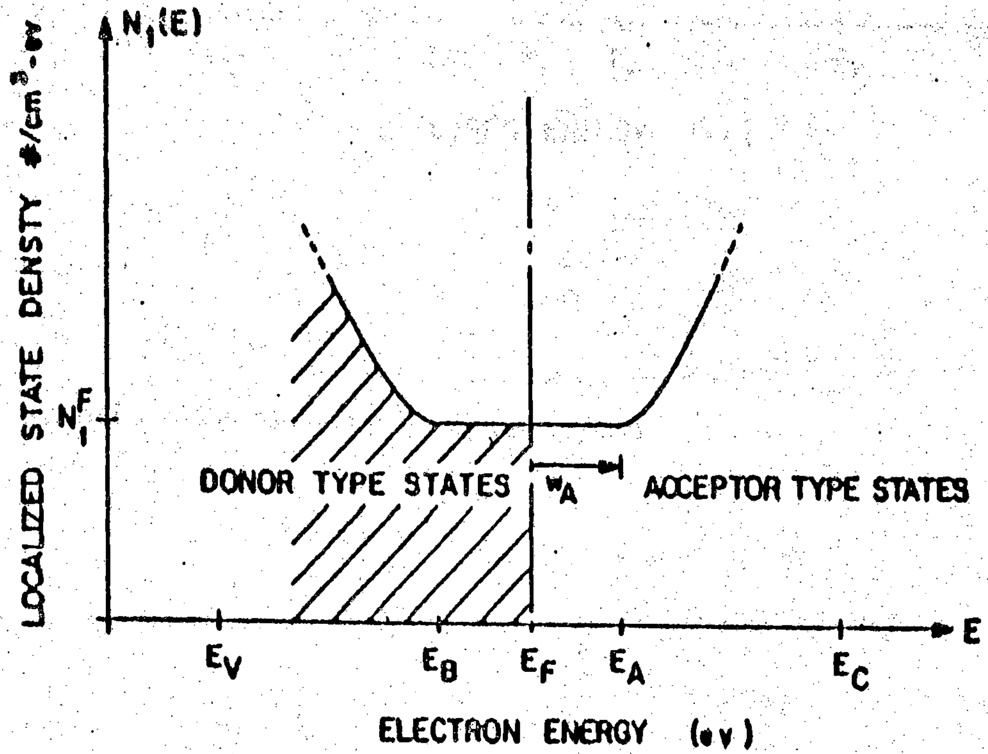

Figure 2.14 Simplified CFO model (from Reference 54)

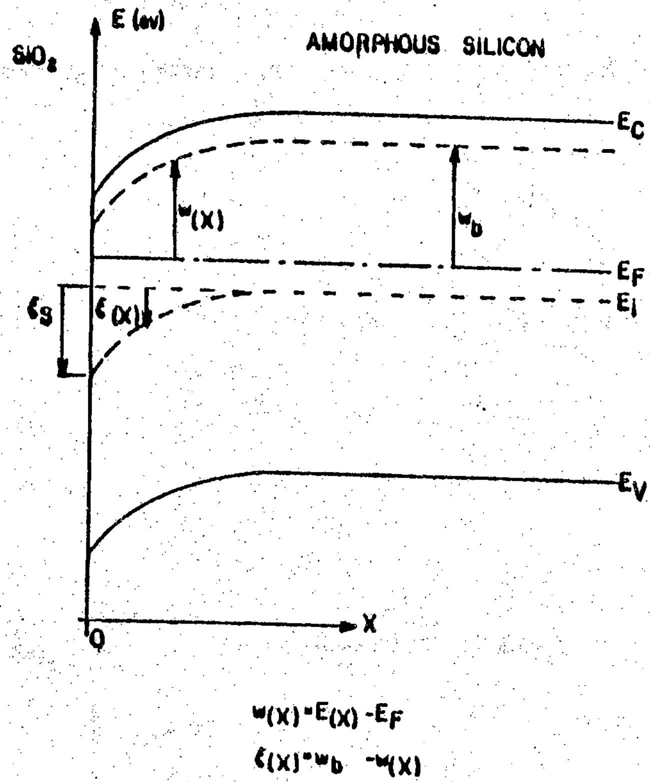

Figure 2.15 Band diagram for the surface of the amorphous material near the insulator with a positive gate voltage (from Reference 54)

insulator interface.

2) $w(x)$ is the energy with respect to the Fermi energy E_F.

3) The subscript "b" is added to a variable at a point where the bands are flat.

4) $\xi(x) = w_b - w(x)$, amount of band bending in the semiconductor. $\xi(x)$ is a positive number for positive gate voltages.

5) $N_t(w)$ is the number of localized states per unit volume per unit energy.

6) $n(x)$ and $p(x)$ are the number of electrons and holes per unit volume.

[A] Space Charge Region

For a band bending $\xi(x)$, the charge density $\rho(x)$ in the space charge region can be written as :

$$\rho(x) = -e \int_0^{\xi(x)} N_t(w)dw \qquad (2.5.1)$$

The mobile charge are included assuming that the extended states electrons and holes obey Maxwell-Boltzmann statistics.

$$\rho(x) = -e \int_0^{\xi(x)} N_t(w)dw + ep_b\exp[-\xi(x)/kT] - en_b\exp[\xi(x)/kT] \qquad (2.5.2)$$

where n_b and p_b are the bulk concentrations of electrons and holes in the extended states.

By inspection of Figure 2.14, the above equation can be written as :

$$\rho(x)=-e\{N_t^F\xi(x)+n_b\exp[\xi(x)/kT]-p_b\exp[-\xi(x)/kT]\} \qquad (2.5.3a)$$

for $\xi(x) \leq w_A$, i.e. $E \leq E_A$ at any point x.

For $E \geq E_A$ or $\xi \geq w_A$ the exponential increase in the density of states can be included and N_t is written as :

$$N_t(w)=N_t^F\exp\{m[w(x)-w_A]\}$$

where m controls the rate at which the states increase and N_t^F is the density of localized states at the Fermi energy. Therefore, for $\xi(x) > w_A$, by carrying out the integration :

$$\rho(x)=-e[N_t^F W_A+(N_t^F/m)(\exp\{m[\xi(x)-W_A]\}-1)$$

$$+n_b\exp[\xi(x)/kT]-p_b\exp[-\xi(x)/kT]] \qquad (2.5.3b)$$

[B] Relation between the Band Bending and the Gate Voltage

To determine the amount of band bending, $\xi(x)$, Poisson's equation needs to be solved for the electric field which in turn is related to the applied voltage.

By Poisson's equation :

$$\nabla^2\phi(x)=-\rho/\epsilon$$

where $\phi(x)$ is electrical potential.

Poisson's equation for electron energy inside the amorphous material in terms of energy variable $\xi(x)$ can be combined with equations (2.5.3a) and (2.5.3b) to form the following equations :

$$\frac{d^2\xi(x)}{dx^2}=\frac{e^2}{\epsilon}[N_t^F\xi(x)+n_b\exp(\frac{\xi(x)}{kT})-p_b\exp(\frac{-\xi(x)}{kT})] \tag{2.5.4a}$$

for $\xi \leq W_A$ and

$$\frac{d^2\xi(x)}{dx^2}=\frac{e^2}{\epsilon}\left[N_t^F W_A+\frac{N_t^F}{m}\{\exp[m(\xi(x)-W_A)]-1\}\right.$$

$$\left.+n_b\exp(\frac{\xi(x)}{kT})-p_b\exp(\frac{-\xi(x)}{kT})\right] \tag{2.5.4b}$$

for $\xi \geq W_A$.

The electric field Φ' is given by the following equation :

$$\Phi'=-\frac{d\phi}{dx}=\frac{-1}{e}\frac{d\xi(x)}{dx} \tag{2.5.5}$$

In order to solve for $\frac{d\xi(x)}{dx}$, both sides of equations 2.5.4(a), 2.5.4(b) can be multiplied with $\frac{2d\xi}{dx}$ and integrated from $-\infty$ to x or equivalently from 0 to $\xi(x)$ as follows :

$$\int_{-\infty}^{x}2\frac{d\xi}{dx}\frac{d^2\xi}{dx^2}dx=\int_{-\infty}^{x}\frac{d}{dx}(\frac{d\xi}{dx})^2dx=\int_{0}^{\xi(x)}d(\frac{d\xi}{dx})^2=(\frac{d\xi}{dx})^2$$

Then from equation (2.5.4a),

$$(\frac{d\xi}{dx})^2=2\frac{e^2}{\epsilon}\left\{\frac{1}{2}N_t^F\xi^2+n_bkT[\exp(\frac{\xi}{kT})-1]+p_bkT[\exp(-\frac{\xi}{kT})-1]\right\}$$

and

$$\frac{d\xi}{dx}=-F_1=-\left[2\frac{e^2}{\epsilon}\{N_t^F\frac{1}{2}\xi^2+n_bkT[\exp(\frac{\xi}{kT})-1]+p_bkT[\exp(-\frac{\xi}{kT})-1]\}\right]^{1/2} \tag{2.5.6a}$$

for $\xi \leq W_A$.

The negative sign is selected to make the field in the correct direction for positive gate voltages. Similarly, for the case of the exponential localized band tails, integrating from zero to W_A and then from W_A to $\xi(x)$, yields :

$$\frac{d\xi}{dx}=-F_2=-\Bigg\{2\frac{e^2}{\epsilon}\{N_t^F W_A(\xi-\frac{1}{2}W_A)-\frac{N_t^F}{m}(\xi-W_A)+\frac{N_t^F}{m^2}\{\exp[m(\xi-W_A)]-1\}$$

$$+n_b kT[\exp(\frac{\xi}{kT})-1]+p_b kT[\exp(-\frac{\xi}{kT})-1]\}\Bigg\}^{1/2} \qquad (2.5.6b)$$

for $\xi \geq W_A$. Again, F_2 is the positive root and is a positive number for a positive ξ.

From equation (2.5.5), the electric field at the surface is

$$\Phi'_s=\Phi'_{(x=0)}=\frac{-1}{e}\frac{d\xi}{dx}\bigg]_{x=0}=\frac{1}{e}F_n(\xi_s)$$

where $\xi_s = \xi(0)$, $n=1$ for $\xi \leq W_A$ and $n=2$ for $\xi \geq W_A$. The surface states between two amorphous materials (SiO_2 and a-Si) are unknown. For the large density of states case the surface states are probably insignificant. In the case where the localized states are much less, then surface states effect the result. For a simple and ideal case, assume there is no interface charge then

$$\epsilon_{ox}\Phi'_{ox}=\epsilon\Phi'_{(x=0)}$$

where Φ'_{ox} is the electric field in the oxide, ϵ and ϵ_{ox} are permittivities of semiconductor and oxide respectively. Therefore,

$$\Phi'_{ox}=\frac{\epsilon}{e\epsilon_{ox}}F_n(\xi_s)$$

Let d_{ox} be the oxide thickness and ΔV_{ox} be the voltage drop in the oxide, then

$$\Delta V_{ox} = \Phi'_{ox} d_{ox} = \frac{\epsilon d_{ox}}{e\epsilon_{ox}} F_n(\xi_s)$$

Since $V_G = \Delta V_{semi} + \Delta V_{ox}$ where V_G is the applied gate voltage and $\Delta V_{semi} = \frac{\xi_s}{e}$ is the voltage drop in the semiconductor, hence

$$V_G = \left[\frac{\xi_s}{e} + \frac{\epsilon d_{ox}}{e\epsilon_{ox}} F_n(\xi_s)\right] \qquad (2.5.7)$$

[C] Conductance Modulation

With zero gate bias, sheet conductance is given by

$$G_{so} = et(\mu_n n_b + \mu_p p_b)$$

where "t" is the amorphous silicon thickness. When a positive voltage is applied, the energy band near the surface is moved closer to the conduction band mobility edge thereby increasing the electrons in the extended states. The total conductance is

$$G_s = e(\mu_n \int_0^t n dx + \mu_p \int_0^t p dx)$$

and the change in sheet conductance $\Delta G_s = G_s - G_{so}$ is given by

$$\Delta G_s = e[\mu_n \int_0^t (n - n_b) dx + \mu_p \int_0^t (p - p_b) dx] \qquad (2.5.8)$$

The integrals can be written as

$$\Delta n=\int_{o}^{t}(n-n_b)dx=\int_{\xi_s}^{o}(n-n_b)\frac{dx}{d\xi}d\xi=\int_{o}^{\xi_s}\frac{n-n_b}{F_1(\xi)}d\xi \tag{2.5.9}$$

and

$$\Delta p=\int_{o}^{t}(p-p_b)dx=\int_{o}^{\xi_s}\frac{p-p_b}{F_1(\xi)}d\xi \tag{2.5.10}$$

The sheet conductance modulation would be

$$\Delta G_s=e\left[\mu_n n_b\int_{o}^{\xi_s}\frac{\exp(\xi/kT)-1}{F_1(\xi)}d\xi+\mu_p p_b\int_{o}^{\xi_s}\frac{\exp(-\xi/kT)-1}{F_1(\xi)}d\xi\right]$$

where ξ_s is related to the gate voltage by equation (7). For the case where $\xi \geq W_A$:

$$\Delta G_s=e\left[\mu_n n_b\left(\int_{o}^{W_A}\frac{\exp(\xi/kT)-1}{F_1(\xi)}d\xi+\int_{W_A}^{\xi_s}\frac{\exp(\xi/kT)-1}{F_2(\xi)}d\xi\right)\right.$$

$$\left.+\mu_p p_b\left(\int_{o}^{W_A}\frac{\exp(-\xi/kT)-1}{F_1(\xi)}d\xi+\int_{W_A}^{\xi_s}\frac{\exp(-\xi/kT)-1}{F_2(\xi)}d\xi\right)\right]$$

A similar expression for ΔG_s and $F(\xi)$ can be obtained for negative gate voltages by changing the signs of m, W_A and ξ_s.

The experimental results are the total current from the source to drain for various gate voltages with a fixed value of voltage from drain to source. The drain to source current I_{DS} can be written in terms of the sheet conductance as

$$I_{DS}=V_{DS}(G_{so}+\Delta G_s)\frac{\text{width}}{\text{length}}=V_{DS}\left(\frac{w}{l}\right)G_{so}\left(1+\frac{\Delta G_s}{G_{so}}\right)$$

or

$$I_{DS}=V_{DS}G_T(1+\frac{\Delta G_s}{G_{so}}) \tag{2.5.11}$$

where G_T is the total source to drain conductance. From equations (2,5,8), (2.5.9) and (2.5.10),

$$\frac{\Delta G_s}{G_{so}}=\frac{\mu_n \Delta n+\mu_p \Delta p}{t(\mu_n n_b+\mu_p p_b)}=\frac{\alpha \Delta n+\Delta p}{t(\alpha n_b+p_b)}$$

where the mobility ratio α is defined as μ_n/μ_p.

The density of localized states at the Fermi energy, N_t^F, is entangled in the expression of ΔG_s through the terms of Δn and Δp. As shown in equations (2.5.7) and (2.5.11), N_t^F is embedded in the expressions of both I_{DS} and V_G which are experimentally measurable variables. Information of N_t^F can be extracted from the analysis of I_{DS} vs. V_G data by the aid of a computer program.

2.6 Major Applications of Amorphous Silicon

Several important and major applications of a-Si are presented in this section. Some other new ideas for device applications of a-Si are still being actively explored in research. The presentations are intended to be brief and introductory only. Detailed information can be found in the references provided.

[A] Amorphous Silicon Solar Cells

The solar cell is a semiconductor device that converts sunlight directly into electrical power. When light is absorbed by a semiconductor junction, the photogenerated electrons and holes are collected by the contacting electrodes, resulting in a photocurrent. A solar cell under load is subject to a forward bias. If the illuminated device operates in the fourth quadrant of the device I-V characteristics, then the device can deliver electrical power to the external load. For a thin film semiconductor device to act as an efficient solar cell, several conditions must be satisfied. First, the optical absorption coefficient must be sufficiently large to absorb a significant fraction of the solar energy. Secondly, the photogenerated electrons and holes must be efficiently collected by contacting electrodes on both sides of the semiconductor film. Thirdly, a large built-in potential is also necessary for efficient photovoltaic energy conversion since this potential determines the output voltage of the cell. Finally, the total resistance in series with the solar cell must be kept small so that the IR drop during operation is only a small percentage of the output voltage.

The main advantage of an amorphous silicon solar cell is its promise of low cost fabrication of large area solar arrays. The low cost merits are due to both the low cost processing and the use of relatively low cost substrate material. Amorphous silicon films can be deposited on inexpensive substrates which are electrically active or passive such as glass, plastic, ceramic, metal, or graphite. The total material costs are on the order of a few dollars per square foot. On the other hand, the main disadvantages of a-Si solar cells are low efficiency and long term instability. Recently, a-Si solar cells of 10% conversion efficiency have been produced by RCA. The long term instability is due to the fact that light can induce changes in the electronic properties of a-Si:H film,

the Staebler-Wronski effect. Staebler and Wronski [103] observed that the photoconductivity and the dark conductivity of undoped a-Si:H decreased slowly during light illumination. The effect can be largely explained by assuming that optical illumination introduces states close to the center of the band gap.

A good and brief overall review on solar cells is given by Sze in the chapter 14 of his book "Physics of Semiconductor Devices", 2nd edition. A detailed review on the special topic "Amorphous Silicon Solar Cells" is written by Carlson and Wronski in the chapter 10 of the book "Amorphous Semiconductors", edited by M.H. Brodsky. Photovoltaic energy conversion of a-Si solar cells was observed in several types of devices such as p-n, p-i-n, and Schottky barrier junctions as well as heterojunctions. Figure 2.16 demonstrates various device structures that have been used to make thin film solar cells with hydrogenated amorphous silicon. The cells without an antireflection coating transmit only ~40-50% of the incident light into the a-Si:H. The average transmission can be increased to ~80-90% by means of antireflection coatings (~450Å) such as ZrO_2, TiO_2, Si_3N_4 and ITO (indium tin oxide).

The photovoltaic properties of a-Si:H solar cells are dependent on the a-Si film qualities which are again strongly influenced by the substrate temperature during glow discharge deposition. Efficient a-Si:H solar cells can only be made with substrate temperature in the range between 200 and 400°C because the films deposited in this temperature range tend to have minimum defect density of states. Beyond this temperature range, the devices exhibit very poor photovoltaic properties due to large defect states [22]. It must be emphasized that since the electronic and optical properties of glow discharge a-Si:H are strongly dependent on deposition conditions a wide variety of cell

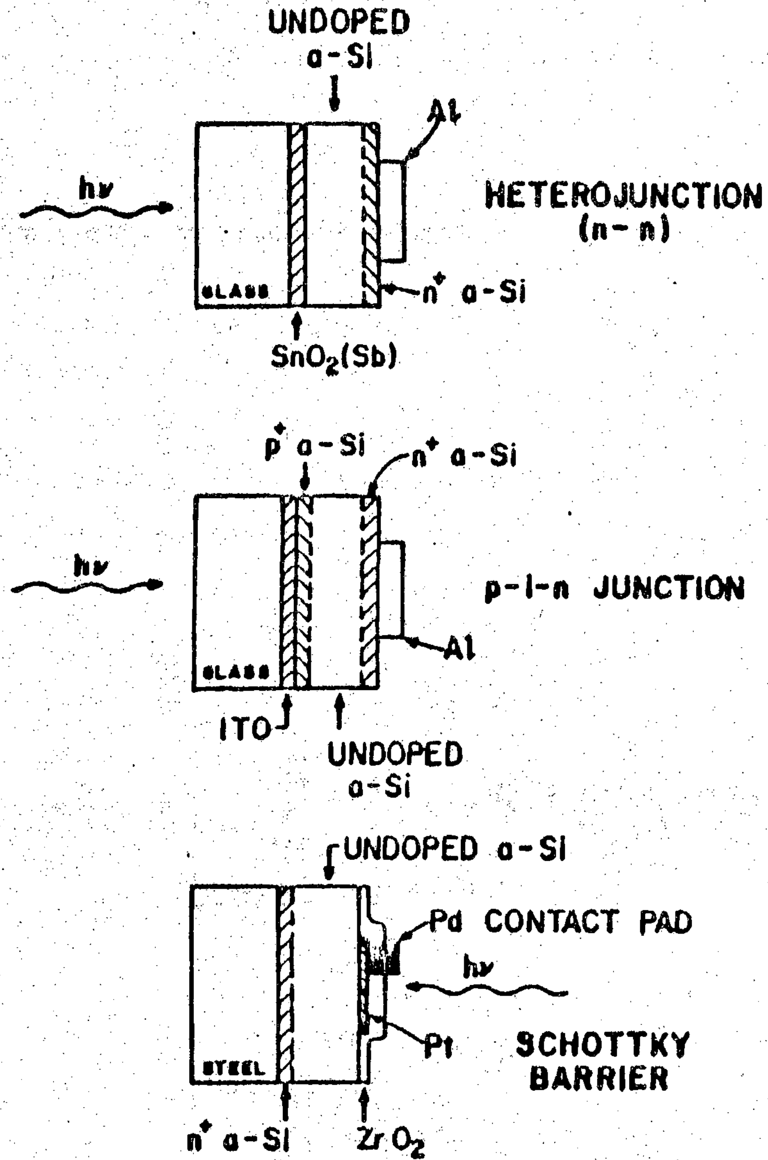

Figure 2.16 Schematic diagram of various solar cell structure (from Reference 31)

characteristics can be obtained. Up to the present, our knowledge concerning the defect states in a-Si:H is still not sufficient and our understanding of the relationship between the discharge kinetics and film properties is even less well developed. Therefore many of the properties of the a-Si, and the related a-Si solar cell devices, are not well understood. Much more research is needed in this field. Hopefully, in the near future, thin film a-Si:H solar cells may provide the people of the world with inexpensive, nonpolluting power from an inexhaustible source.

[B] Amorphous Silicon Thin Film Transistors

Besides solar cells, amorphous silicon thin film transistors (a-Si TFT) have also been intensively studied and explored recently. Some proposed applications of a-Si are simply modifications or just an extended usage of a-Si TFT's.

The first published work on an a-Si TFT was done by Neudeck and Malhotra [1]. Figure 2.17 demonstrated the geometric configuration (both experimental and calculated) for the device. For a-Si TFT, transistor operation depends entirely on the transport properties of the majority carriers, i.e. electrons in most cases. At zero gate voltage, low off current is achieved because the conductivity of a-Si is low. In the turned-on condition at $V_G > 0$, a strong majority carrier accumulation layer is induced in the a-Si channel. The drain characteristics I_D vs. V_D for a fixed value of V_G appear quite similar to an ordinary MOSFET. As the drain voltage (V_D) is increased, the drain current (I_D) increases but begins to saturate at large values of V_D, indicating a channel

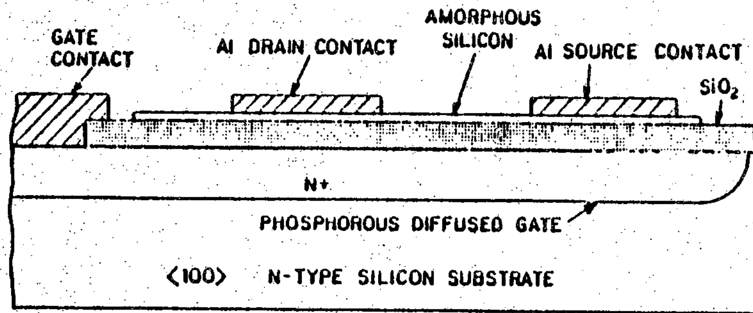

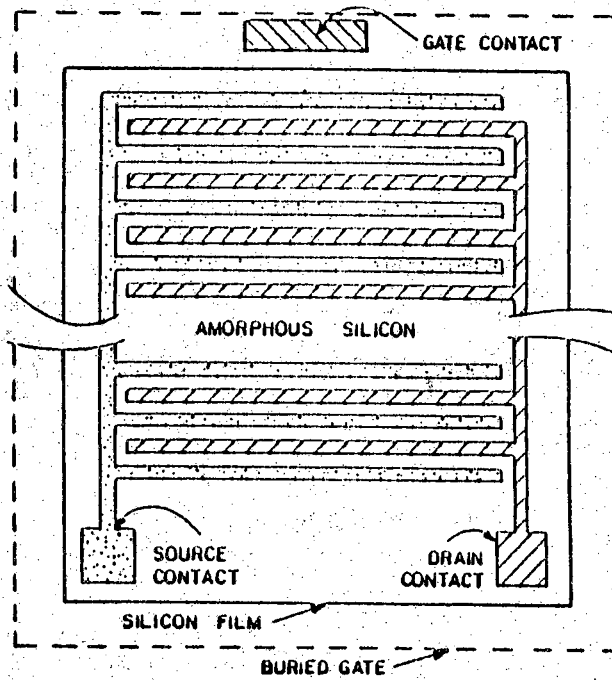

Figure 2.17 Cross section and top views of a completed a-Si TFT (from Reference 1)

pinch-off type condition.

The most promising and important application of a-Si TFT's is in the field of large panel, matrix-addressed Liquid Crystal Display (LCD) which is driven with a-Si TFT arrays [104-106]. Figure 2.18 illustrates the equivalent circuit of TFT-aided LCD picture element. The operation speed of a-Si TFT is intrinsically much slower than that of single crystal silicon MOSFET. Yet a-Si has the flexibility to be deposited on various inexpensive substrate materials in a large area. Therefore it is believed that a-Si TFT will be useful for some low cost slow speed switching arrays, such as a scanner for large area lensless facsimile transmitters and large area character displays as well as three dimensional integrated circuits.

A variety of experimental device structures such as inverted, noninverted, dual gate etc. were investigated. Figure 2.19 shows a schematic structure of an inverted gate device [107]. Figure 2.20 illustrates the schematic of a dual gate a-Si:H TFT [2]. In the dual gate structure, two conducting channels in the a-Si:H film, one at the top silicon-silicon nitride interface and one at the bottom interface, can be formed by applying positive biases to both gate electrodes. The device can also be operated in the single gate mode by grounding one gate electrode and applying a positive bias to the other gate electrode. Figure 2.21 shows the cross sectional view of an a-Si enhancement/depletion (E/D) inverter [108]. Figure 2.22 illustrates the equivalent circuit of the proposed inverter and Figure 2.24 demonstrates the transfer characteristics of the inverter. Amorphous silicon FET's can operate with both n- and p- channel by only changing the gate voltage polarity. The inverter shown has a p-channel depletion type load.

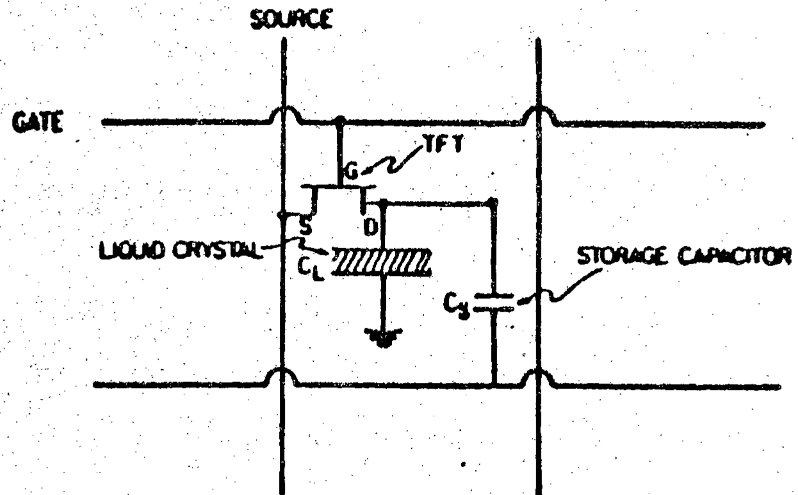

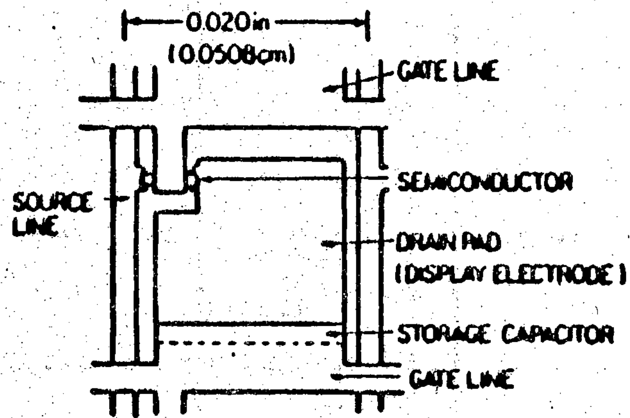

Figure 2.18 (a) Equivalent circuit of TFT-aided LCD picture element, (b) picture element layout for TFT-aided LCD (from Reference 104)

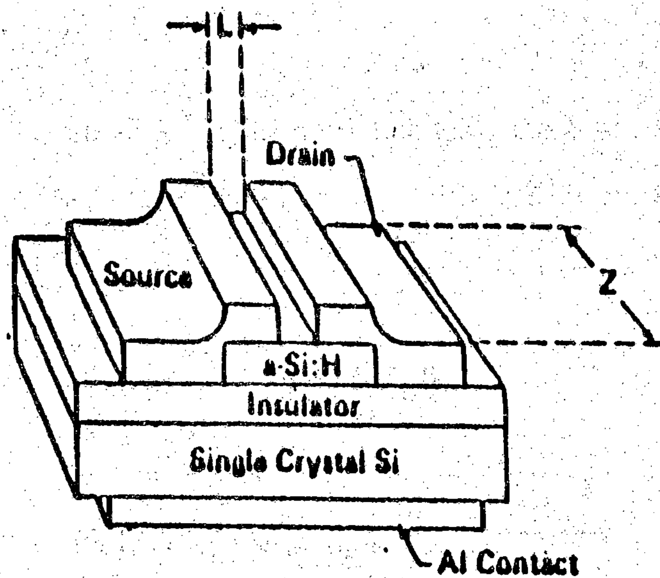

Figure 2.19 Thin film transistor in the inverted gate configuration. The channel length is L and the channel width is Z. (from Reference 107)

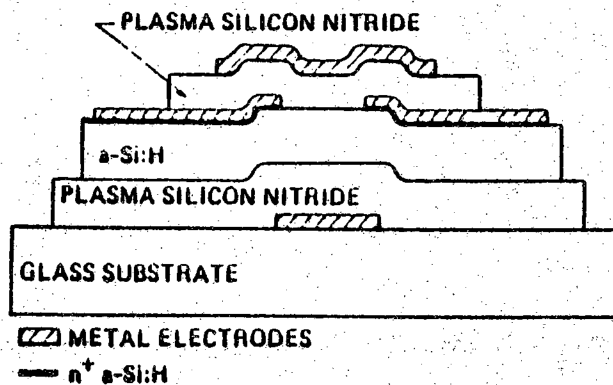

Figure 2.20 The schematic of a dual-gate a-Si:H TFT (from Reference 2)

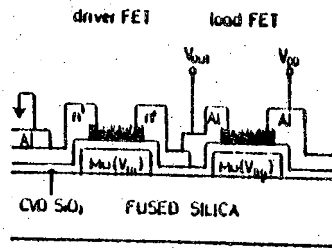

Figure 2.21 The cross-sectional view of a fabricated E/D inverter (from Reference 108)

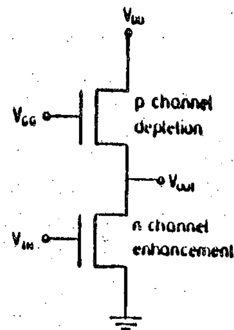

Figure 2.22 An equivalent circuit of the proposed E/D type inverter (from Reference 108)

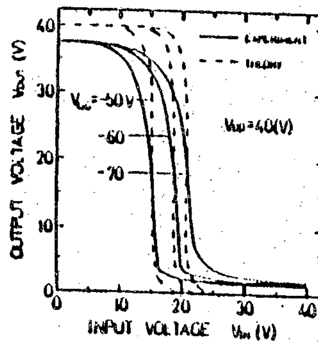

Figure 2.23 The transfer characteristics of the E/D type inverter (from Reference 108)

A short comment should be addressed to the nature of the contact between the metal (usually Al) and the a-Si. It has long been known that contacts produced by the evaporation of metals onto amorphous semiconductor surfaces tend to be ohmic in nature, i.e. they display little or no rectifying effect [109]. Sputtered and evaporated a-Si films, in particular, show no evidence of metal-semiconductor rectification. Glow discharge produced films, on the other hand, have been found to display strong rectification properties when coated with metals such as Al, Cr, Au, Pd and Pt [110]. That is why in some a-Si TFT's there is a n^+ doped layer of a-Si between the metal and the undoped glow discharged a-Si film; to make the contact be ohmic.

[C] Amorphous Silicon Image Sensors

Figure 2.24 shows a unit cell structure of an a-Si image sensor [6]. The cell consists of an a-Si FET, an a-Si photoconductor and an MOS capacitor. The equivalent circuit is shown in Figure 2.25. The device operates as follows : While the FET is off, the current which flows through the photoconductor is accumulated in the capacitor. When the FET is turned on, these accumulated charges are discharged. If the RC time constant of the capacitance of the MOS capacitor and the dark resistance of the photoconductor is much longer than a period of the clock pulse applied to the FET, the amplitude of the current packet passing through the FET is proportional to the intensity of illumination. Thus, by successive application of a clock pulse train to the cell array, a one-dimensional or two-dimensional image can be picked up.

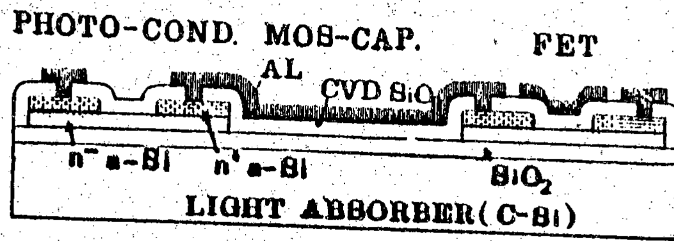

Figure 2.24 The unit cell structure of a proposed a-Si image sensor (from Reference 6)

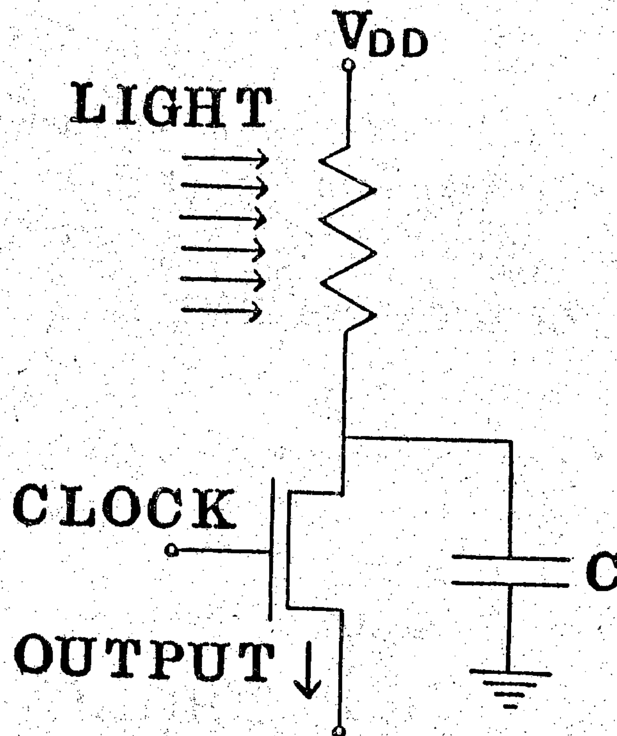

Figure 2.25 Equivalent circuit of the unit cell of the a-Si image sensor (from Reference 6)

The features of this unit cell can be summarized as follows : 1) The accumulation of the photocurrent can be realized by a small capacitance, because the dark resistivity of the a-Si is very high. 2) The electron mobility-lifetime product and the quantum efficiency of a-Si are about 10^{-4} cm^2/v and 1 respectively [111]. The gain of the a-Si photoconductor at applied voltage of 10 volts will be about 1000. This high gain can be utilized effectively. This is one of the merits of an a-Si image device. 3) It is possible to fabricate large area image sensors, because the a-Si can be deposited easily and uniformly on various substrate materials such as glass, metal and so on. The device will be useful for a cheap and large area sensor IC, for example in facsimile transmission.

[D] Amorphous Silicon Charge Coupled Devices

Figure 2.26 illustrates the cross sectional view of an a-Si charge coupled device (CCD's) with a four phase clock pulse [5]. The a-Si in the structure is sandwiched between staggered transfer electrodes with a silicon-oxynitride insulator. Electrons are transferred along the a-Si film with a serpentine motion. It is difficult to realize a-Si CCD's in a conventional structure because an electric field cannot penetrate sufficiently deep into a-Si for charge coupling. Therefore the sandwiched and overlapped structure is used for the ease of charge transfer. The prototype device fabricated on a glass substrate had a transfer inefficiency of as low as 0.4% transferring at 0.5-1 KHz clock frequencies. Amorphous CCD's will be potentially useful for large area linear or two dimensional image sensors.

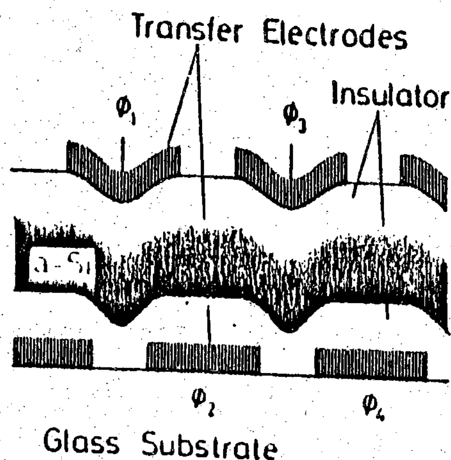

Figure 2.26 The cross-sectional view of a proposed a-Si CCD's with a four phase clock pulse (from Reference 5)

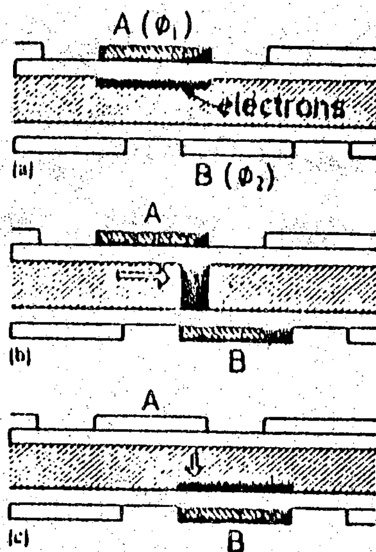

Figure 2.27 Schematic motion of electrons in the proposed a-Si CCD's (a) electrode A at a high level, (b) both electrodes A and B are at a high level, (c) B remains at a high level while A falls to a low level (from Reference 5)

Figure 2.27 shows a schematic motion of electrons in the a-Si. Initially only the transfer electrode A is connected with clock pulse Φ_1 which is at a high level voltage. Signal electrons (excess) are gathered at the a-Si/insulator interface just under electrode A. When the next transfer electrode, B, which is initially connected with the low level clock pulse Φ_2 rises to a high level Φ_1, these electrons move easily to the bulk a-Si region sandwiched between electrodes A and B, where overlapping of the depletion regions under two electrodes occurs. When Φ_1, at electrode A, falls to a low level then electrons move to and are stored at the opposite a-Si/insulator interface just above electrode B. Thus one transfer has been accomplished. During the charge transfer, electrons experience trapping and detrapping by localized states in a-Si. Analysis indicates that more than 95% of the initially stored electrons can be transferred within 250 μsec.

It should be noted that a great deal of research on the applications of a-Si in the photocopy techniques has being done by Xerox Company at their Palo Alto Research Center. These documents have been kept secret, unable to be accessed by the general public.

CHAPTER 3

EXPERIMENTAL PROCEDURES

Detailed experimental procedures are described in this chapter. The substrate and the film fabrication procedures are presented first, followed by measurement and test procedures. Hydrogenation by ion implantation is the last process to be described.

Figure 3.1 shows the device structure which was used in the early course of this research. In order to avoid surface contamination due to wet chemical etching of the gate contact window and to simplify the fabrication procedures, the device structure was changed to that illustrated in Figure 3.2. The substrate was changed to N/N^+ epitaxial type of silicon and the aluminum gate contact was located on the back (bottom) of the substrate. The following fabrication procedures are presented only for the device structure shown in Figure 3.2, known as the inverted gate structure.

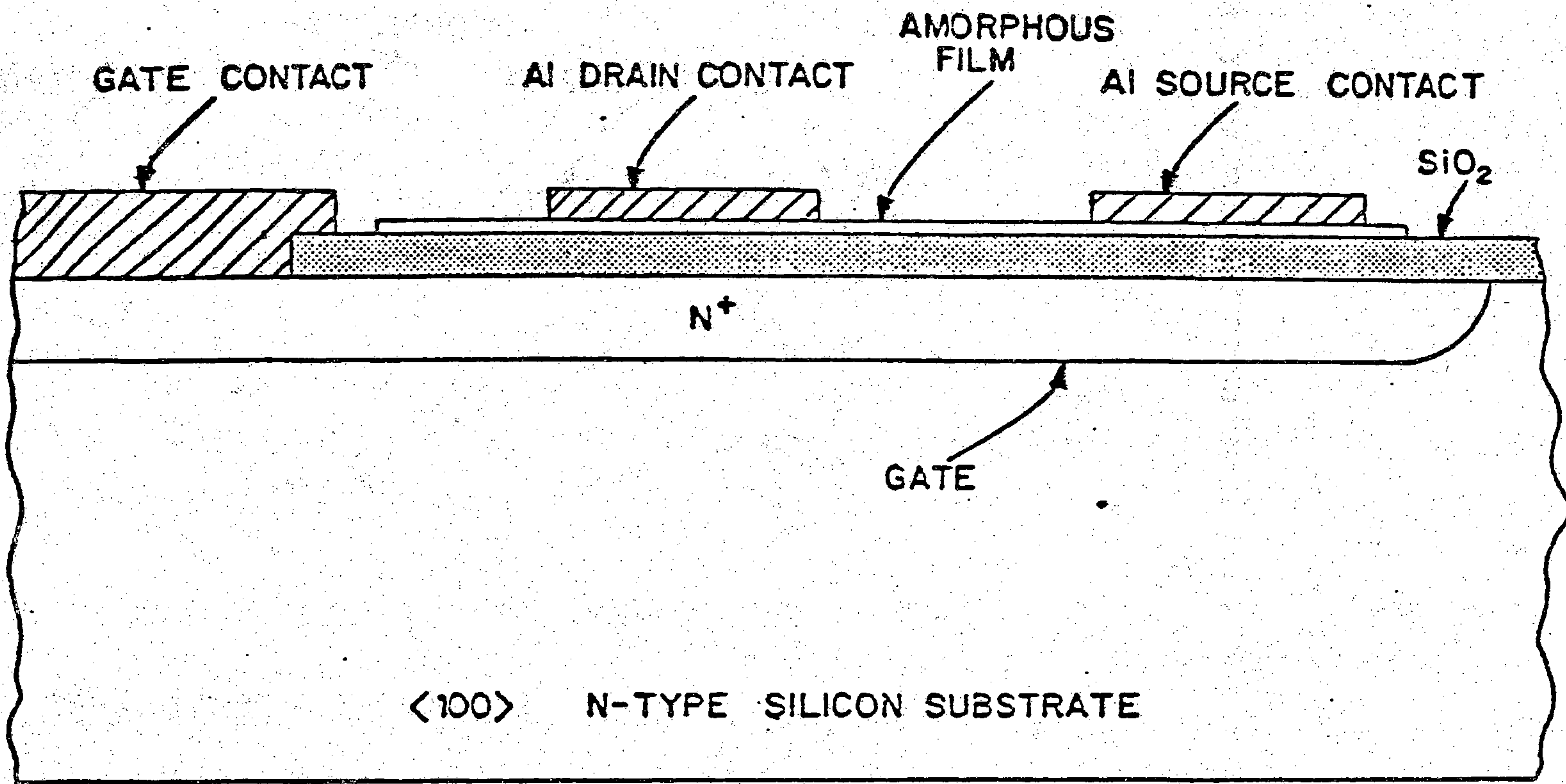

Figure 3.1 Cross section of a field effect structure with a buried N^+ layer as a gate

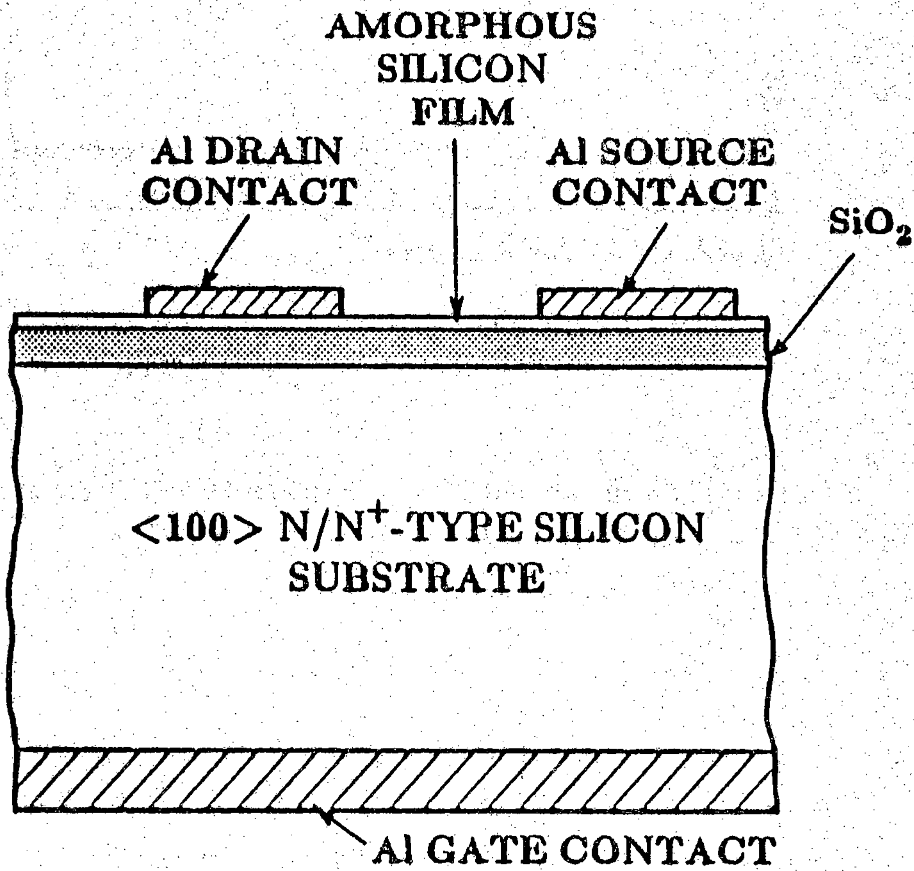

Figure 3.2 Cross section of an inverted gate field effect structure

3.1 Sample Preparation

[A] Substrate Fabrication

In order to study the properties of amorphous silicon films using the field effect measurement technique, we must minimize the effects of the non-ideal underlying MOS system. This requires a low leakage, pinhole-free, thin insulator with negligible ionic motion and high breakdown fields. The best characterized insulator to date is thermally grown silicon dioxide on single crystal silicon. If grown carefully, this kind of high quality silicon dioxide satisfies all the aforementioned requirements and thus was chosen as the insulator needed for the field effect measurements. In addition, the silicon substrate matches the a-Si thermally and resulted in a-Si films with less thermal strains and structural defects.

The substrate is a single crystal silicon wafer of 1.5 inches in diameter, supplied by the Monsanto Corporation. It is <100> oriented N/N^+ epitaxial type silicon. The epitaxial layer is about 8 to 10 microns thick, having resistivity of about 3.5 ohm-cm. The heavily doped N^+ silicon base is about 8 to 9 mils thick, having resistivity of about 0.013 ohm-cm. Silicon oriented in the <100> direction was used because the thermally grown silicon dioxide on the surface has a lower fixed charge and a lower density of surface states at the $Si\text{-}SiO_2$ interface [112] than the oxide grown on <111> oriented silicon.

The wafers were ultracleaned using electronic grade solvents, distilled deionized water, teflon beakers, and clean tweezers. The ultracleaning procedures are presented in the Appendix 1. Great care was taken in these cleaning procedures to assure a high quality oxide could be grown successfully

during the subsequent thermal oxidation. Each successive step in this cleaning process was performed in an individual, labeled teflon beaker. Tweezer handling was kept at a minimum. The oxidation furnace had been purged with HCl for 30 minutes prior to oxidation to minimize the sodium contamination [113,114], which leads to ionic motion in the oxide [115] during field effect measurements. Zero grade dry oxygen was passed through the furnace for at least half an hour before the wafer was loaded in the furnace. The wafer was loaded into the oxidation furnace within 20 minutes after it was ultracleaned to avoid any contamination during the intermediate time. The dry oxidation was performed at 1200°C for 125 minutes, resulting in a high quality oxide layer of about 3000 Å thickness which was checked by a chart of color. The wafer was pushed in and pulled out from the furnace slowly to avoid any thermal shock. Cleanliness of the oxidation furnace affected the oxide characteristics drastically. A contaminated furnace resulted in leaky oxides with low breakdown voltage and undesired fixed charge in the oxide. To make sure that a high quality oxide was obtained, tests for leakage current and sodium contamination were conducted on the oxide. The structure of the devices tested was a simple MOS structure. The leakage current through the oxide was measured at a voltage of 140 volts on either the drain or source contacts to be in the range of 10^{-11} amperes, negligible as compared to the a-Si film current at the same voltage. The voltage shift due to sodium contamination after a bias temperature stressing test (bias$=\pm 20$ volts, T$=$135°C), a commonly used technique on metal-oxide-semiconductor (MOS) devices, is only 0.8 volts. Figure 3.3 shows the capacitance-voltage (C-V) plot for the bias temperature stressing test. The typical measured density of fixed charge and surface states at the interface was in the range of 10^{10} to $10^{11}/cm^2$-eV .

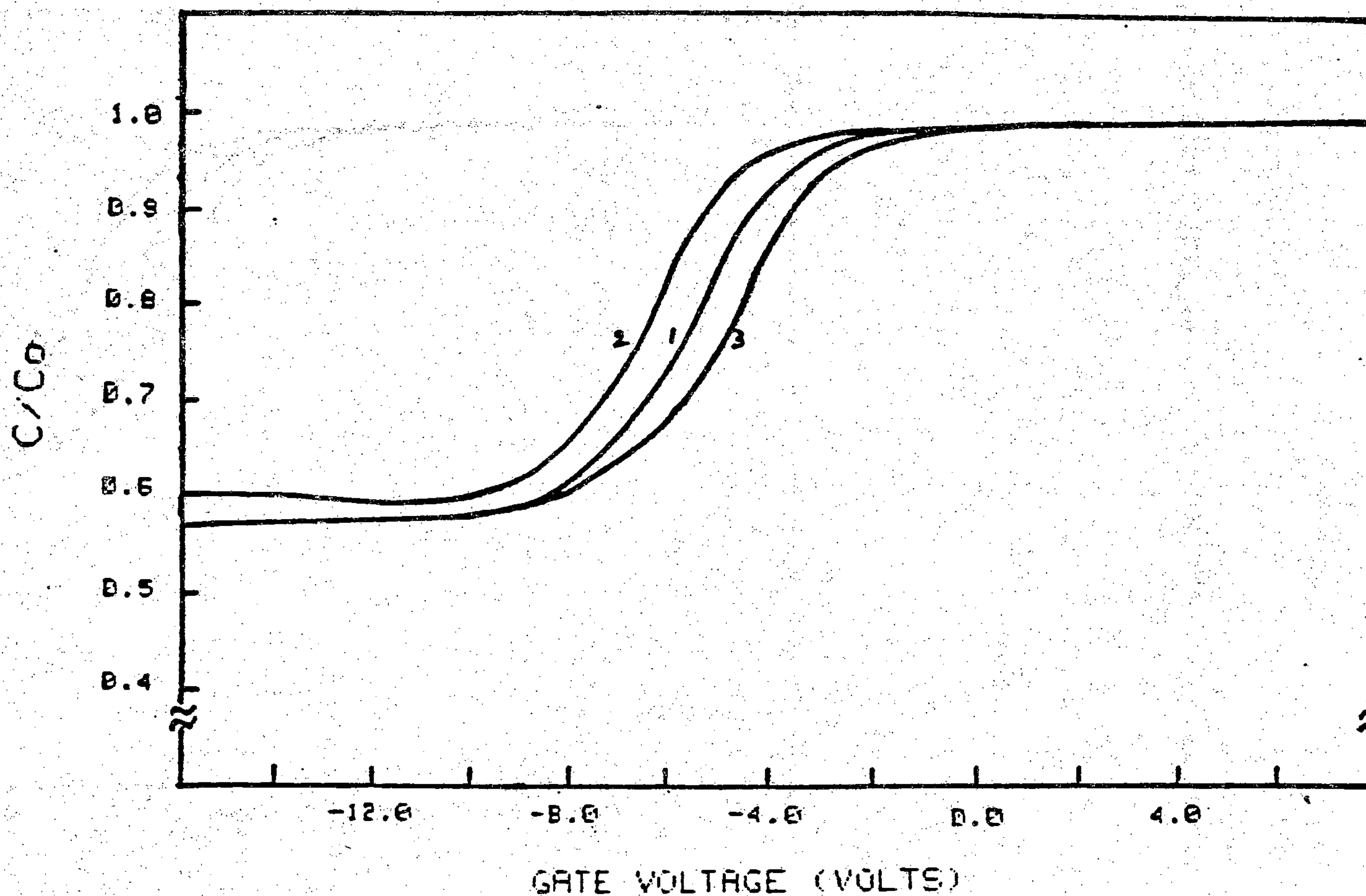

Figure 3.3 Capacitance-voltage plot for the bias temperature (BT) stressing test of a MOS capacitor, 33°-(3) : (1) initial curve, (2) after 5 min., @ +35 V, 150°C BT stressing, (3) after 5 min., @-35 V, 150°C BT stressing

[B] Amorphous Silicon Film Fabrication

I. Evaporation Facilities

Figure 3.4 is a schematic representation of the Varian VacIon system used for the a-Si thin film deposition. The system consists of a mechanical pump, three sorption pumps and an electronic ion pump. An ion pumped vacuum system can produce a very clean evaporation environment free of the oil contamination usually encountered in diffusion type pumping systems. The base pressure of the system was usually $6x10^{-9}$ torr.

The feedthrough ring shown in Figure 3.4 permits the attachment of such accessories as a thermocouple (TC) gauge, ultrahigh vacuum (UHV) and millitorr gauge tubes, plus water conducting lines for cooling the crystal detector, and crucible hearthes. Feedthroughs for electrical and motional purposes are also installed on the ring. Electrical feedthroughs include high voltage electrodes for the electron-gun and its control, substrate holder heater wires, and thermocouple wires for substrate temperature monitoring. Motional feedthroughs are for controlling and positioning of the shutter and the hearthes.

Amorphous films were prepared by electron beam evaporation of a 99.999995% pure polycrystalline silicon source contained in a vitreous carbon crucible which was situated in a water cooled copper hearth. The silicon chunks were cut from a polycrystalline silicon bar into small pieces and ultracleaned in teflon beakers and blown dry with ultrahigh purity nitrogen. The substrate was fastened with two copper clips to a stainless steel mounting block and placed above the source-chimney-shutter assembly. The distance between the

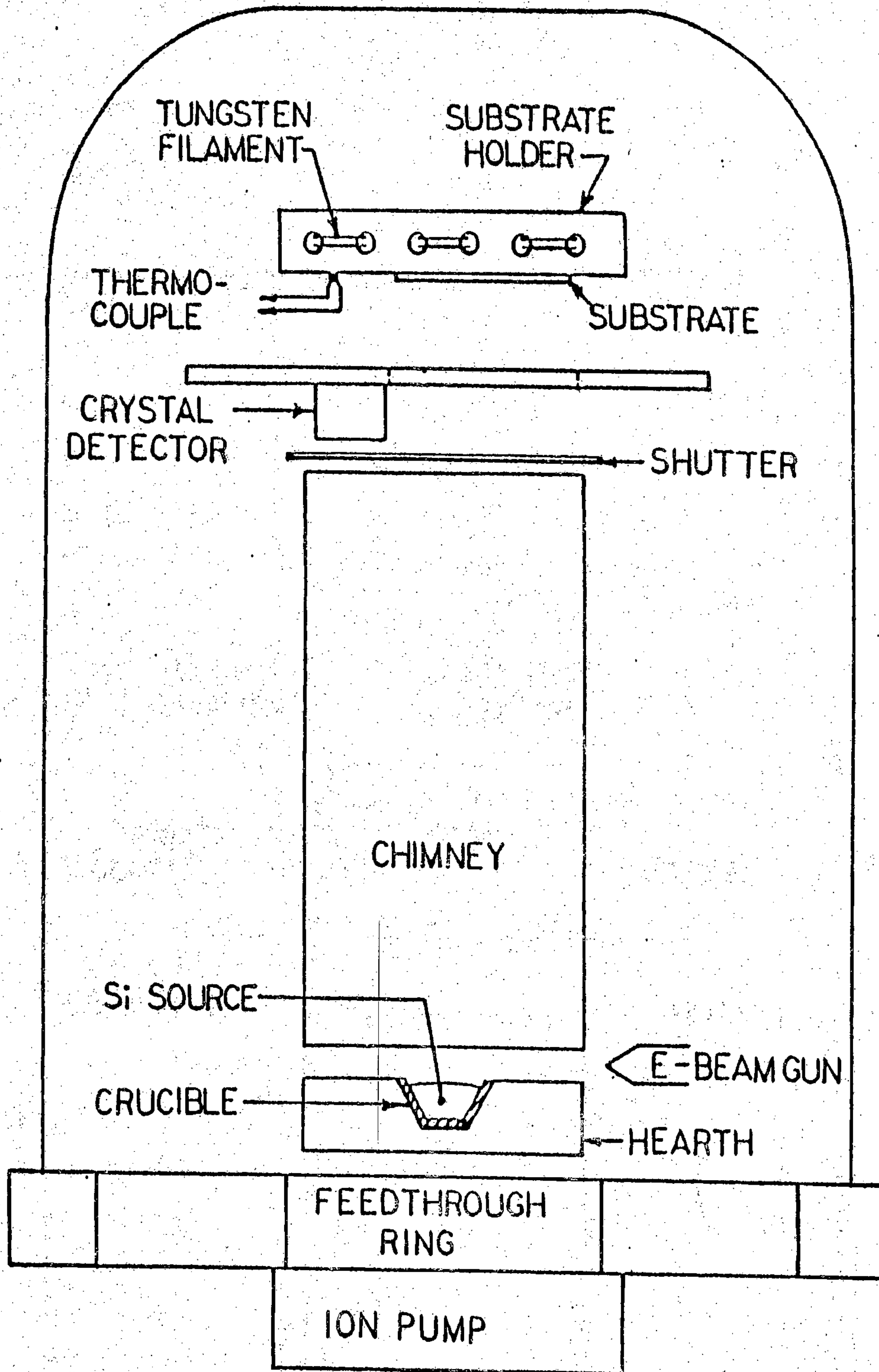

Figure 3.4 Schematic representation of vacuum evaporation apparatus

substrate holder and silicon source crucible was about 36 cm. The mounting block had provisions for heating of the substrate to 400°C and temperature measurements, consisting of a tungsten filament and a chromel-alumel thermocouple.

The deposition rate was monitored and controlled by using a Sloan Omni II deposition control master in which a local oscillator was tuned to the frequency of a quartz crystal monitor which was mounted in the vacuum system. The evaporant was deposited on the quartz crystal and the mass loading on the Au coated crystal caused a decrease in the resonant frequency of the crystal. The frequency difference between the crystal monitor and the tuned oscillator was converted into a d.c. voltage signal. Electronically differentiating this d.c. voltage provided an indication of the rate of frequency change and indirectly the rate of mass or thickness change taking place on the crystal.The Omni-II compared this indirect rate with a desired rate and generated a signal that was proportional to the difference between the two. This generated error signal was used to control a silicon controlled rectifier (SCR) power pack. The SCR chopped output waveform was applied to the filament of the electron gun through a step-down transformer which controlled the power delivered to the source to regulate evaporation and maintain the desired (constant) rate of deposition. The total frequency shift between the crystal and the oscillator frequencies, which was proportional to the evaporant thickness on the quartz crystal, was detected by the Omni II. The circular Au coated quartz crystal was mounted on a water cooled holder. The thicknesses of the films were measured on a Sloan Dektak thickness gauge to calibrate the Sloan Omni-II crystal deposition monitor. It was determined that a 1 KHz frequency shift on the monitor corresponded to a thickness of a-Si of typically

about 750 Å. It was very close to the calculated value by using the approximate formula given by the Sloan manual : $\Delta f \simeq DT/2$ where Δf is total frequency shift, D is material density in gm/cm^3 and T is film thickness in Angstroms.

The electron-gun (E-gun) is a Varian 6KW high rate source. Figure 3.5 illustrates the E-gun source parts. Note that in Figure 3.4, the E-gun position is sidewise to make a clearer drawing. Actually the filament of the E-gun source is located vertically in front of the crucible as demonstrated in Figure 3.5. This position arrangement prevents source contamination due to the tungsten filament of the E-gun. The beam is deflected by a permanent magnetic field from its point of origin into a sharp curvature of 210° to intercept the crucible. The electron beam is moved around within the crucible by a variable electromagnetic field. The variable electromagnetic field is controlled by two knobs labeled "A" and "B" which are installed on a remote control module. Electrons are accelerated toward the grounded crucible assembly by a large negative voltage at the filament. The beam current provided by this E-gun source is in the range of 0 — 1000 mA with beam voltage of 6000 volts. Therefore the E-gun source can provide an electron beam with a maximum power of 6KW. The crucible, which is 2.5 cm in diameter, is made of vitreous carbon.

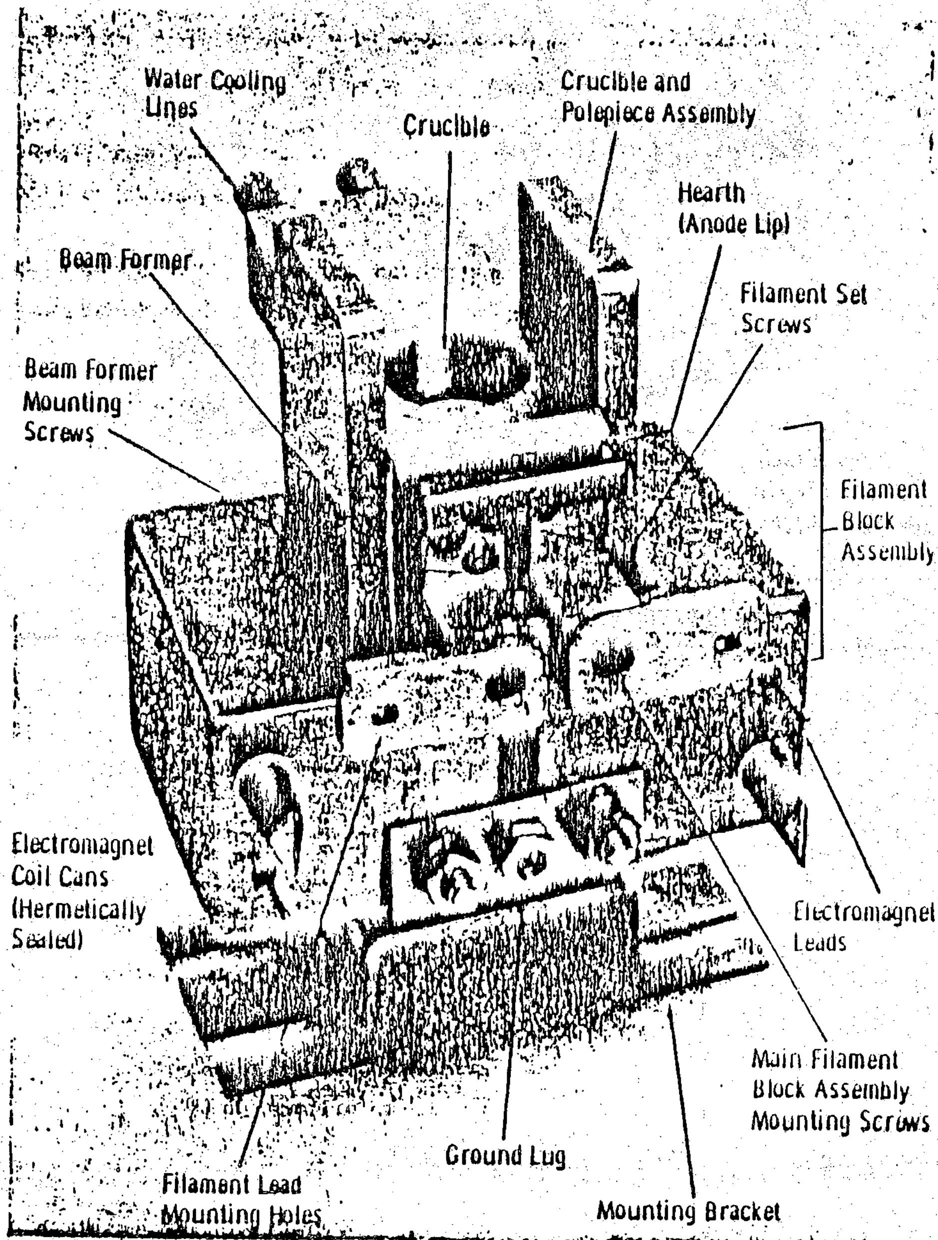

Figure 3.5 Identification of parts of the E-gun source

II. Film Evaporation Procedures

The wafer was loaded into the vacuum system immediately after removal from the oxidation furnace. After closing the vacuum system, an eighteen or twenty four hour 140°C bake-out of the work chamber and pump was performed. This bake-out procedure reduced the residual gas in the chamber to a minimum and removed many of the contaminants. The system was then allowed to cool and pump down for several hours to a pressure less than 6×10^{-9} torr. After that period, the substrate was heated to 400°C for one and one half hours to thermally clean the surface of the substrate. The thermal cleaning reduced the hysteresis [51] in the field effect curves (I_{DS} vs. V_G) to an insignificant value. This procedure also decreased the time dependence of the source drain current each time the gate voltage is stepped to a new value. The substrate was allowed to cool to 200°C before silicon was electron beam deposited. The deposition was performed within one hour after thermal cleaning. Pressures prior to evaporation were typically below 1×10^{-7} torr (usually 7×10^{-8} torr). The water cooling system to the crystal and the Sloan deposition controller were turned on and allowed to warm up before deposition was initiated. The shutter was closed during the initial part of the deposition sequence thus shielding the substrate from the silicon evaporation source. The electron-gun was turned on. After focusing and positioning the beam spot in the vitreous carbon crucible, the silicon source was melted and thermally soaked below its evaporation temperature for 10 to 15 minutes to allow for outgassing of the source. The electron beam emission current was adjusted to provide additional power to the source until evaporation began and the Omni-II controlled the deposition rate. After the deposition rate was stabilized at the desired level, the shutter was opened. The vacuum system pressure during

deposition stabilized at a typical value of 3 to $5x10^{-7}$ torr. In this research, the deposition rate was fixed at about 3 Å/sec. Films with high deposition rates tend to have a less homogeneous structure and contain more defects and voids than the films deposited at low rates. The density of localized states increases with the deposition rate [51]. Typical evaporations required 3 to 5 minutes. Amorphous silicon film of thickness 700 to 750 Å were deposited over the entire wafer. These values were used due to the fact that 90% of the current flows through an a-Si conducting channel which is a layer less than 100 Å thick [101] adjacent to the SiO_2-amorphous silicon interface. The device is modeled as a modulated resistor which is in parallel with a bulk resistor. The a-Si film is kept thin to maximize the conductance modulation of the field effect measurement. On the other hand, the film should be thick enough to prevent penetration of the electric field through the a-Si for the case of a very low density of localized states film.

Immediately following deposition, some films were given a four- hour 300°C or 400°C *in situ* thermal anneal and some films were not subjected to such an anneal. The final field effect results, after hydrogenation, were quite different for these two cases. Further discussions on these differences will be presented in the following chapter. The *in situ* thermal anneal was conducted by turning on the substrate heater element, which was a coiled tungsten wire of 10 mil in diameter. It required about 45 minutes for the substrate holder to reach 400°C.

[C] Drain and Source Contacts

The sample was allowed to cool to room temperature, then removed from the vacuum system and loaded immediately into another vacuum system for aluminum (Al) deposition of the source and drain contacts. The source was Al staples of five nines purity. The staples were cleaned ultrasonically with hot Trichloroetheylene (TCE), Acetone, rinsed with deionized water, and blown dry with ultra pure nitrogen. These staples were evaporated from a degreased low alkali tungsten filament which had gone through the same cleaning procedures as used to clean the Al staples. The NRC vacuum system pressure prior to Al deposition was usually 3 to 5×10^{-7} torr. An aluminum layer of about 1000 Å thick was deposited with a filament current of 25 mA for one minute.

After Al deposition, the wafer was removed from the vacuum system and subjected to a process for stripping the backside silicon dioxide. Black wax was applied on a piece of Kodak slide cover glass which was heated on a hot plate. The Al coated side of the wafer was placed face down on the glass. After being removed from the hot plate and allowed to cool, the back oxide was etched with a buffered HF solution. The wafer was then removed from the glass plate and subjected to cleaning treatments with solvents. Trichloroetheylene was used first to dissolve the black wax which was left on the wafer. The wafer was then rinsed with Acetone and finally rinsed with deionized water and blown dry with ultra pure nitrogen.

The source-drain contacts to the a-Si films were produced by standard photolithographic techniques. The contact photomask was made on a Gyrex model 105 pattern generator. A positive photoresist, Shipley Az-1450 J, was used throughout the research. The photoresist was spun on the wafer at a speed of 4.75 Krpm for 30 seconds, resulting in a typical resist thickness of

about one micron. The resist was then dried, prior to exposure, by pre-baking in an oven at 90°C for 15 minutes. The resist coated wafer was then aligned with the photomask on a Kasper model 17A wafer aligner. After a 14 second exposure with ultraviolet light (with light setting of 5.8 MW/cm^2), the photoresist pattern was produced by developing in Az developer, diluted 3:1 with D.I. water, for approximately 35 seconds. Following a D.I. rinse for 2 minutes, the resist pattern was hardened by a 20 minute post-bake at 90°C. Using a standard aluminum etch, which contained 760 c.c. H_3PO_4, 150 c.c. CH_3COOH, 30 c.c. HNO_3, and 50 c.c. H_2O, the excess aluminum was removed, leaving behind the desired source and drain contact pattern. After a D.I. water rinse, the unexposed photoresist was then stripped with Acetone at room temperature. The wafer was again rinsed with D.I. water and blown dry with ultra high pure nitrogen. The wafer was finally loaded into the same NRC vacuum system for aluminum back gate contact deposition which resulted in a layer of aluminum of about 1500 Å thick. A cross section view of the completed device structure is illustrated in Figure 3.2. Since the resistivity of the N^+ substrate base is 0.013 ohm-cm, which corresponds to a heavily doping density of about $5x10^{18}/cm^3$, a good ohmic contact is formed on the back aluminum gate. Therefore no contact sintering is performed. In addition, contact sintering is usually performed at a high temperature of 550°C which is not a compatible process for the a-Si.

The Gyrex produced pattern of drain source contacts was of an interdigital finger geometry. This geometry was used because of the high resistivity ($\sim 10^7$ ohm-cm) of the a-Si material. The geometry reduced the resistance between the source and drain by about three orders of magnitude for ease of current measurements since only a small voltage will be applied across

the contacts. The pattern "printed" on the wafer was an image of the pattern on the photomask which consisted of 50 interdigital finger pairs. These fingers were designed to be one mil wide and 97.5 mil in length, with 1.75 mil of spacing between fingers. The actually measured dimensions of the pattern on the wafer were 0.98 mil, 95.3 mil and 1.68 mil respectively. Considering the drain source current across the space between a pair of fingers, the ratio of channel width to channel length (i.e. finger length/finger spacing) is 56.7 (i.e. $\frac{95.3}{1.68}$) which is calculated by using the above measured values. With a total of 50 interdigital finger pairs, the overall ratio of channel width to channel length is 2836. Figure 3.6 is a Calcomp plot illustrating the pattern used. Overlap regions in portions of the pattern were used to ensure electrical continuity due to potential errors in the pattern generator tolerance. There were eight identical patterns on each wafer.

3.2 Some Experiment Measurements

STRUCTURE: X-ray analysis is used to determine the sample structure. A General Electric XRD-5 x-ray unit was used in the diffraction mode. $K\alpha$ radiation from a copper target was used. The output was obtained in the form of a strip chart recording where diffracted x-ray intensity, in relative units, is plotted as a function of 2θ, where θ is the angle of insidence.

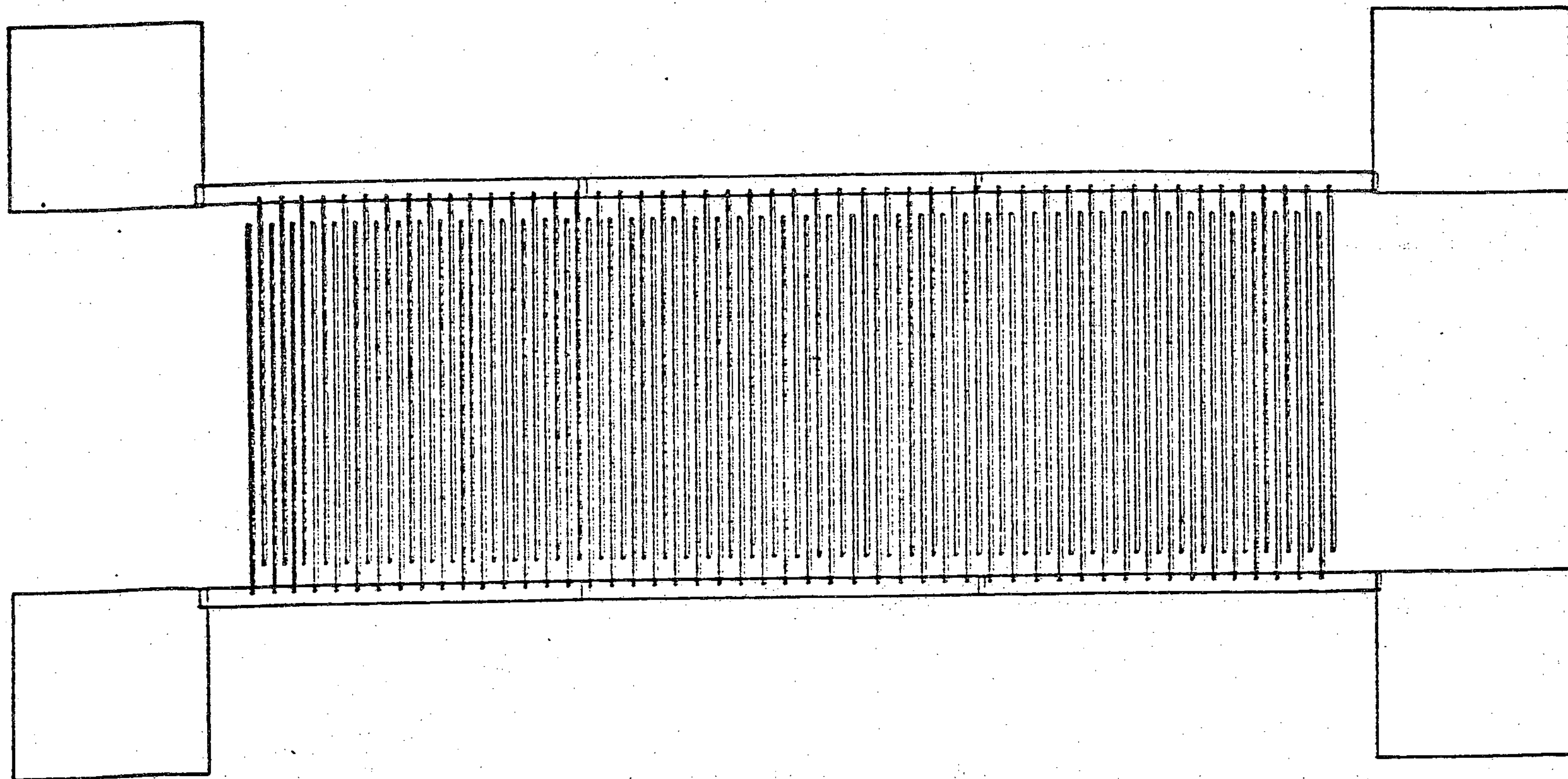

Figure 3.6 An interdigital finger pattern for field effect measurements

THICKNESS: Sample thickness of all a-Si film was measured using a Sloan Dektak. Estimated accuracy for absolute thickness measurements using this technique is ± 10%. The silicon dioxide thickness was determined from the time and the temperature of the oxidation using standard charts between the thickness of the oxide and the time for various temperatures.

A more precision method to measure the Sio_2 thickness is an ellipsometer[116]. Ellipsometers are precition optical instruments which measure changes in the state of polarized light reflected from the surfaces of the sample. Such measurements permit determination of the optocal constants of sample surfaces, and the thickness and refractive index of thin films on those surfaces. The measurements involve rotation of a polarizer and an analyzer to cause extinction of a beam of polarized light reflected from the surface of the sample. The photoelectric ellipsometer system type 43603-200E was used in this research. A Fortran 77 program, that performs the calculations required to analyze ellipsometer, measurements was used to analyze the data. The program was written for use on DEC 11/70's and 11/780 VAX's with UNIX operating systems. The film thickness and index of refraction was determined.

RESIDUAL GAS ANALYSIS: The residual gas analyzer used was a Granville Phillips model Seprascan 400. For detection purposes a Kiethley 602 electrometer was used and a strip chart was connected to the output to record the detector's output.

3.3 Field Effect Measurements

The field effect measurements in this research were carried out by applying a small fixed drain-source voltage (typically 1.5 volts) and measuring the current as the gate voltage was changed over positive and negative values.

A light shielded aluminum box with a hinged top cover plate served as the measurement compartment. Shielded cable input/output terminals were made using BNC connectors. Inside the compartment an aluminum block, which served as the substrate holder, was insulated from the box by an alumina plate and a thick teflon slab. To avoid any surface leakage due to moisture or other conduction paths, a curled copper tube was installed to provide for dry ultra high purity nitrogen to flow over the sample during the measurements.

Three probes were used inside the compartment to make electrical connections to the device under test. Each probe consisted of a polyethlene block with a teflon rod attached so as to extend 0.5 inch to 1 inch above the substrate holder. At the end of each rod 10 mil thick tungsten probes were attached. Coaxial cables were used to connect the probe tips to the input/output terminals.

A Keithley model 610C electrometer was used for making measurements on the thin film samples. The instrument has an input impedance in excess of 10^{14} ohm and has the capability of measuring current to 10^{-15} amperes full scale. Throughout the current measurements the range multiplier switch on the electrometer was set to give a maximum drop of 0.1 volts across the meter. The electrometer was also used to check the isolation of the probes in the measurement compartment. The resistance measured between two probes spaced $\frac{1}{8}$ inch apart on a teflon strip was greater than the highest meter range.

The resistance between the ground and each probe was also greater than the highest meter range.

The circuit for the field effect measurement is shown in Figure 3.7. Connections to the batteries and electrometer were made with RG-62/U coaxial cable through BNC connectors. The Keithley 610C electrometer was used for the source drain current measurement and a digital voltmeter was used to measure the gate voltage.

When making the measurements, the ultrahigh purity dry nitrogen source was first turned on and then contacts with the device terminals were made. The gate voltage was set by adjusting a potentiometer across a battery supply. For each setting of gate voltage, the source-drain current (I_{SD}) was recorded after 5 minutes had elapsed to insure that near steady state conditions had been achieved. In order to make sure that the measured change in source drain current was due to the field effect and not leakage current through the silicon dioxide insulator, checks were made by measuring the leakage current between gate and source, gate and drain, and the source-drain current on reversing the polarity of the 1.5 volts battery. For good devices very small change in source-drain current was observed and the leakage was negligible as compared to the source-drain current. The data to be analyzed were obtained by taking the average value of I_{DS} and I_{SD} for each setting of gate voltage. The potentiometer was then reset to a new gate voltage. The electrometer was locked to protect it from damage when the gate voltage was changed. The gate voltage was usually changed in steps of 5 volts and was increased up to 140 volts. Once the measurements for positive gate voltage were completed, the polarity of the batteries were reversed and the sequence was repeated for negative gate voltages. Typically, source drain currents ranging from 10^{-11} to 10^{-5} amperes

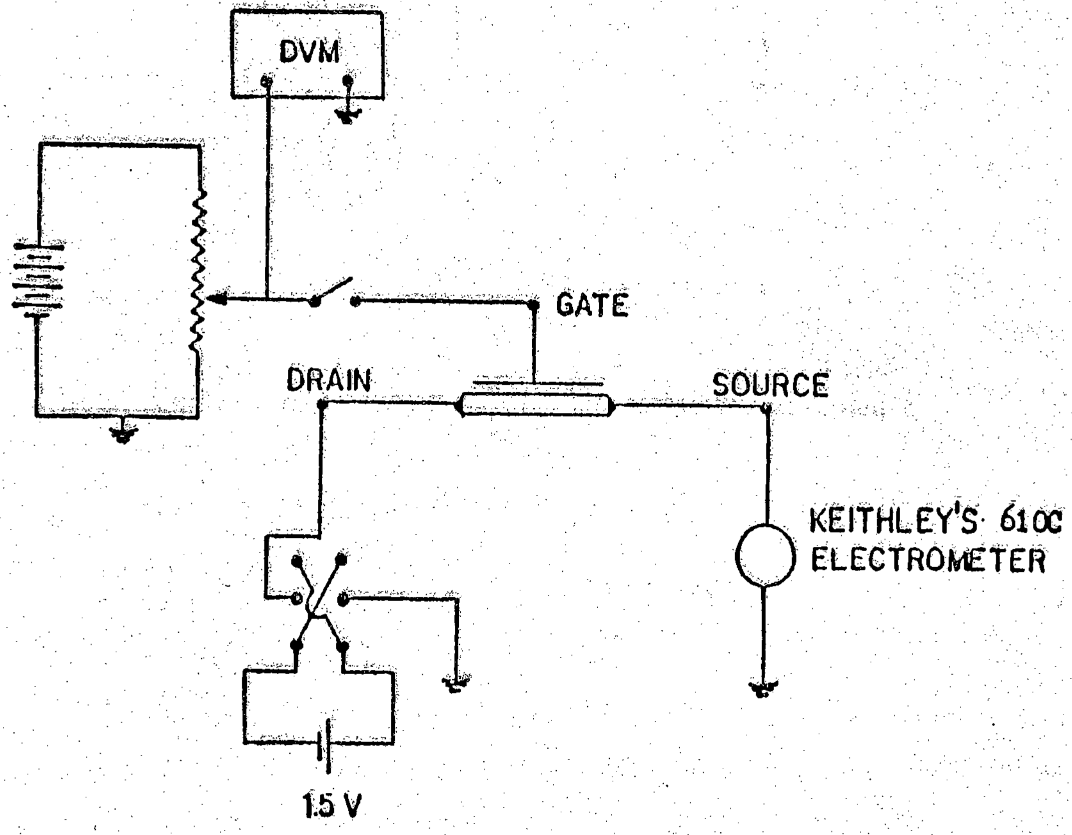

Figure 3.7 Circuit used for field effect measurements

were measured for applied gate voltages ranging from 0 to 140 volts. The above measurements were made at room temperature, 23°C.

3.4 Hydrogen Ion Implantation and Thermal Activation

Hydrogenation of the a-Si in this research was conducted by ion implantation of hydrogen into the evaporated a-Si films. After the initial field effect data were taken, the sample was loaded into an AI model 210 ion implanter. Ion implantations were performed when the system pressure was pumped down to a typical value of 8×10^{-7} torr. Since the a-Si film was only about 750 Å thick, a light element such as hydrogen, implanted with moderate energy, can easily penetrate the a-Si film. Therefore a technique, developed by other researchers [117], was used in this research to reduce the hydrogen energy for implantation. The hydrogen ions were produced by ballistic impact of hydrogen molecules source with electrons which were emitted from a hot filament. The hydrogen ions entered into a magnetic mass analyzer. By adjusting the magnetic field, the analyzer could be made to select only the desired ion species with mass to charge ratio of 2, namely H_2^+ ions. These H_2^+ ions were then accelerated by an electrical potential of 25 Kev, which is the minimum acceleration energy available at Purdue, to obtain 12.5 Kev H_1^+ implanted ions. The channeling effect, to which attention has to be paid in the ion implantation into crystalline material, was not considered to be important here because of the amorphous material. Hence, the incident direction of the

implanted ions was normal to the sample surface. In addition to the low acceleration voltage, the ion beam current was also maintained at a low value, less than 10 $\mu A/cm^2$, to avoid ion beam heating of the film. Different implantation doses ranging from $1x10^{16}/cm^2$ to $1.5x10^{17}/cm^2$ were applied in this research. Typically, it took about 5 hours to finish the implantation with a dosage of $5x10^{16}/cm^2$. The implant dosage was measured by a current integrator installed in the ion implanter. The concentration profile for single energy hydrogen implanted into amorphous silicon is essentially that of a Gaussian distribution [117] with a projected range of around 1600 Å [118]. Therefore much of the implanted hydrogen went through a-Si film into the silicon dioxide insulator. In order to increase the implanted hydrogen in the a-Si film, to optimize the hydrogenation technique, a thin film overcoating photoresist of the wafer is suggested (further discussed in Chapter 6, section 6.2).

On some samples, after hydrogen implantation, the field effect measurement was performed before and then after the samples were thermally annealed in a Marshall oven at 230°C for 2 hours in a nitrogen ambient. This time and temperature was chosen based upon a series of experiments in which the annealing temperature or the annealing time was changed while the other parameter was fixed. More discussions on these experiments are given in Chapter 4, section 4.5. After thermal annealing the slightly milky surface, which was observed on the films after implantation, disappeared. The thermal anneal activates (forms H-Si bonds) the implanted hydrogen, and hence this post-implant annealing is referred to as thermal activation to distinguish it from the *in situ* thermal annealing on the deposited films. The field effect measurement was again carried out after thermal activation.

CHAPTER 4

EXPERIMENTAL RESULTS AND ANALYSIS OF THE DATA

Experimental results along with their corresponding discussions are presented in this chapter. The results are presented in a way which is intended to elucidate the following points : (1) the specific fabrication steps for the device, (2) the field effect data observed due to this treatment, and (3) interpreting the data and to discuss the results. The data presented from section 4.2 up to section 4.5 are the data obtained from the hydrogenated devices without *in situ* thermal annealing. These reports include a comparison of hydrogenated and nonhydrogenated results, field effect conductance change after hydrogenation, influence of implantation dosage on the field effect curves, and hydrogen effusion phenomenon. A comparison of hydrogenated results with and without *in situ* thermal annealing is included in section 4.6.

The field effect measurement of the conductance change was employed in this research as a probing tool to investigate the changes in the localized states of a-Si upon hydrogenation. This measurement has become a standard experimental technique for determining the density of localized states in

amorphous silicon. Unlike other techniques, which can only estimate the density of states at the Fermi level or the total number of unpaired electron spins, the field effect technique provides the most detailed information about the density of states within the span of the mobility gap [12,13,42,43,92,110]. The field effect technique is also very useful for studying the changes in a single sample as it undergoes a series of treatments.

Nearly eighty wafers have been fabricated and measured. Two wafers were processed concurrently during each fabrication sequence. There were eight devices on each wafer. A numbering scheme was devised for easy identification of the devices fabricated. A single device on the last fabricated wafer, 42*-(2)-[3], is taken as an example to demonstrate this numbering scheme. The first two digits, namely "42", serve as an identifier which is simply the sequential number of the completed fabrication process. The mark "*" means the device structure is that of a back gate contact type. The following number in round parentheses, namely "(2)", indicates that this is the second wafer of the concurrently processed two wafers. Therefore nearly eighty wafers have been fabricated in this research. The last digit in the square parentheses, namely "[3]", locates the position of the designated device among a total of eight devices on each wafer. Figure 4.1 shows the locations of all the eight devices on a wafer. In some cases, devices were cut separately from each other for different experimental treatments.

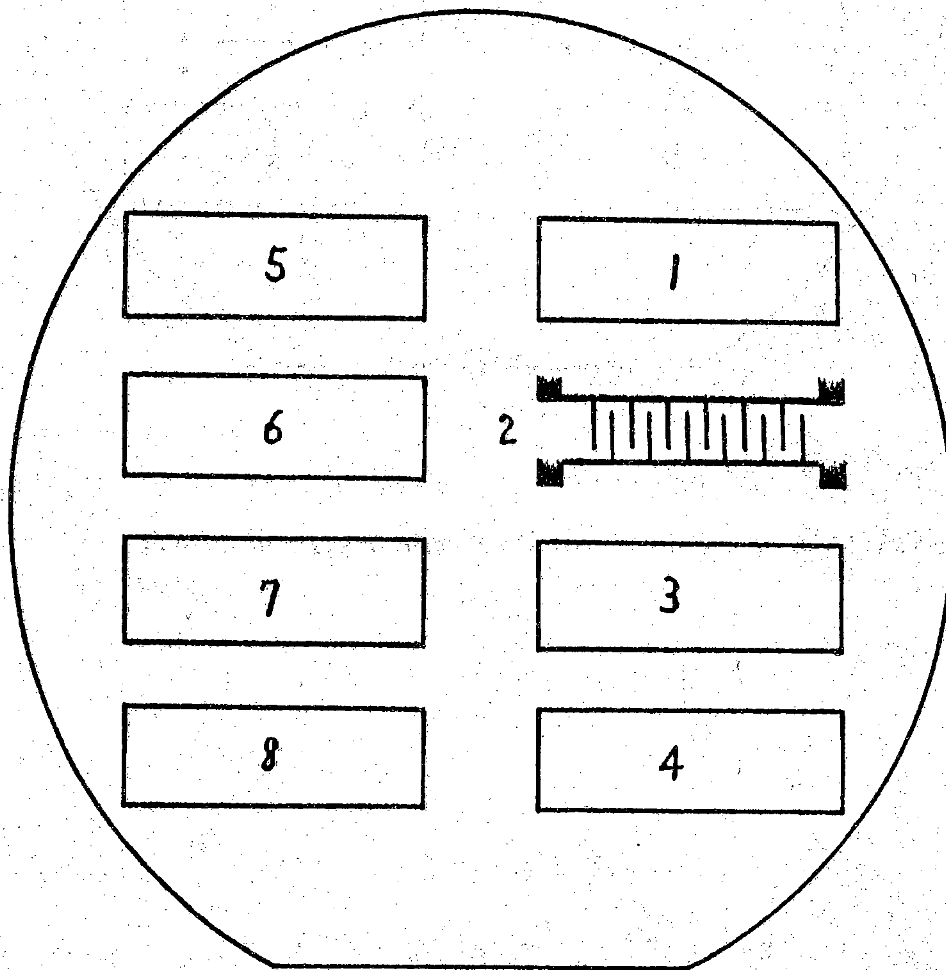

Figure 4.1 Schematic representation of the locations of eight devices on a wafer

4.1 Results of Some Experiment Measurements

STRUCTURE

X-ray diffraction studies were made to verify that the films were amorphous. Because of the lower absorption coefficient of silicon, films of at least 10 microns were needed to get a sufficient difracted signal to be detected. Due to the lower evaporation rate(<5 Å /sec) used, it was not feasible to deposit films thicker than 2 — 3 microns. Moreover thicker films crazed and did not adhere to the substrates.

Silver coated quartz crystals, which were used as the sensor for the thickness monitor, had films of at least 10 microns thick. these films were deposited at an average rate of 5 Å /sec on the water cooled quartz crystals. The main difference between the films on the Ag coated quartz crystals and the films on the oxidized silicon wafers was the nature of the substrates. Thermally grown silicon dioxide is amorphous whereas the film on a quartz crystal is polycrystalline. A film deposited under identical conditions is more likely to be amorphous on an amorphous substrate then on a polycrystalline substrate.If the thicker films on the polycrystalline substrate are amorphous, then the films on the amorphous substrates should indeed be amorphous.

Figure 4.2 shows the x-ray diffraction pattern of a 9 μ thick as — deposited silicon film on an Ag coated quartz crystal. The broad peak near 27° in 2θ is due to the diffraction of Cu Ka radiation from the <111> plane of Si. The second broad peak from the <220> plane can be seen around 53°. Complete lack of structure is indicated by the broad peak similar to that obtained by Brodsky et al.[119]. The two relatively sharp peaks shown are due to the diffraction from Ag films beneath the a-Si films. For comparison purposes, x-ray diffraction patterns from an Ag coated quartz crystal without

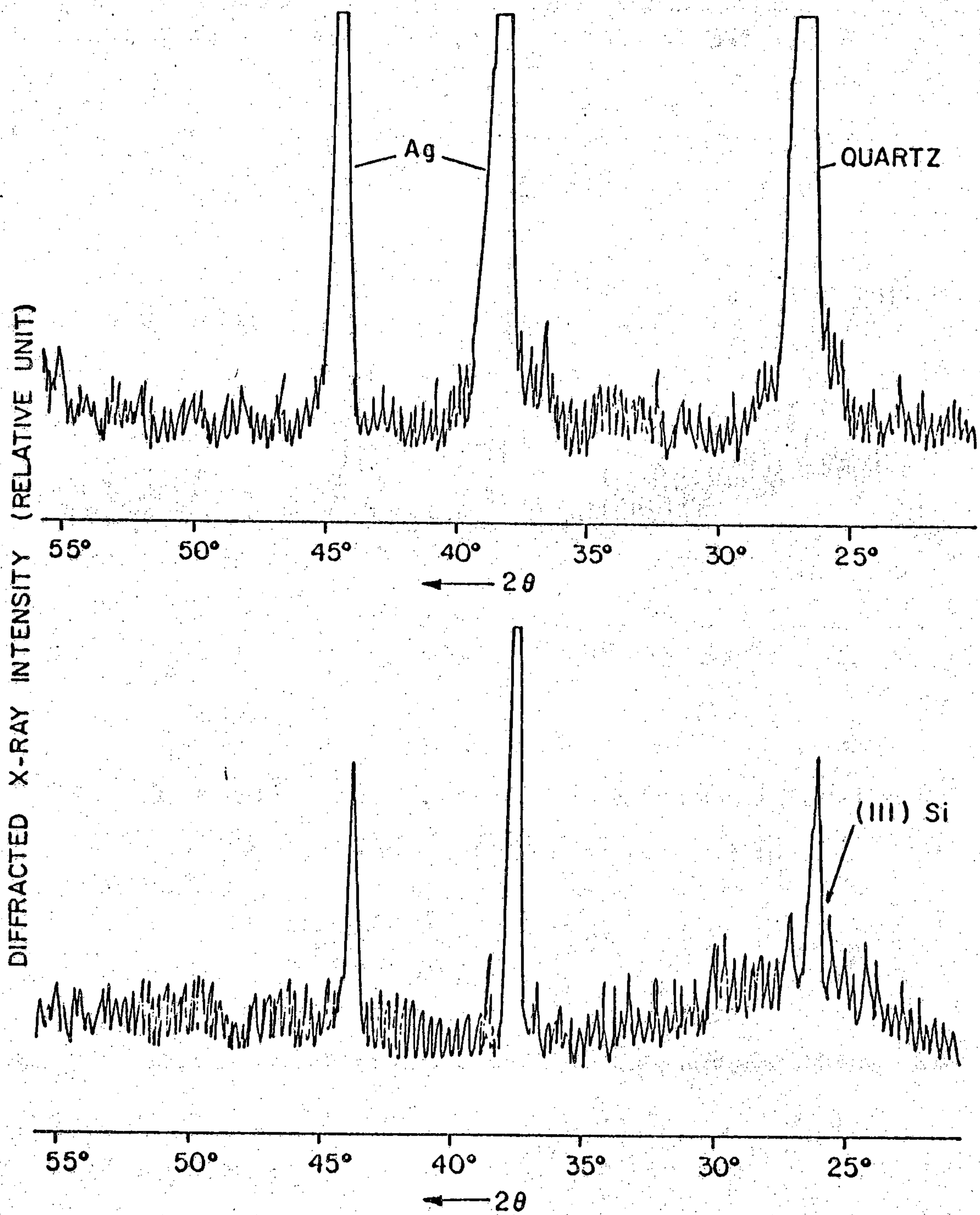

Figure 4.2 X-ray diffraction patten of: (a) 9 micron a-Si film deposited on Ag coated quartz substrate, (b) Ag coated quartz substrate.

any a-Si film is also shown in Figure 4.2(a). The film was then annealed in the vacuum for 4 hours at 400° C just as other films were annealed. The x-ray diffraction pattern from the annealed films are nearly the same as those shown in figure 4.2(b) for the as — deposited films. This indicates that all the Si films deposited on room temperature substrates and annealed for 4 hours at 400° are "x-ray amorphous".

RESIDUAL GAS ANALYSIS

The analysis of the residual gases in the vacuum system was used to determine what gases might be trapped in the amorphous thin film during evaporation and

the ambient conditions under which the film was being annealed.

The spectra scan 750, the analyzer used, identifies the various gas species in the vacuum system by ionizing some of the gas molecules. These ions are then passed through a mass filter which repeatedly scans through the mass range, periodically permitting ions with a specific charge to mass ratio to pass while restricting other ions with a different charge to mass ratio. The filtered ions are collected and a signal proportional to the collected ion current is displayed on a time base which is the same base used to scan the mass range.

The analyzer was used in a slow scan mode and the output was detected with an electrometer. The output of the electrometer was fed into a strip chart recorder to get a permanent record of the analysis. Figure 4.3 shows the strip chart record of the residual gas analysis before evaporation and during an annealingcycle. The plot is the intensity of the peaks due to ionized gases versus the mass of the ionized species. The intensity of the peaks is related to the amount of the gas present, but in this research no quantitative analysis was made of the amount of the species present. The horizontal scale, which is

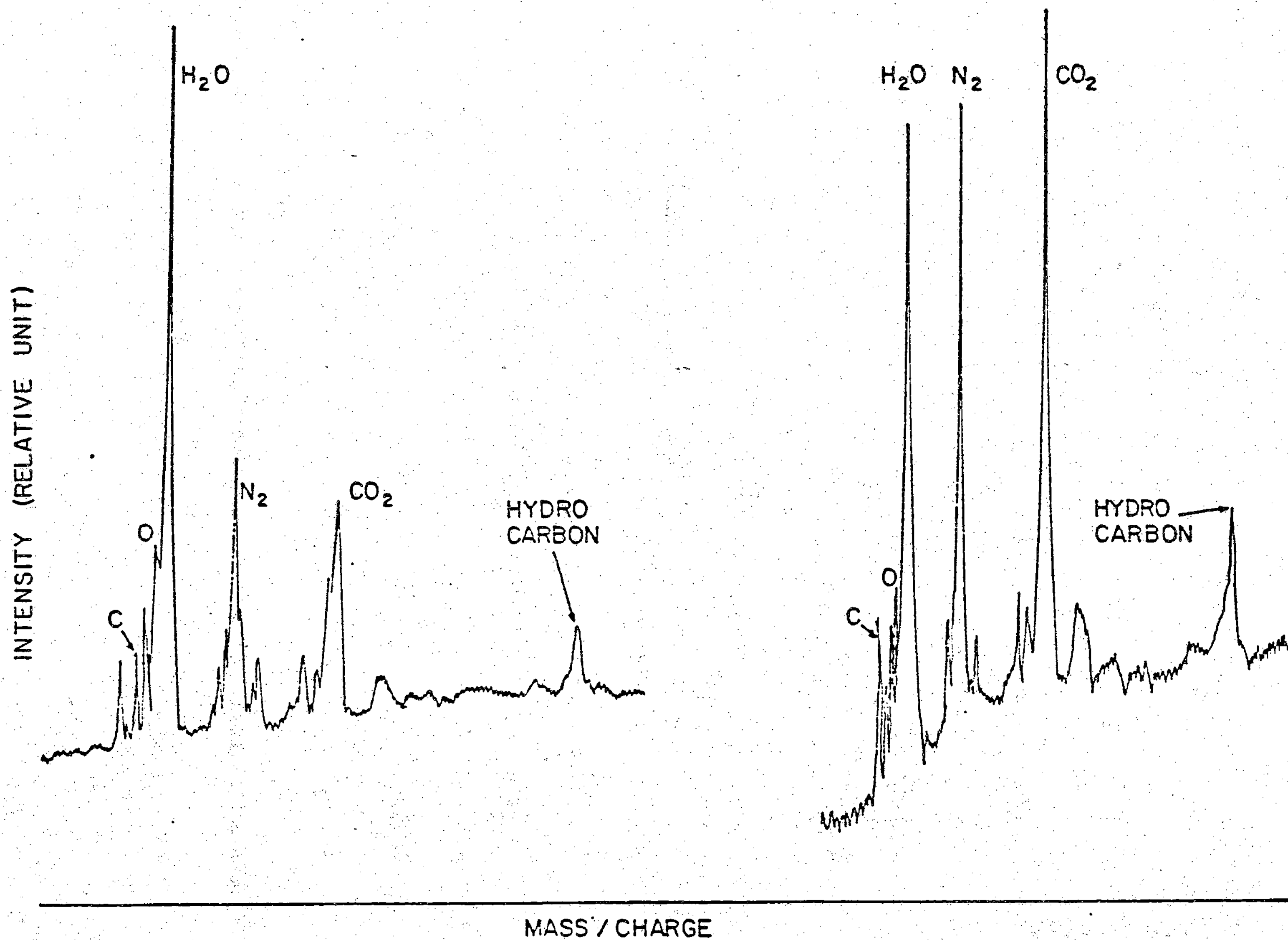

Figure 4.3 Residual gas analysis (a) before evaporation, (b) during the annealing cycle

related to the mass of the gas ions, was calibrated by bleeding nitrogen into the vacuum system and observing the peak corresponding to the N_2 increase in intensity. Once the nitrogen peak was determined, knowing the molecular weight of nitrogen and comparing the distance of its peak with other peaks with respect to the start of the scan, molecular weights of other gases present were determined and are labeled on each peak.

Before evaporation the gases contain mainly oxygen, nitrogen, carbon dioxide, water vapors, and some hydrocarbons, The intensity due to water vapor is the maximum which is not surprising since water is very hard to pump out the ion pumped vacuum system. The day the analysis was made, the relative humidity was around 65%. During annealing cycles nitrogen and carbon dioxide peaks increased considerably. This is probably due to the outgassing of the source and the chamber walls.

The residual gas analysis shows that the gases present in the vacuum system before evaporation and during the annealing cycle are typical laboratory gases which are commonly found in vacuum systems. No quantitative analysis of the amount of gases present was conducted.

4.2 Amorphous Silicon with Vacuum Annealing and Thermal Etching at 400°C

The field effect measurement was attempted on an unannealed sample deposited at a 4.0 Å /sec. With no measureable change in source to drain current as shown in figure 4.4. The Al contacts were removed and the sample annealed at 230° C for 3 1/2 hours. The field effect conductance modulation was then observed. A second sample, deposited at the same initial rate, was annealed for 2 hours at 400° C. As shown, several orders of magnitude change in the source to drain current was observed. A third film of the same deposition rate was annealed for 1 hour at 400° C, then an additional 1 hour, and then an additional 2 hours. The field effect curves showed little additional conductance modulation after the initial 1 hour 400° C anneal. Direct anneals of 8 and 12 hours at 400° C were performed but again the shape and values of conductance change remained essentially as before.

The initial films were deposited without thermal etching of the substrate prior to deposition. If the thermal etching was performed, the deposition was started a wait of five to six hours. The unetched films showed a time dependence in the source drain current after a change in the gate voltage, i.e., there was a decrease in the source drain current with time after an increment in the gate voltage as shown in figure 4.5. The steady state was reached in about 30 minutes and the steady state current vs. gate voltage plots showed hysteresis as illustrated by figure 4.6. When the film was deposited after thermal etching and the time between the deposition and the thermal etching was less then 2 hours, typically one hour, only one minute was needed to reach steady state. There was a decrease of about 10% from a peak value in the source drain current after a change in the voltage. Hysteresis in the field effect

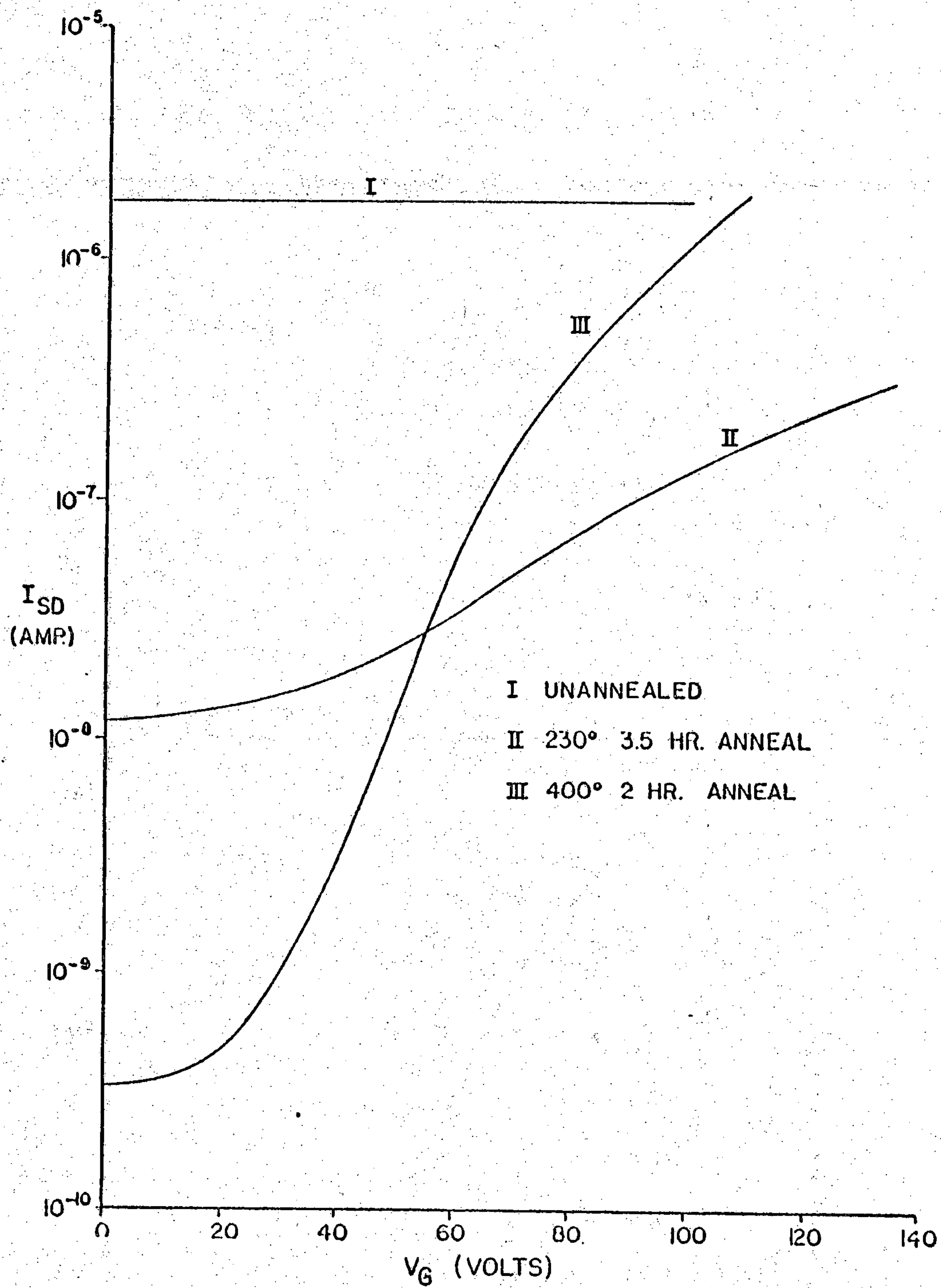

Figure 4.4 Effect of annealing on the conductance change due to field effect

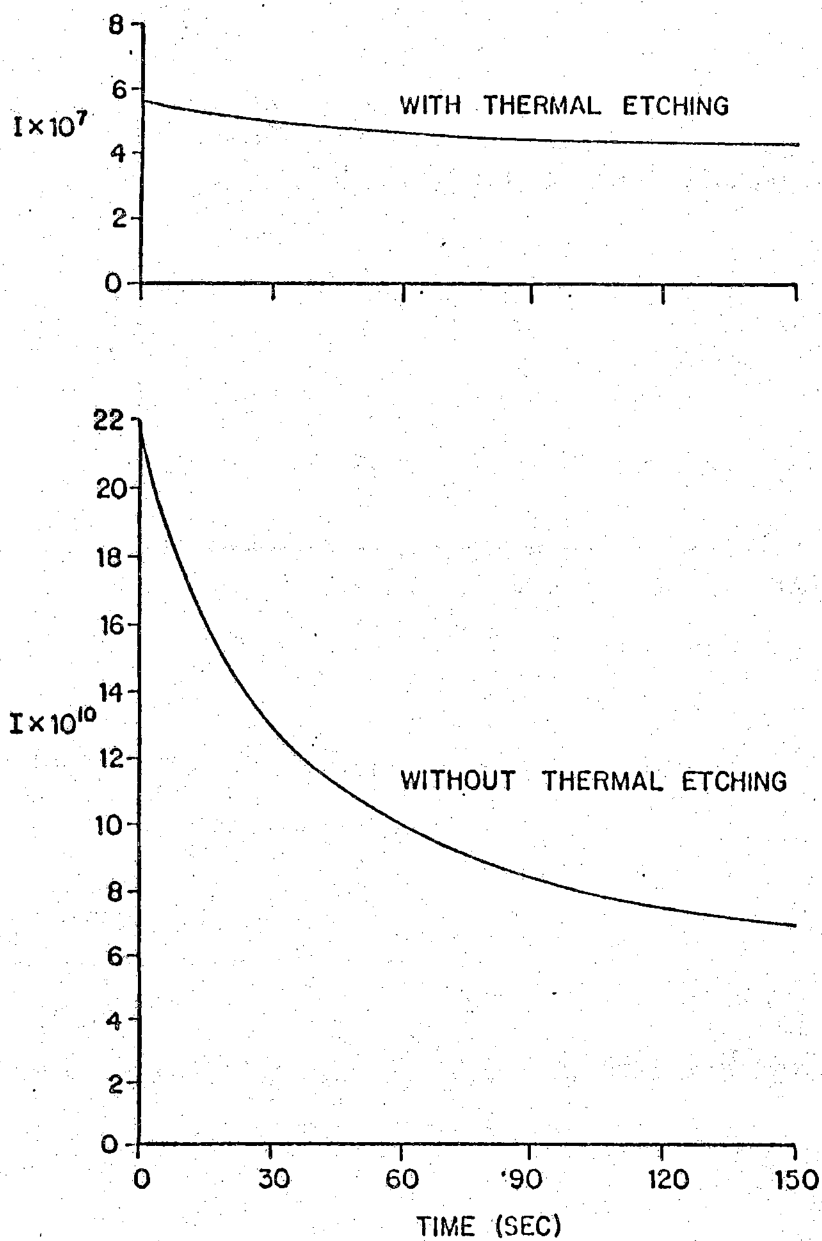

Figure 4.5 Soure-drain current as a function of time with and without thermal etching

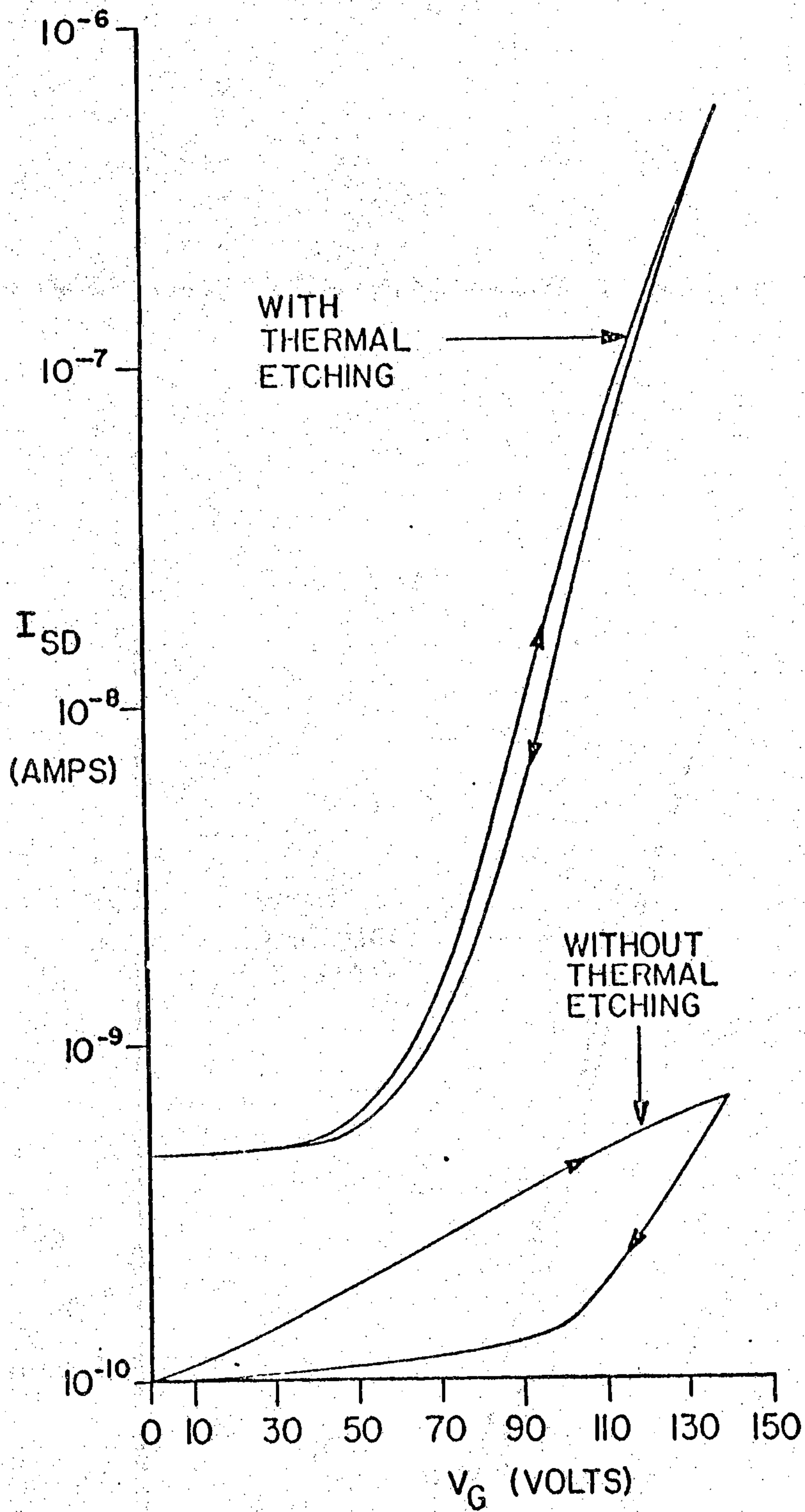

Figure 4.6 Field effect conductance change with and without thermal etching

curve was also reduced to a negligible amount. (Figure 4.5 and 4.6 illustrates the reduction.) Therefore, the thermal etching and the annealing at 400° C were made an integral part of the sample preparation procedure.

4.3 Hydrogenation Implants versus Nonhydrogenation

In this section, strong experimental evidence of hydrogen incorporation into the a-Si film by ion implantation technique is demonstrated. A comparison of the field effect conductance change between the devices which were hydrogen implanted and those which were not implanted with hydrogen clearly confirms the reduction of the density of states in the mobility gap by hydrogen incorporation. None of these devices were *in situ* thermally annealed. Therefore the results are totally due to the effect of hydrogen participation.

Device 31*-(2)-[8] and device 31*-(2)-[3] are two separate devices fabricated on the same wafer. Device 31*-(2)-[8] was not subjected to ion implantation, but was thermally annealed at 230°C for two hours in the Marshall oven. No field effect conductance change is observed on the I_{DS} vs. V_G plot before or after annealing as illustrated by (1a) and (2a) in Figure 4.7. Device 31*-(2)-[3] was hydrogen ion implanted with a dosage of $5x10^{16}/cm^2$ and went through the identical post-implant thermal treatment as device 31*-(2)-[8]. Curve (3b) in Figure 4.7 shows that a large field effect conductance change occurs on this device. The larger the field effect conductance change on the device, the lower the density of states in the mobility gap. Comparing line (2a) with curve (3b)

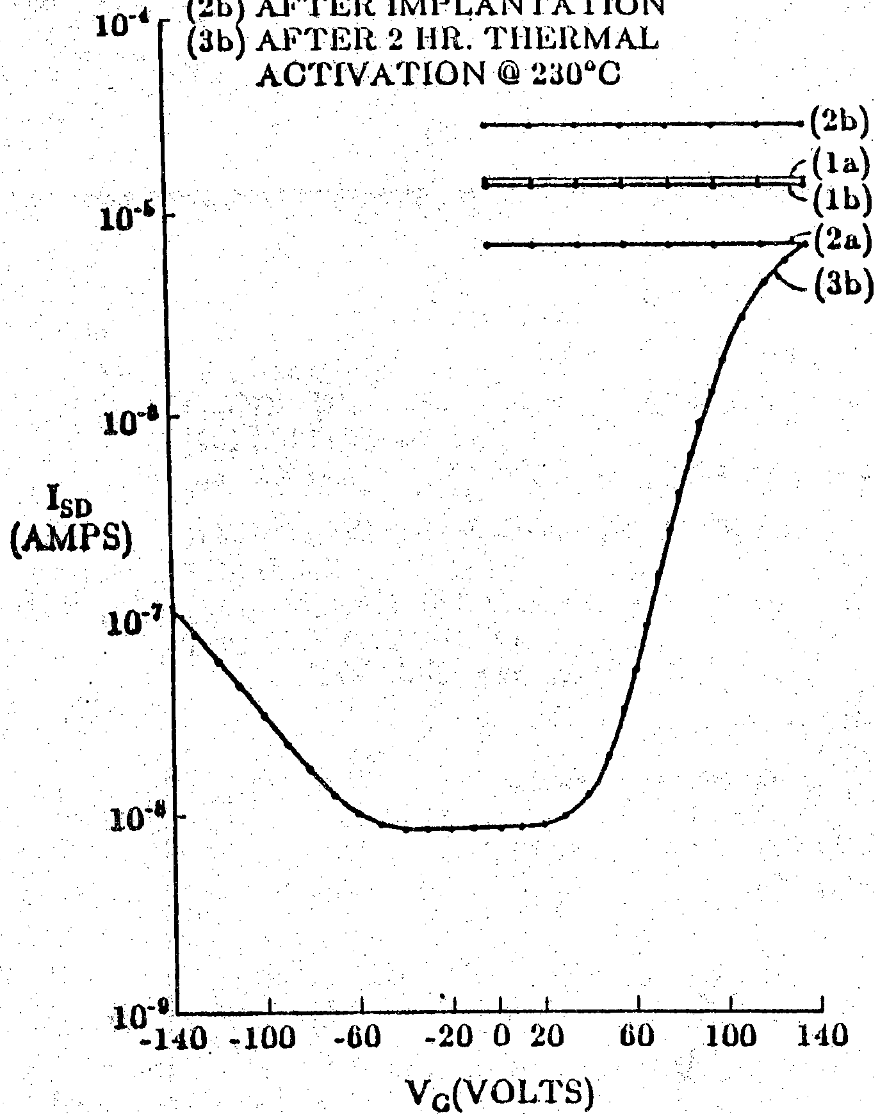

Figure 4.7 Field effect data of nonhydrogenated device 31*-(2)-[8] and hydrogenated device 31*-(2)-[3] with implant dosage $5 \times 10^{16}/cm^2$

very clearly demonstrates the role played by hydrogen in reducing the density of states in the mobility gap. Plots (1a), (1b), (2a), and (2b) show no conduction modulation because the density of localized states is too large. This large number of localized states tend to pin the Fermi level near midgap, which prevents significant band bending from occurring when gate voltage is applied. Hence no conductance change (I_{DS}) is observed. Reducing the density of localized states with hydrogen incorporation is different from that of thermal annealing. Thermal annealing, when performed at high temperatures (typically 400°C for 4 hours), on the nonhydrogenated a-Si film has the effect of healing the amorphous structure and removing most of the voids [120]. The proposed model for hydrogen incorporation depicts the activated hydrogen, through post-implant low temperature thermal annealing, as participating in the removal of localized defect centers in the mobility gap and forming either an antibonding state in the conduction band or a bonding state in the valence band [121]. The hydrogen incorporation and activation into the amorphous silicon structure has reduced the density of localized states in the mobility gap to a lower level. Hence band bending is now much easier to achieve when gate voltage is applied. Therefore large conductance changes (I_{DS}) are observed. To acquire similar results, thermal annealing alone requires a much higher temperature [51] (400°C) for a longer time (4 hours) than does hydrogen activation (230°C, 2 hours).

Incidentally, good uniformity and excellent initial data consistency of the a-Si film produced by this technique is clearly illustrated by plots (1a) and (1b) in Figure 4.7. This fact is also shown by the plot (1) in Figure 4.8 which demonstrates the results of different samples. All these confirm the statement in Chapter 1 which says the a-Si film produced by this technique has good

uniformity and consistency from device to device and from wafer to wafer as compared with glow discharge produced a-Si film.

4.4 Field Effect Conductance Change after Hydrogenation

In this section, field effect conductance changes after hydrogenation are further demonstrated and discussed. Figure 4.8 shows the field effect curves of device 37*-(1)-[3], which was hydrogen ion implanted with a dosage of $1.5\times10^{17}/cm^2$. Curve (1) and curve (2) are the data taken after fabrication and implantation respectively. Both curves are flat lines which show no conductance change with applied gate voltage. It is found that the level of flat line (2) is lower than that of line (1) if the implant dosage is above $1\times10^{17}/cm^2$. The reverse situation is observed if the implant dosage is below $5\times10^{16}/cm^2$ as illustrated by line (1b) and (2b) in Figure 4.7. This indicates that implantation with a lower dosage slightly increases the density of gap states, while implantation with a higher dosage decreases the density of gap states. This observed differences might be due to two factors, namely hydrogen passivation and radiation damage compete with each other during implantation. In the case of higher implant dosage, more substitutional hydrogen passivation takes effect even before hydrogen activation is performed and hence suppresses the small radiation damage effect which appears more pronounced in the case of lower implant dosage. The conduction mechanism for line (1) and line (2) in Figure 4.8 is variable range hopping in the localized states. So is line (1a), (2a),

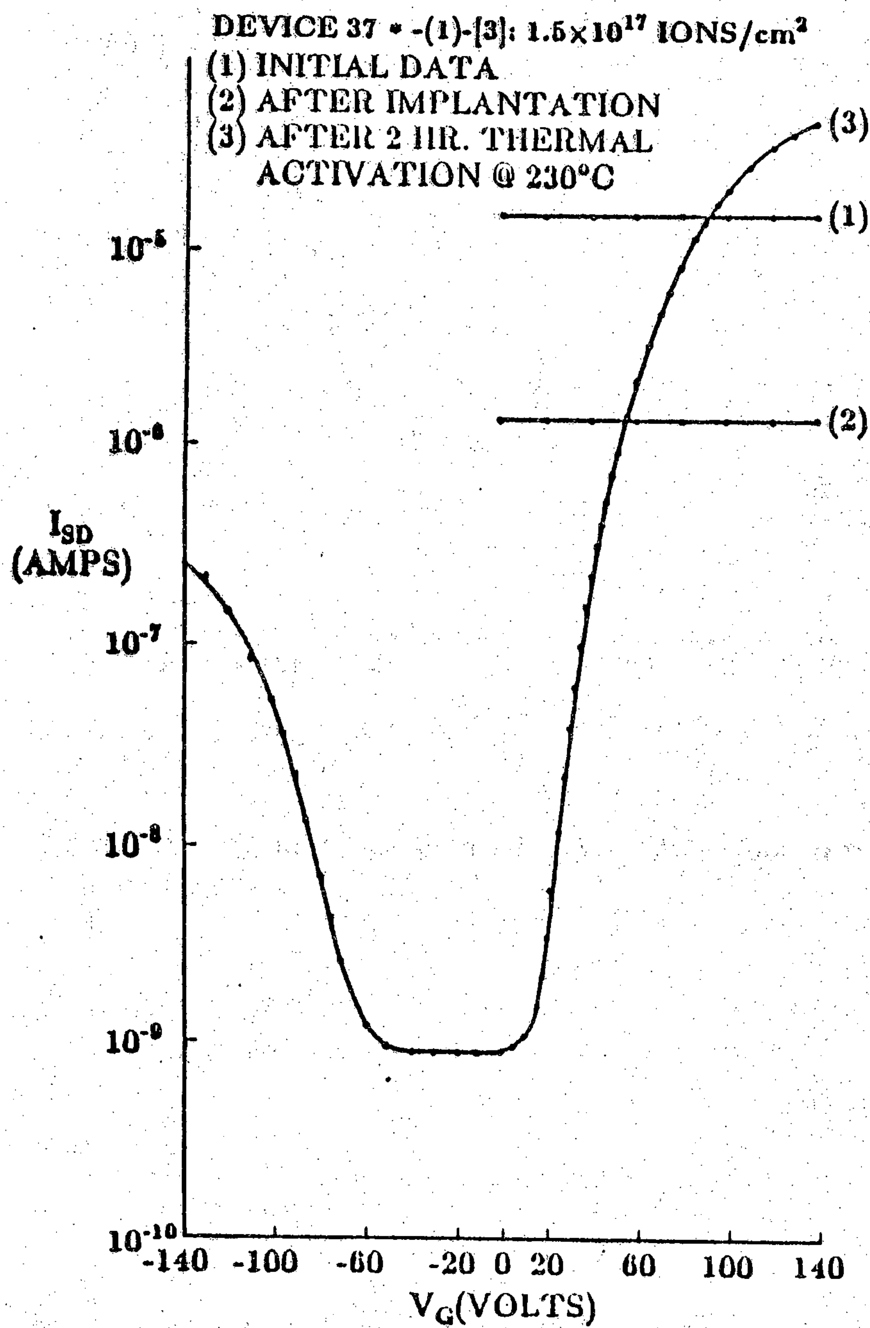

Figure 4.8 Field effect data of device 37*-(1)-[3] with hydrogen implant dosage $1.5\text{x}10^{17}/\text{cm}^2$

(1b), and (2b) in Figure 4.7. The upper limit of the density of states is about $10^{22}/cm^3$-eV as analyzed by applying Mott's Hopping Theory [45,58,59].

After low temperature thermal activation at 230°C for two hours, four orders of magnitude conductance change was observed as illustrated by curve (3) in Figure 4.8. This is the first evidence demonstrating the difference in the field effect characteristics before and after the a-Si films have been hydrogenated. Using glow discharge produced films already incorporating hydrogen, Goodman [24] demonstrated similar changes in field effect characteristics by expelling hydrogen from the film through thermal annealing at high temperatures. The conclusion of both Goodman's experiment and this experiment, while conducted in reverse, is that the presence of hydrogen lowers the density of localized states and thus accentuates the field effect variation. In Figure 4.8 the field effect response after thermal activation appears for both positive and negative gate voltages, but is asymmetric about zero due to the difference of electron and hole mobilities [52]. The plot is not centered about V_G=0 due to fixed charge at the Si-SiO_2 interface or in the oxide. The field effect curve tends toward saturation in the high field region (beyond ± 100 volts). This saturation is partly due to the degradation of the carrier mobility in the high electric field region and partly because of the increasing density of localized states at energies sufficiently away from mid-gap. In very low density of localized states films that are very thin, depletion could penetrate through the a-Si film.

If we assume that all the implanted hydrogen remains in the a-Si film, the atomic percentage of hydrogen content is about 45% for this dosage. H/Si ratio is 0.8, that is, for every five Si atoms present in the amorphous layer, four hydrogen atoms are present. Among the available published papers

[82,111,122-124], hydrogen contents of 5 - 50 at.% have been reported in the films prepared by the glow discharge decomposition of silane gas. The evaporation produced a-Si is quite porous, therefore a lot of hydrogen may reasonably be incorporated interstitially in the film.

The concentration profile of implanted hydrogen in a-Si is essentially that of a Gaussian distribution [117] with a projected range of around 1600 Å and a projected standard deviation of about 600 Å [118]. Because of the thin a-Si film and the minimum implant energy available, some of implanted hydrogen passes through the a-Si film and into silicon dioxide insulator which is about 3000 Å thick. Some hydrogen might even reach the SiO_2 - Si interface. In order to increase the implanted hydrogen in the a-Si, a thin film of photoresist overcoating is suggested.

4.5 Influence of Implantation Dosage on the Reduction of Localized States

Figure 4.9 shows the field effect curves of four devices with different implantation dosages while all other experimental parameters are kept fixed. As the implantation dosage is increased, the amount of conductance change for both positive and negative gate voltages increases, indicating a reduction in the localized states. Also the conductivity at zero gate voltage decreases and the width of the flat portion of the plot (nearly no conductance change region) decreases.

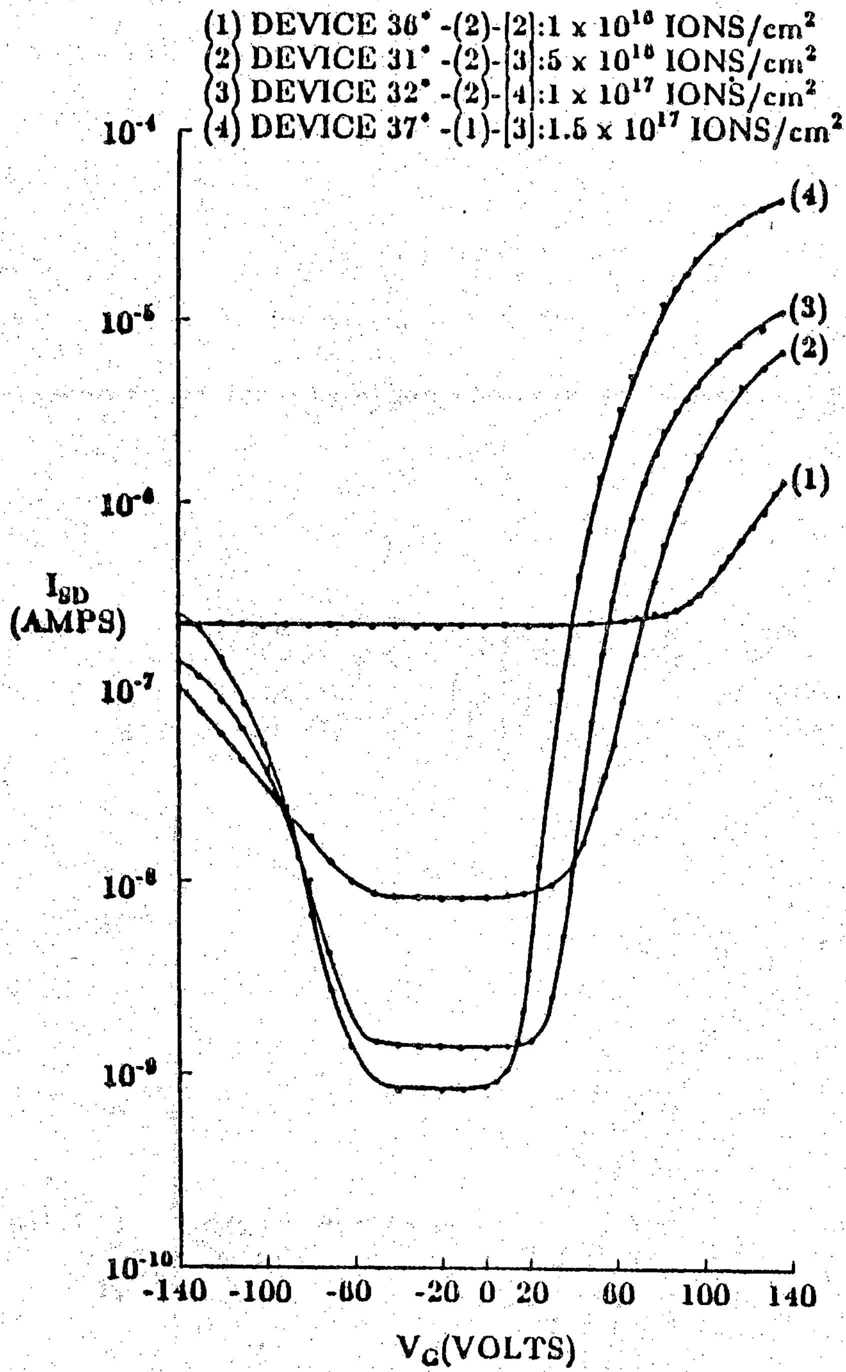

Figure 4.9 Effect of four different ion implantation dosage of hydrogen on field effect curves in amorphous silicon

A computer program [101,102], which uses both an iterative predictor-corrector algorithm and finite temperature statistics to numerically solve Poisson's equation, has been used to analyze the field effect data to determine the density of localized states (N_T^F) near the Fermi level. The computer program and information on how to run the program are presented in Appendix 2. The theory behind this program is basically the same as that presented in Chapter 2, section 2.5 except that this program uses finite temperature Fermi statistics while the analysis in section 2.6 uses the limiting case of Fermi function at T=0°K to calculate the charge density for Poisson's equation. The predictor-corrector computer algorithm is employed in the program to find the distribution of the density of states in a-Si. The main points of the program are outlined below. In order to be consistent with the computer program, some notation used here is a little different from that used in Chapter 2, section 2.5.

The application of a non-zero field across the sample bends the mobility edges of the conduction and valence bands of the a-Si down or up respectively for positive or negative gate voltages, V_F. The potential distribution inside the a-Si material, V(x), is determined by the solution of Poisson's equation :

$$\frac{d^2V(x)}{dx^2} = \frac{4\pi e}{\epsilon_s}\rho(x) \tag{4.5.1}$$

where x is the distance inside the a-Si from the a-Si-insulator interface.

The charge density, $\rho(x)$, is given by the energy integral over the density of states,, N(E), using finite temperature Fermi statistics :

$$\rho(x) = \int_{-\infty}^{\infty} N(E)[f(E-eV(x))-f(E)](dE) \tag{4.5.2}$$

where f is the Fermi-Dirac function at temperature T, i.e.

$$f(E)=\frac{1}{1+\exp((E-E_F)/kT)}$$

The program uses numerical techniques to do this finite temperature Fermi statistics calculation which is demonstrated from the numbered lines 42 to 49 of the program provided in Appendix 2.

Poisson's equation is subject to the boundary conditions that V(x) must approach zero with zero slope at some finite x; and

$$V_o' = \left.\frac{dV(x)}{dx}\right]_{x=0} = \frac{-(V_F-V_o)}{d}\frac{\epsilon_i}{\epsilon_s} \tag{4.5.3}$$

where V_o is the voltage at the a-Si-insulator interface, d is the thickness of the insulator and ϵi, ϵs are the dielectric constants of the insulator and a-Si, respectively. This boundary condition is due to the continuity of the normal component of the electric displacement at the interface. The validity of equation (4.5.3) is based on the assumption that there is no real charge trapped in the insulator or at the interface plane.

Using our first guess for N(E), the program solves Poisson's equation, equation (1), with a predictor-corrector computer algorithm to find V(x) which satisfies the boundary conditions. The final V(x) is inserted into the following equation of the induced change in conductance to obtain $G(V_F)$ and this is compared with the experimental data.

$$\frac{G-G_o}{G_o}=\frac{\alpha}{\alpha+1}\frac{1}{t}\int_o^t dx\,[\exp(eV(x)/kT)-1]+$$

$$\frac{1}{\alpha+1}\frac{1}{t}\int_o^t dx\,[\exp(-eV(x)/kT)-1] \tag{4.5.4}$$

where G_o is the total conductance when the energy band is in a flat situation.

"t" is the thickness of the a-Si and "α" is the ratio of the contribution by electrons to that by holes. Note that in Chapter 2, section 2.5, the expression

$$\frac{\Delta G_s}{G_{so}} = \frac{\alpha \Delta n + \Delta p}{t(\alpha n_b + p_b)}$$

is the same as equation (4.5.4) above if $n_b = p_b$ and Δn, Δp are presented in the integral forms which were given by equations (2.5.9) and (2.5.10) respectively in Chapter 2, section 2.5.

The integral for G in equation (4.5.4) is valid only if the band bending caused by the applied field shifts all localized states rigidly with V(x) without a change in their carrier mobility parallel to the surface. It is further assumed that the only effect of interface states is to create a nonzero flat band voltage, V_{FB}. In order to match the boundary condition, equation (4.5.3), the effect of flat band voltage is taken care of in the program by VFIELD = VDATA(NVF)-VFBP (see Appendix 2, numbered line 61 of the program). The program compares the calculated conductance (G_{calc}) with the experimental values of G (G_{data}), modifies N(E) accordingly and starts again by solving Poisson's equation with the new N(E). This iterative process is repeated until the average fractional error of G_{calc} relative to the experimental data is less than the experimental uncertainty or a preset limit (typically around $\pm 5\%$). The solution is then considered to have converged and N(E) is not modified further.

For the first guess of N(E), it is best to begin by trying to find the N(E) near E_F which gives the correct $G(V_F)$ near V_{FB}, and to then progressively work out to higher values of $|V_F - V_{FB}|$ and of $|E - E_F|$. If the initial guess is too far away, the program will show signs of divergence. This happened in the course of this research when the experimental data were analyzed. Figure 4.10

shows a flow chart for the computer program which derives N(E) from $G(V_F)$.

This computer program was used to analyze the experimental data shown in Figure 4.9. Figure 4.11 demonstrates the effect of hydrogen implant dosage on the reduction of the density of localized states in a-Si films. N_T^F after hydrogenation decreases from 8.6×10^{20} to $1\times10^{19}/cm^3$-eV as the implant dosage of hydrogen increases from 1×10^{16} to $1.5\times10^{17}/cm^2$.

The mechanism of hydrogen incorporation by implantation is different from that of the glow discharge of silane or sputtering deposition in the presence of hydrogen. In the implantation method, hydrogen was incorporated after the a-Si film had been deposited. The optical absorption data obtained by other researchers [117] suggest that the a-Si:H structure produced by ion implantation favors monohydride formation. In the glow discharge or sputtering method, hydrogen was incorporated in the film at the same time as the a-Si:H matrix was fabricated. The hydrogen content and the film properties are greatly related to the surface reaction during the deposition. Although most good quality glow discharge materials mainly have SiH [125], SiH_2 and SiH_3 groups may also exist [68,123,125]. In the glow discharge method, film properties are influenced by several deposition parameters, especially the substrate temperature during deposition [20,126].

Table 4.1 presents a summary of the fabrication parameters and selected electrical properties of the samples from which valuable information was abtained in the research.

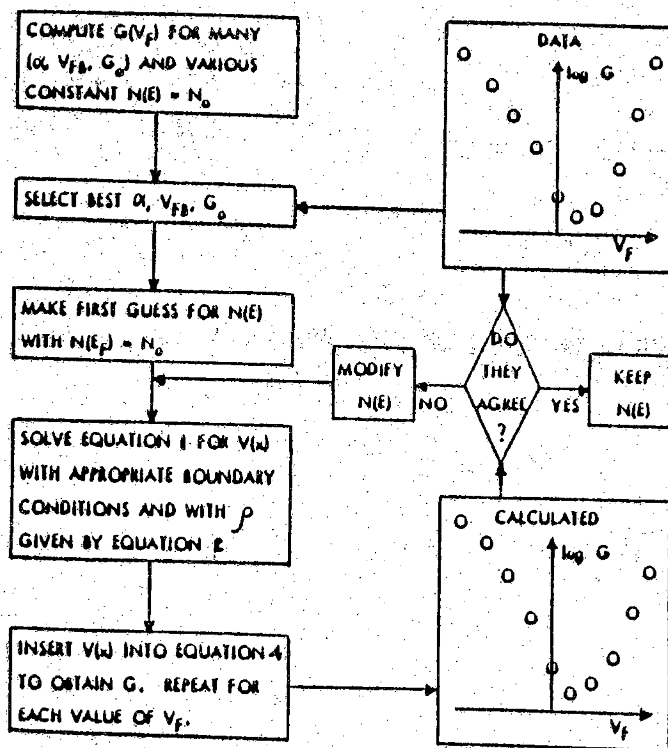

Figure 4.10 Flow chart of computer program to analyze field effect data

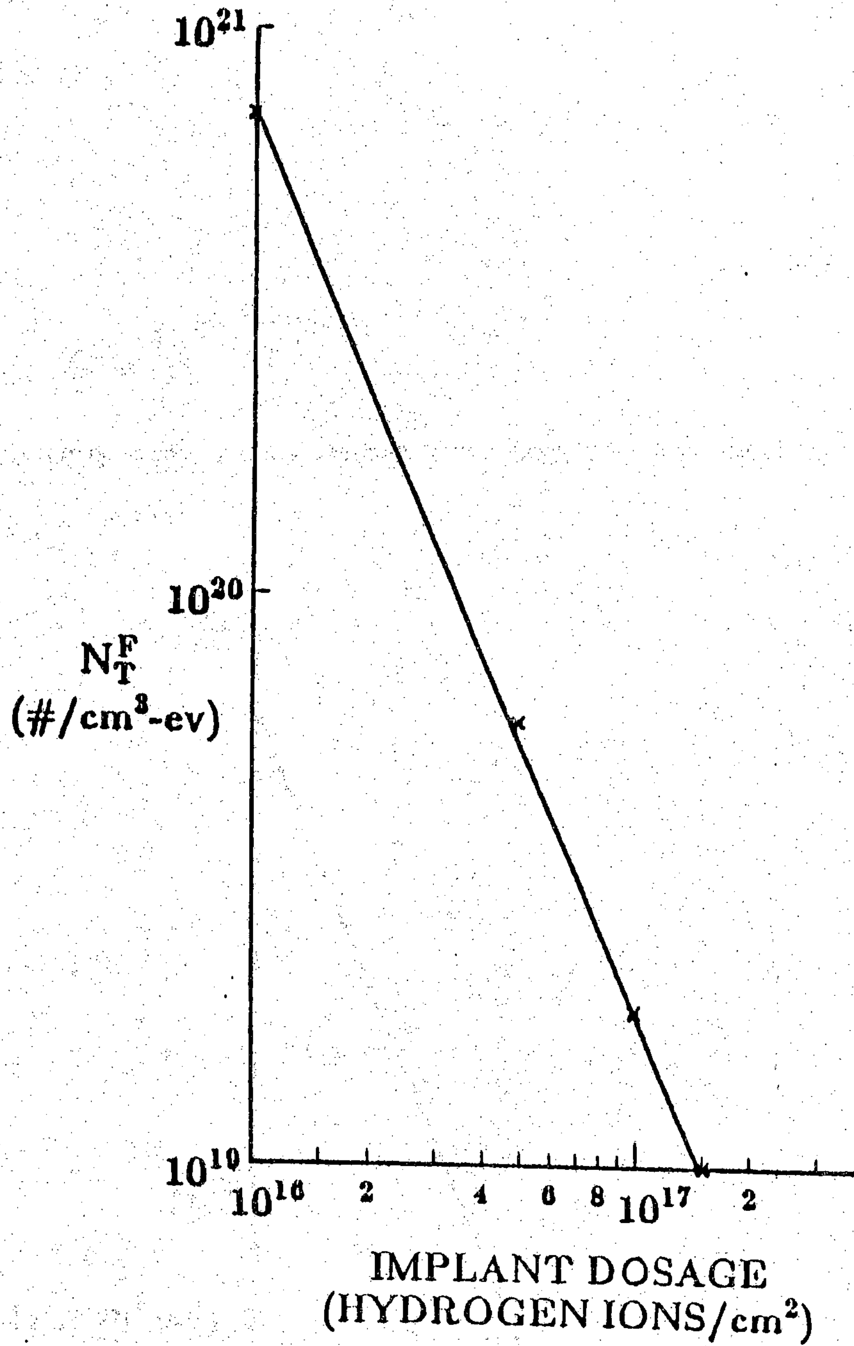

Figure 4.11 Effect of ion implantation dosage of hydrogen on density of localized states near E_F of amorphous silicon thin film

Table 4.1 Summary of fabrication parameters and Density of Localized States near the Fermi level of a-Si samples

Device No.	Oxide Thickness (Å)	a–Si Thickness (Å)	Base Press. (Torr)	Dep. Press. (Torr)	Dep. Rate (Å/sec)	Dep. Temp. (°C)	*in situ* Anneal Temp. & Time	Implant Dosage (ions/cm²)	Implant Chamber Press. (Torr)	Thermal Activation Temp. & Time	N_T^F (/cm³-eV)
31°-(2)-[8]	3100	750	7.6×10^{-8}	4.0×10^{-7}	3.0	196				@ 230 °C, 2 hr.	$\sim 10^{20}$
31°-(2)-[3]	3100	750	7.6×10^{-8}	4.0×10^{-7}	3.0	196		5×10^{16}	8.0×10^{-7}	@ 230 °C, 2 hr.	8.0×10^{19}
31°-(2)-[4]	3100	750	7.6×10^{-8}	4.0×10^{-7}	3.0	196		5×10^{16}	8.0×10^{-7}	@ 230 °C, 4 hr.	8.0×10^{19}
31°-(2)-[5]	3100	750	7.6×10^{-8}	4.0×10^{-7}	3.0	196		5×10^{16}	8.0×10^{-7}	@ 230 °C, 1 hr.	8.0×10^{19}
36°-(2)-[2]	3250	735	8.4×10^{-8}	6.2×10^{-7}	3.5	192		1×10^{16}	4.6×10^{-7}	@ 230 °C, 2 hr.	8.6×10^{20}
32°-(2)-[4]	3000	750	1.1×10^{-7}	5.8×10^{-7}	3.2	187		1×10^{17}	6.0×10^{-7}	@ 230 °C, 2 hr.	3.3×10^{19}
37°-(1)-[3]	3250	735	8.2×10^{-8}	4.2×10^{-7}	3.5	187		1.5×10^{17}	8.0×10^{-7}	@ 230 °C, 2 hr.	1×10^{20}
32°-(2)-[6]	3000	750	1.1×10^{-7}	5.8×10^{-7}	3.2	187		1×10^{17}	6.0×10^{-7}	@ 290 °C, 2 hr.	
31°-(1)-[2]	3100	710	1.0×10^{-7}	9.5×10^{-7}	3.0	180	@ 300 °C, 4 hr.	5×10^{16}	5.2×10^{-7}	@ 230 °C, 2 hr.	
39°-(2)-[3]	3250	950	6.8×10^{-8}	8.0×10^{-7}	3.0	180	@ 400 °C, 4 hr.	1×10^{17}	5.0×10^{-7}	@ 230 °C, 2 hr.	4×10^{17}

4.6 Hydrogen Effusion

In this section, time and temperature for the activation of hydrogen were determined based upon a series of experiments. The phenomenon of hydrogen effusion was found during the course of experiments.

With temperature fixed at 230°C during thermal activation, annealing times of 1, 2, and 4 hours have been used to activate the implanted hydrogen. Figure 4.12 shows the field effect curves of three separate devices used for this experiment. These three devices, 31*-(2)-[5], 31*-(2)-[3], 31*-(2)-[4] were fabricated and hydrogen implanted on the same wafer and then separated before they were thermally treated at 230°C for 1, 2, and 4 hours respectively. Nearly identical results were observed in the field effect data. Therefore time is not a critical factor in the activation process. With the time fixed at 2 hours, different activation temperatures of 200, 230, 260, 290°C were tested. The results were also nearly identical, except at 290°C. As shown in Figure 4.9, the field effect response of the 290°C activation is less than that of the 230°C anneal. The field effect data indicates that hydrogen starts to effuse out of the a-Si at 290°C, which results in a higher density of localized states. This phenomenon is in agreement with the results of Goodman [24] and other researchers [20,127,128], who reported that hydrogen effusion occurs during the annealing of glow discharge produced a-Si:H films at temperatures of around 300°C.

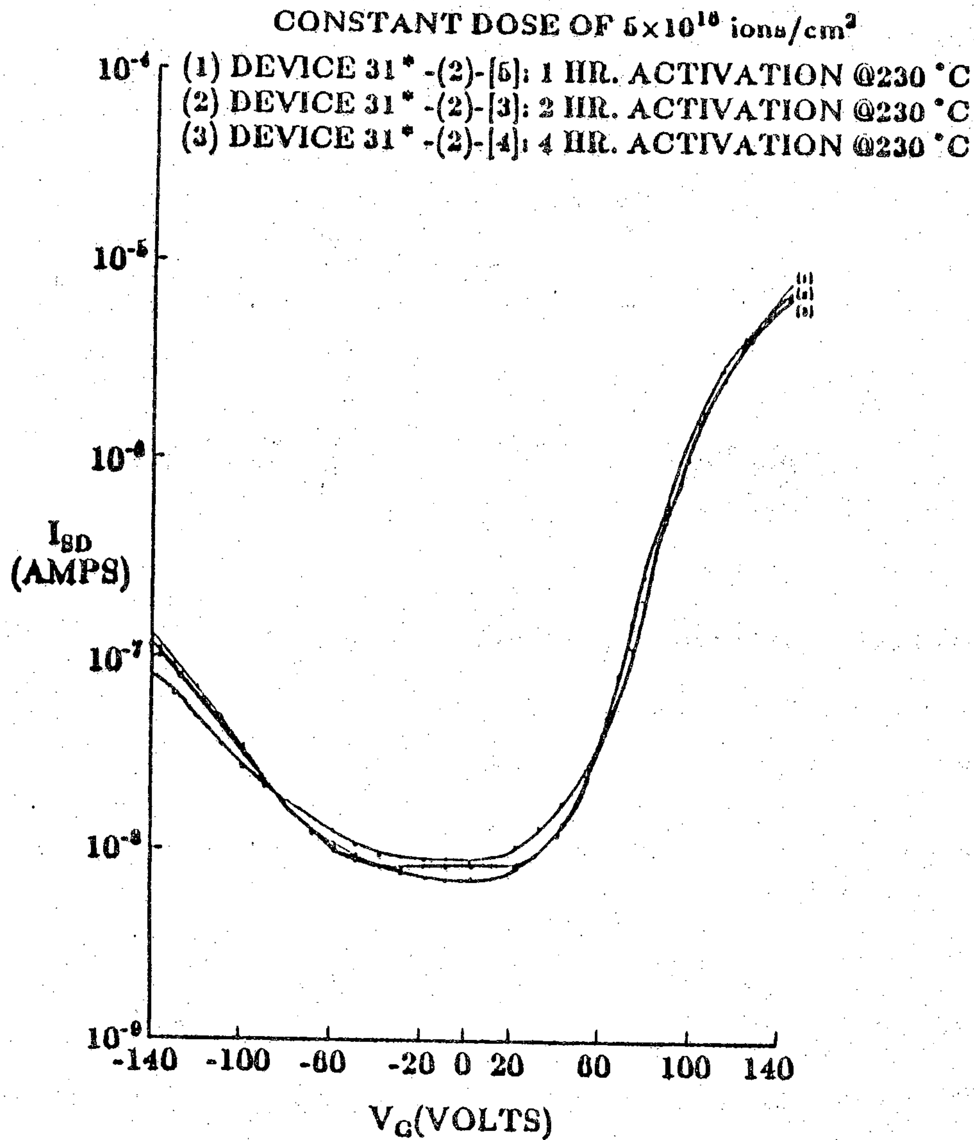

Figure 4.12 Field effect curves of three devices with fixed thermal activation temperature (230°C) but different annealing times of 1, 2, and 4 hours

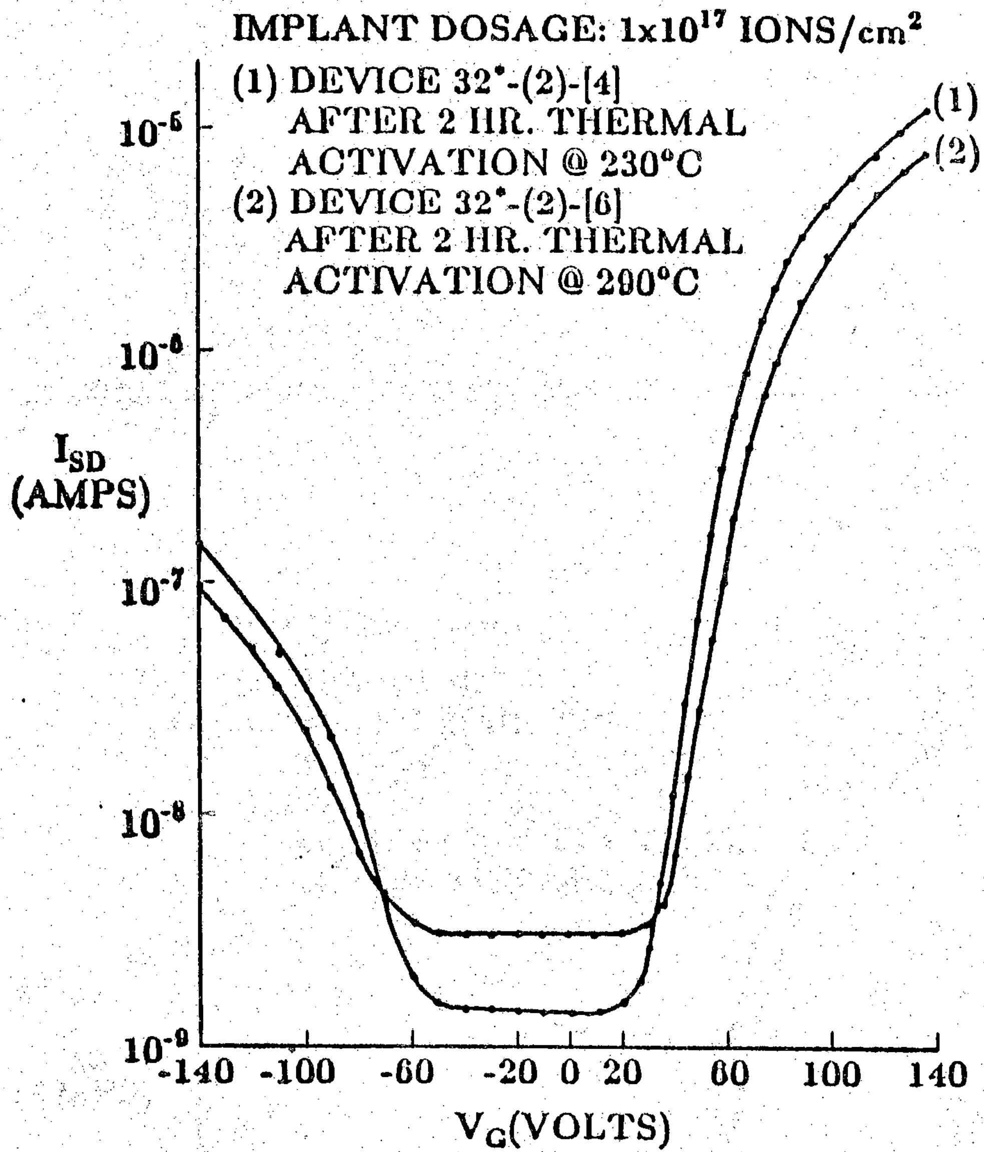

Figure 4.13 Field effect data of two devices with same implantation dosage ($1 \times 10^{17}/cm^2$) but different thermal activation temperature (230°C and 290°C)

4.7 Effect of pre-implant in situ Thermal Annealing on the Reduction of Localized States

All the results presented to this point were acquired on devices which were not subjected to *in situ* thermal annealing immediately following a-Si film deposition. In previous samples large amounts of hydrogen have been implanted into the electron beam vacuum evaporated a-Si film. However the density of localized states, although reduced drastically, remains large compared to high quality glow discharge produced material. Before these films can be useful for device applications, the density of localized states must be further reduced by several orders of magnitude. In this section, the effect of a pre-implant *in situ* thermal annealing on the reduction of localized states is demonstrated. The porous nature of vacuum evaporated a-Si is confirmed through this experiment.

The *in situ* thermal annealing was performed immediately following a-Si film deposition. An adjustable transformer was set to deliver a current of about 10 amperes to the substrate heater which was a coiled tungsten wire of 10 mils in diameter. The temperature of the substrate holder was monitored by a digital voltmeter (DVM) which was connected to a chromel-alumel thermocouple attached to the substrate holder. The DVM reading equivalent to 400°C was determined by referring to the thermocouple table which lists the temperatures and the corresponding thermoelectric values based upon 0°C reference junction. The table value must be corrected by a value corresponding to the measured room temperature. Usually, it took about 20 to 30 minutes for the substrate holder to reach the desired temperature. After 4 hours *in situ* thermal anneal, the heater current was turned off and the substrate was allowed to cool to room temperature before the wafer was removed from the vacuum system and taken to the ion implanter.

Figure 4.14 shows the field effect curves of I_{SD} vs. V_G for three devices with different *in situ* conditions while all other sample preparation procedures were held constant. Each had an implant dosage of 5×10^{16} ions/cm^2 and had a post implant thermal activation at 230°C for 2 hours. Device 31*-(2)-[3], (curve (1)), was not subjected to thermal anneal *in situ* after a-Si deposition. Device 31*-(1)-[2], (curve (2)), and device 39*-(2)-[3], (curve (3)), were thermally annealed *in situ* for 4 hours, immediately following film deposition, at 300°C and 400°C respectively. Comparing curve (1) with curve (3) clearly demonstrates that with the aid of *in situ* thermal annealing at 400°C, the field effect conductance change was improved by three orders of magnitude over the non-annealed device. Also illustrated in the figure is that the field effect conductance change is more pronounced for an anneal at 400°C than at 300°C.

It is known that evaporated amorphous materials are quite porous [129,130]. Fritzsche [131-133] and his coworkers have shown that the internal surfaces of the interconnected voids in a-Si are oxidized with substantial oxygen incorporation as soon as the film is exposed to air. It is believed that absorbed water vapor, which can not be removed, causes internal oxidation and prevents subsequent hydrogen-silicon bonds from forming, and hence prevents this hydrogenation technique from achieving its maximum effectiveness.

In this experiment, by means of thermal annealing *in situ*, the amorphous structure has been healed by partially removing the voids. Therefore the film has been made more impervious to water vapor and hence reduced the possibility of extensive internal oxidation. With less oxidation the subsequent hydrogenation effect is enhanced, resulting in a significant improvement in the field effect data which corresponds to a lower density of localized states.

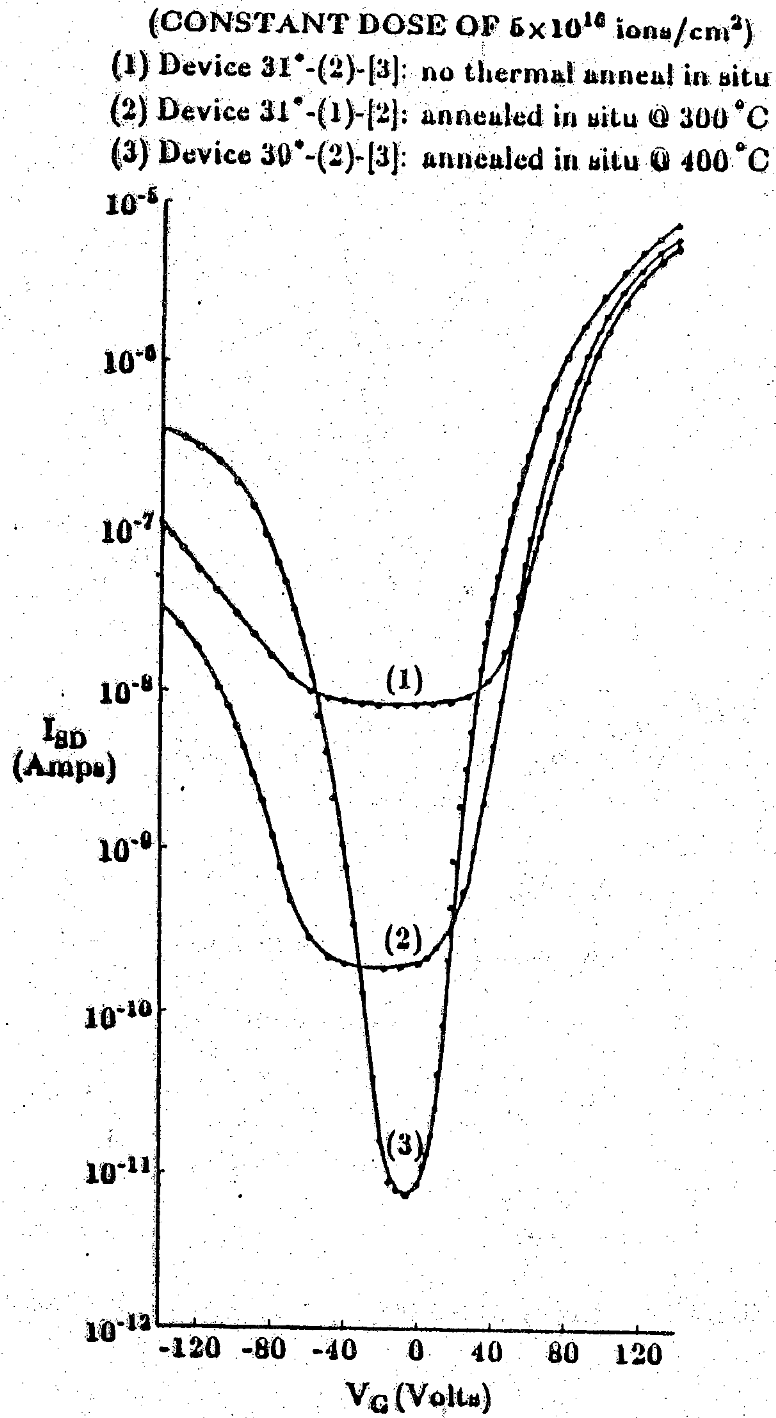

Figure 4.14 Field effect data for three devices with the same implant dosage ($5x10^{16}/cm^2$) but with different *in situ* thermal annealing conditions

Besides H.Fritzsche's [131-133] and the work presented here, other researchers also reported that micropores penetrated the structure of evaporated a-Si. J.C.Bean and J.M.Poate [134] have investigated the nature of these voids and their influence on the epitaxial crystallization rate of UHV evaporated amorphous silicon. They reported that crystallization was inhibited in samples exposed to air at room temperature due to the gas absorption on the internal surfaces of the voids.

Figure 4.15 illustrates the field effect curves of device 39*-(2)-[3], which was thermally annealed *in situ* at 400°C for 4 hours immediately following film deposition. The device was initially hydrogenated with a dosage of $5 x 10^{16}$ ions/cm^2, resulting in the field effect curve (2). Curve (3) is the data taken on the same device after it was subjected to a second hydrogen implant with a dosage of $5 x 10^{16}$ ions/cm^2 (total dosage on the device is $1 x 10^{17}$ ions/cm^2). Analysis of the data corresponding to curve (3) shows that the density of localized states near the Fermi level has been reduced from $7 x 10^{17}/cm^3$-eV to $4 x 10^{17}/cm^3$-eV. With this density of localized states a much improved a-Si thin film transistor (TFT) is possible [1].

Figure 4.16 illustrates how the localized states are distributed in energy around the Fermi level for device 39*-(2)-[3]. This plot is obtained from the output of the computer program being applied to the experimental data of Figure 4.15, curve (3). Note that the localized states are relatively constant near the center of the gap and increase at energies away from mid-gap.

Table 4.2, which contains some data from section 4.3, shows the effect of hydrogenation with different implantation dosages on the density of localized states. The data demonstrates quantitatively the effect of hydrogen implant dosage on the reduction of the density of localized states. The table also

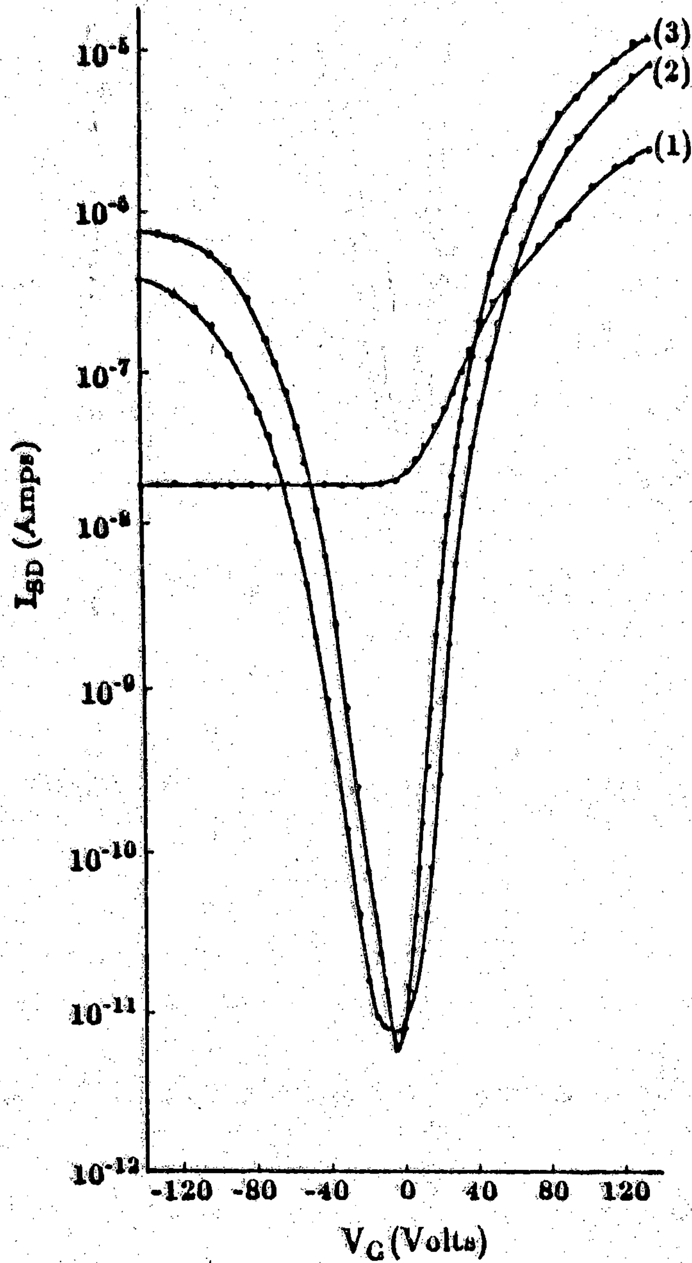

Figure 4.15 Field effect data of device 39*-(2)-[3]

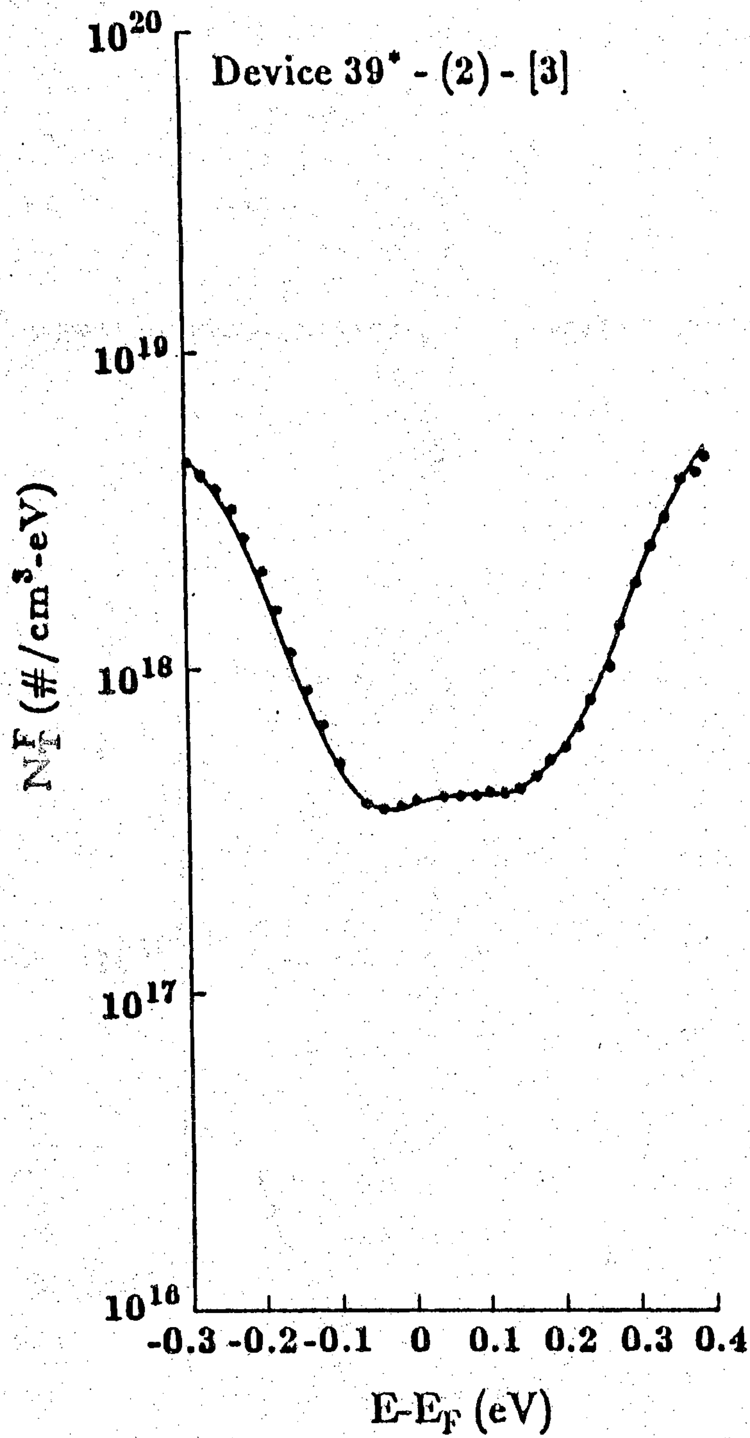

Figure 4.16 Density of localized states in the band gap for film 39*-(2)-[3] after hydrogenated to a dose of $1x10^{17}/cm^2$

Table 4.2 Summary of effects of *in situ* thermal anneal and hydrogen implant dosage on the Density of Localized States of a-Si samples

film	400 ° C anneal in situ	Implanted ions/cm^2	N_T^F/cm^3–eV
36*–(2)–[2]	NO	1×10^{16}	8.6×10^{29}
31*–(2)–[3]	NO	5×10^{16}	8.0×10^{19}
32*–(2)–[4]	NO	1×10^{17}	3.3×10^{19}
37*–(1)–[3]	NO	1.5×10^{17}	1×10^{19}
39*–(2)–[3]	YES	5×10^{16}	7×10^{17}
30*–(2)–[3]	YES	1×10^{17}	4×10^{17}

compares films with an *in situ* 400°C anneal with those which were not annealed.

4.8 Some Discussions on Surface States

Surface states at the Si-SiO_2 interface and at the amorphous silicon-SiO_2 interface are included in the field effect measurements. Surface states are of concern because a large density of surface states may easily mask the bulk localized state density of the a-Si. For example, suppose a density of surface states as large as ~ $10^{13}/cm^2$-eV exist at the SiO_2 - amorphous silicon interface. A density of ~ $10^{13}/cm^2$-eV is equivalent to a density of $1.3x10^{18}/cm^3$-eV bulk states in a thickness of the a-Si of 750 Å. Thus, surface states in the order of $10^{13}/cm^2$-eV can easily mask bulk densities which are less than $10^{18}/cm^3$-eV. The positive fixed charges at the interface can shield the electric field applied at the gate, thus weaken the electric field in the a-Si. Large gate voltages are needed to obtain sufficient energy band bending and start the onset of the conductance modulation, i.e. an increase of drain source current. Evidence of this occurring will appear in the I_{SD} vs. V_G plots as voltage shifts about V_G=0. In terms of crystalline silicon, this effect implies the increase of threshold voltage in a MOSFET. In addition, if surface states at the SiO_2 - amorphous silicon interface trap a large number of charge carriers, the conductance between drain and source will be degraded because of these trapped charges.

At the Si-SiO_2 interface these undesired surface states are greatly reduced with careful fabrication techniques. By using the quasi-static technique [135], the measured density of surface states at the Si-SiO_2 interface was determined to be in the range of 10^{10} to $10^{11}/cm^2$-eV [136]. Figure 4.17 shows the surface state distribution obtained from this measurement. Any radiation damage occurring during ion implantation with hydrogen is expected to be negligibly small, since the predominant energy loss mechanism is electronic stopping [137]. Nevertheless, most radiation damage will be annealed out by the post-implant thermal treatment.

Some questions arise concerning the surface states at the interface of the two amorphous materials (SiO_2 and a-Si). It is expected that some implanted hydrogen will reach the interface, passivate the interface dangling bonds, and hence reduce the surface states there. Since a field effect conductance change of six orders of magnitude has been observed in this experiment, it seems reasonable to assume that surface states at the a-Si:H-SiO_2 interface are close to a value of $10^{11}/cm^2$. This value has been reported to be an upper limit of the surface states at the interface as obtained from photoemission studies by Williams, Varma, Spear, and LeComber [138].

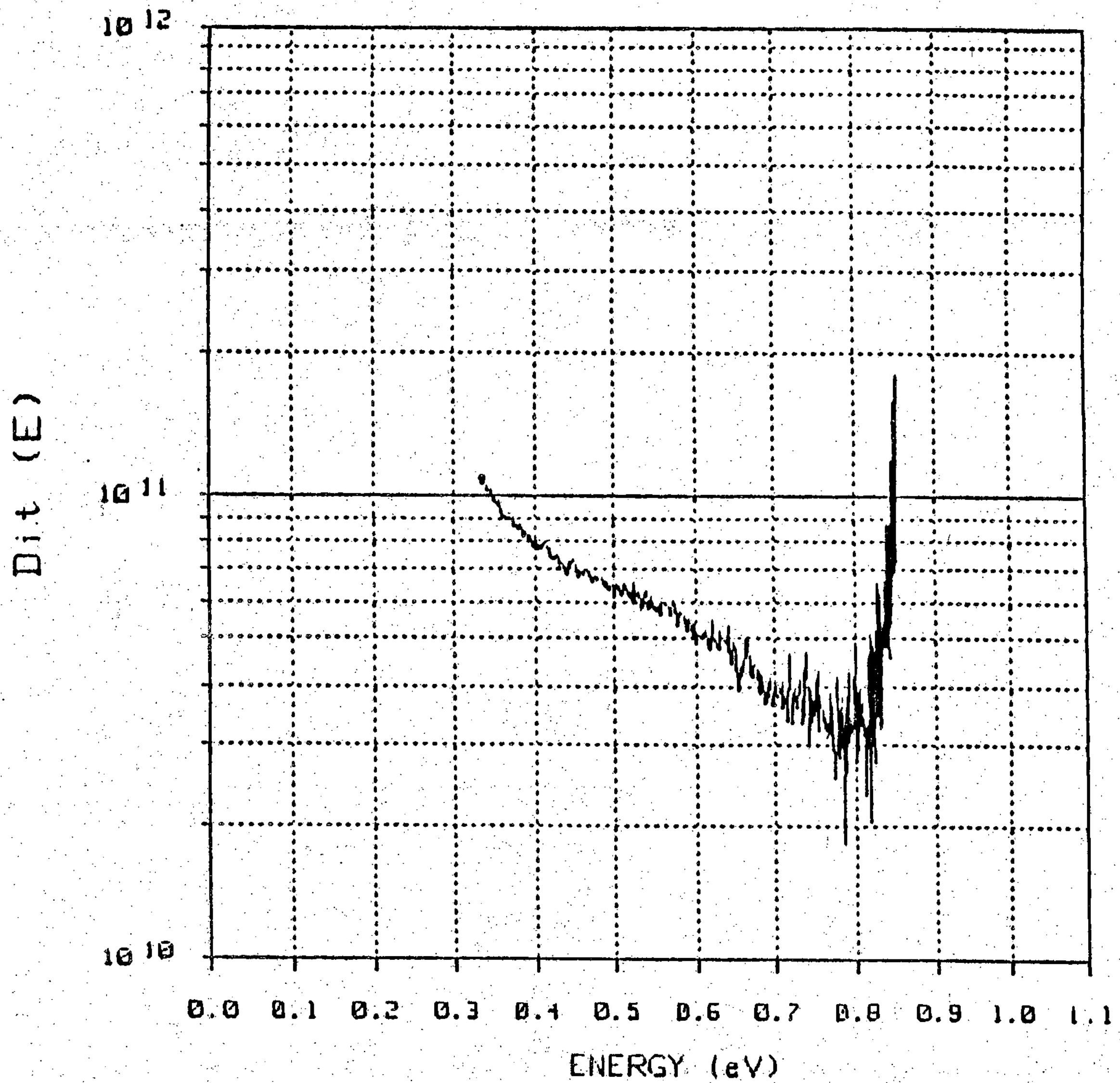

Figure 4.17 Surface states distribution at the Si-SiO_2 interface of a MOS capacitor, 33*-(3)

CHAPTER 5

A—Si:H TFT

In recent years, extensive studies had been made on hydrogenated amorphous silicon thin film transistors(TFTs), which are considered to be one of the promising switching devices for large-area liquid-crystal display panels[139]. The on/off current ratio as large as six orders of magnitude has already been achieved in a-Si:H TFTs[104]. Despite rapid progress in the TFT performance, the theoretical basis to determine static- and dynamic-characteristics of TFTs has not yet been settled mainly, because the influence of the gap states on TFT operation is very complicated. Neudeck and Malhotro[1] derived a simple theory to obtain TFT characteristics in the case of uniformly distributed gap states. Recently, Tohru Suzuki et al[140] reported the theoretical expressions of drain current as functions of gate bias and drain voltage. The TFT characteristics computed for various cases of gap state density distributions revealed the presence of a clear correlation between the TFT performance and the gap state density distribution. Satoru Kishida et al[141] presented a simple equation on the characterahistics of an a-Si TFT

with realistic semiconductor film thickness and having an exponential or uniform gap state density distribution.

5.1 General Analysis for Characteristics of A-Si:H TFT

5.1.1 General Expression for Drain Current

Figure 5.1 illustrates the stracture of the a-Si:H TFT studied in this research. The electrostatic petential in the surface space charge layer at the point (x,y) is expressed as $V(x,y)=V_o(y)+u(x,y)$. Here, $V_o(y)$ is the potential at the edge of the space charge layer, where $\partial u/\partial x=0$ is satisfied, and u(x,y) refers to the surface band bending. The sign of u(x,y) is positive for $V_G-u_{bi}>V_o(y)$ (V_G is the gate bias and u_{bi} is the build-in potential) and negative for $V_G-u_{bi}<V_o(y)$.

For simpliest, we derive the formula for an enhancement TFT, i.e. only consider the electron conductance and neglect the hopping conductance. The conductance for an element of the channel length dy and the width W is composed of the flat-band conductance $G_o(y+dy)$ and of the field-induced condutance $\Delta G(y+dy)$ arising from the band bending u(x,y). G_o (y+dy) and $\Delta G(y+dy)$ are written for electrons as

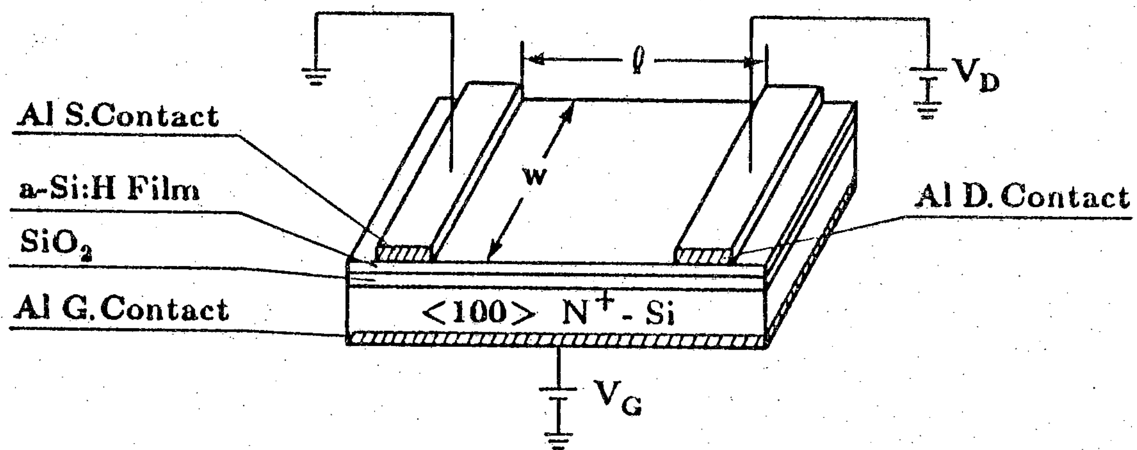

Figure 5.1 Schematic diagram of an a-Si:H TFT

$$G_o(y+dy)=\sigma_o\frac{Wd_a}{dy} \qquad (5.1.1)$$

and

$$\Delta G(y+dy)=\frac{W}{dy}\int_0^{d_a}\{\sigma_o\exp[eu(x,y)/kT]-\sigma_o\}dx$$

$$=\frac{\sigma_o W}{dy}\int_0^{eu^a(y)}\frac{\exp(eu/kT)-1}{\partial u/\partial x}\frac{d(eu)}{e} \qquad (5.1.2)$$

Here, σ_o is the flat-band conductivity of bulk a-Si:H and $u^a(y)$ is the surface potential at y, i. e., $u^a(y)=u(0,y)$. Then, the differential resistance of the element is given by

$$dR=[G_o(y+dy)+\Delta G(y+dy)]^{-1}$$

$$=\frac{dy}{\sigma_o W}\Bigg/\left[d_a+\int_0^{eu^a(y)}\frac{\exp(eu/kT)-1}{\partial u/\partial x}\frac{d(eu)}{e}\right] \qquad (5.1.3)$$

Since the potential difference cross the channel element $dV_o(y)$ for the drain current I_D is equal to $I_D dR$, the following equation holds:

$$I_D dy=\sigma_o W[d_a+\int_0^{eu^a(y)}\frac{\exp(eu/kT)-1}{\partial u/\partial x}\frac{d(eu)}{e}]dV_o(y) \qquad (5.1.4)$$

Integration of this equation over the channel from source($V_o(0)=0$) to drain($V_o(l)=V_D$ is the drain voltage) yields an expression for the drain current:

$$I_D=\frac{\sigma_o W}{l}\left[d_a V_D+\int_0^{V_D}\left(\int_0^{eu^a(y)}\frac{\exp(eu/kT)-1}{\partial u/\partial x}\frac{d(eu)}{e}\right)dV_o(y)\right] \qquad (5.1.5)$$

If both the electric field strength $\partial u(x,y)/\partial x$ and the surface potential $u^a(y)$ are obtained as a function of $V_o(y)$ for given values of V_G and V_D, the drain

current I_D can be calculated by eq.(5.1.5).

5.1.2 Determination of the Electric Field Strength $\partial u(x,y)/\partial x$

The surface band bending u(x,y) at the position(x,y) for a fixed value of y obeys the one dimensional Poisson's equation:

$$\frac{\partial^2 u(x,y)}{\partial x^2} = -\frac{\rho(x,y)}{\epsilon_o k_s} \tag{5.1.6}$$

Where, k_s is the dielectric constant of a-Si:H and $\rho(x,y)$ is the space-charge density due to the Fermi-level shift of qu(x,y). In general, the charge density is

$$\rho(x,y) = (-e)\int_{-\infty}^{\infty} N(E)[f(E-eV(x,y))-f(E)]dE \tag{5.1.7}$$

Where N(E) is the energy dependent density of states, and in its most general form implicitly includes all localized and extended states; f(E) is the Fermi-Dirac distribution function

$$f(E) = \left[1+\exp\left(\frac{E-E_F}{kT}\right)\right]^{-1} \tag{5.1.8}$$

Here, E_F is the Fermi-level. If both sides of eq.(5.1.6) are multiplied by 2 $\partial u/\partial x$ and integrated from x to the edge of the space-charge layer, where $\partial u/\partial x = 0$ is satisfied, then one obtains $\partial u(x,y)/\partial x$ for positive u(x,y) as

$$\left.\frac{\partial u}{\partial x}\right]_{x=x} = -\left[\frac{2}{\epsilon_o k_s}\int_0^{eu(x,y)} d(eu)\int_{-\infty}^{\infty} N(E)\{f(E-qu(x,y))-f(E)\}dE\right]^{\frac{1}{2}} \tag{5.1.9}$$

The denominator of eq.(5.1.5) $\partial u(x,y)/\partial x$ is therefore determined by eq.(5.1.8),

if the density distribution of gap states is given.

5.1.3 Determination of Surface Potential $u^a(y)$

The surface potential $u^a(y)$ is connected to the voltage drop across the insulating film $V_i(y)$, the built-in potential u_{bi} and the gate bias V_G by

$$V_G - u_{bi} = V_o(y) + V_i(y) + u^a(y) \tag{5.1.10}$$

The surface space-charge density $Q_a(y) = -C_i\ V_i(y)$(C_i=the insulator capacitance per unit area) is related to the surface electric field $\partial u(x,y)/\partial x]_{x=0}$ by Gauss' law $Q_a(y) = \epsilon_o k_s \partial u/\partial x]_{x=0}$, so that eq.(5.1.10) is rewritten as

$$V_G - V_o(y) - u_{bi} - u^a(y)$$

$$= \frac{1}{C_i}[2\epsilon_o k_s \int_0^{eu^a(y)} d(eu) \int_{-\infty}^{\infty} N(E)\{f(E-eu(x,y)) - f(E)\} dE]^{\frac{1}{2}} \tag{5.1.11}$$

This indicates that the surface potential $u^a(y)$ can be uniquely determined as a function of $V_o(y)$, if the gap state density distribution and gate bias are given.

By the use of eqs.(5.1.9) and (5.1.11), the theoretial drain current I_D is expressed by eq.(5.1.5) and can be calculated as a function of drain voltage.

5.1.4. Localized State Density Distribution N(E)

It is necessary to know the density of electronic states, N(E), of an amorphous semiconductor in order to understand and implove its electronic properties. This has become especially topical with the recent development of amorphous solar cells, diodes, switching devices and transistors. In crystalline semiconductors the density of states in the band gap is zero except for the presence of discrete energy levels. In constract, it is commenly believed that there is a continuous distribution of electronic states in the mobility gap of tetrahedrally coordinated amorphous semiconductors. Because of this difference, many techniques which can be used to determine N(E) for a crystal are not readily applicable to amorphous materials.

Recent years, the widely used experimental techniques for determining N(E) are field-effect measurement and capacitance-voltage measurement. Using the measurement data of the localized state density distribution N(E), we can get the I_D vs V_D for valuer of V_g according to eq.(5.1.5) by using numerical analysis techniques.

For analytical calculations an analytical formula of localized state density distribution N(E) is necessary. There are several models in literature. Listed are some as following:

(1) Neudeck and Malhotra[1] submited a model, that was

$$N(E)=N_t \quad E<E_A \tag{5.1.12}$$

$$N(E)=N_t \exp[m(E(X)-E_A)] \quad E\geq E_A \tag{5.1.13}$$

Where m controls the rate at which the states increase and N_t is the density of localized states at the Fermi energy.

(2) Tohru Suzuki et al.[140] proposed a function for localized state density distribution

$$N(E)=10^{16}\left\{A+B\left[\exp\left(\frac{E-E_c+0.6}{0.05}\right)+\exp\left(-\frac{E-E_c+1.0}{0.05}\right)\right]\right.$$

$$\left.+C\left[\exp\left(\frac{E-E_c+0.5}{0.025}\right)+\exp\left(-\frac{E-E_c+1.1}{0.025}\right)\right]\right\} \qquad (5.1.14)$$

Here, A, B, and C are curve fitting paramters and the N(E) curve has a minimum density of states at E_c -0.8eV. Three kinds of results are: (a) A=B=C=1 reproduces a measurement result; (b) A=10, B=C=1 refers to the case with a high density of states near midgap; (c) A=B=1, C=0 corresponds to the case with a low density of states near the band edges.

(3) Satoru Kishida et al.[141] assumed adensity distribution of localized state as

$$N(E)=N_G\exp\frac{E-E_c}{kT_G} \qquad (5.1.15)$$

Where N_G is the localized state density just under the conduction band edge and T_G is the characteristic temperature.

5.2 Approximate Analysis for Characteristics of A-Si:H TFT

The theoretial analysis of the a-Si:H TFT characteristics has been derived in the previous section. But these implicit explessions need to use cumbersome numerical calculation to be solved. For designing of devices and circuits, a simple less accurate theory which can intuitively grasp the physical phenomena and I—V characterics is very important.

5.2.1 Simple Theory

According to Tickle[142] the I_D— V_D characteristic of a TFT can be obtained from Equation (5.2.1). The potential, V, is the voltage between the gate and the conducting channel

$$I_D=\frac{W}{L}\int_{V_G-V_D}^{V_G} g(V)dV \tag{5.2.1}$$

The width of the channel is W, while L is its length. The voltage V_G and V_D are the gate and the drain voltage respectively.

Neudeck and Malhotra[1] derived the sheet conductivety of the channel, g(v), as a function of the gate voltage V_G. The rather complex expression obtained was shown to be approximated by Equation (5.2.2)

$$g(V)\simeq b^{aV} \tag{5.2.2}$$

Here a is a function of the slope of the straight-line portion of logg(V) vs V_G plot, while b is an arbitrary constant that will depend upon the carrier mobility, temperature, and geometrical factors of the device. By substituting into Equation (5.2.2) into Equation (5.2.1), the drain current was calculated as

$$I_D = B\left[e^{aV_G}(1-e^{-aV_D})\right] \quad (5.2.3)$$

Were B is a constant equal to Wb/La. This formula is only appropriate for the region where logg(V) vs V_G is a straight line and the "inhanced" channel is not pinched off. The calculated curve was consistent with the experimental data in the region of larger gate voltages and where the channel is not "pinched-off".

TO expand region, where Equation (5.2.3) can be used a new expression for g(V) that would be applicable at lower gate voltages is given by Equation (5.2.4) [143]

$$g(V) = b(e^{aV} + c) \quad (5.2.4)$$

The constant c is related to the construction and depends on the density of the localized states in the bandgap of the a-Si. As these states near the Fermi energy are smaller, a will become larger and c gets smaller. By adding the constant c, Equation (5.2.4) will more nearly approximate the g(V) of practical devices at low gate voltages. Substituting Equation (5.2.4) into Equation (5.2.2), we get

$$I_D = B[e^{aV_G}(1-e^{-aV_D}) + acV_{D]} \quad (5.2.5)$$

5.2.2 An Approximative Theoretical Analysis

[A] Uniform Localized State Density Distribution Case

In this approximative analysis, the following is assumed: (1) Approximation of zero temperature statistics; (2) Uniform localized state density distribution; (3) For a-Si, the density of electrons trapped in localized states is much larger than the excess density of free carriers(electrons or holes). We have for the charge density:

$$\rho(x,y)=-e\int_0^{eu} N_T d(eu)=-e^2 N_T u \tag{5.2.6}$$

Substituting it into eq. (5.1.6) yields:

$$\frac{\partial^2 u(x,y)}{\partial x^2}=\frac{e^2}{\epsilon_o K_s} N_T u(x,y) \tag{5.2.7}$$

This equation is easily solved for u(x,y) and shows the band bendind to be exponential

$$u(x,y)=u(0,y)\exp(-Lx) \tag{5.2.8}$$

Where u(0,y) is the surface potential.

Substituting eq.(5.2.6) into eq.(5.1.9) yields

$$\left.\frac{\partial u}{\partial x}\right]_{x=x}=\pm\left[\frac{2}{\epsilon_o K_s}\int_0^{eu} e N_T u\, d(eu)\right]^{\frac{1}{2}}=\pm\left[\frac{2}{\epsilon_o K_s} N_T \frac{e^2 u^2}{2}\right]^{\frac{1}{2}}$$

$$=\pm\left[\frac{N_T e^2}{\epsilon_o K_s}\right]^{\frac{1}{2}} u=\pm L u \tag{5.2.9}$$

Where L is

$$L=\left[\frac{N_T e^2}{\epsilon_o K_s}\right]^{\frac{1}{2}} \tag{5.2.10}$$

Substituting eq.(5.2.6) into eq.(5.1.11) yields

$$V_G - V_o(y) - u_{bi} - u^a(y) = \frac{1}{C_i}\left[\epsilon_o K_s \int_0^{eu^a(y)} N_T eud(eu)\right]^{\frac{1}{2}}$$

$$u^a(y)=\frac{V_G - V_o(y) - u_{bi}}{\frac{e}{C_i}(\epsilon_o K_s N_T)^{\frac{1}{2}}+1} \tag{5.2.11}$$

Under larger V_G, eq.(5.2.11) can be approximated by

$$u^a(y)=\left[\frac{\epsilon_o k_{ox}^2}{e^2 d_{ox}{}^2 K_s N_T}\right]^{\frac{1}{2}}(V_G - V_o(y)) \tag{5.2.12}$$

Substituting eq.(5.2.9) into eq.(5.2.5) yields (5.2.13)

$$I_D=\frac{\sigma_o W}{l}\left[d_a V_D + \int_0^{V_D}\left(\int_0^{eu^a(y)} \frac{\exp(eu/kT)-1}{Lu}\frac{d(eu)}{e}\right)dV_o(y)\right] \tag{5.2.13}$$

In eq.(5.2.13), the pre-exponential factor 1/eu changes gradually compared with exponential factor exp(eu/kT). Thus we can take the 1/eu term out of the integrand, and ignor the "1". Eq.(5.2.12) can then be approximated as

$$I_D \simeq \frac{\sigma o W}{l}\left[d_a V_D + \frac{kT}{Leu}\int_0^{V_D}\left[\exp\frac{eu^a(y)}{kT}-1\right]dV_o(y)\right] \tag{5.2.14}$$

Substituting eq.(5.2.12) into eq.(5.2.14) yields

$$I_D \simeq \frac{\sigma o W}{l}\left\{ d_a V_D + \frac{k^2T^2}{Le^2u}\exp\left[\left(\frac{\epsilon_o k_{ox}{}^2}{k^2T^2d_{ox}{}^2K_sN_T}\right)^{\frac{1}{2}} V_G \right] \right.$$

$$\left. \left[1-\exp\left(\frac{\epsilon_o k_{ox}{}^2}{k^2T^2d_{ox}{}^2K_sN_T}\right)^{\frac{1}{2}}(-V_D) \right] \right\} \qquad (5.2.15)$$

Let

$$a = \frac{\epsilon_o K_{ox}{}^2}{k^2T^2d_{ox}{}^2K_sN_T} = \frac{e}{kT}\frac{K_{ox}}{K_s}\frac{1}{d_{ox}L} \qquad (5.2.16)$$

$$B = \sigma_o \frac{W}{l}\frac{k^2T^2d_{ox}K_s}{e^2uK_{ox}} = \frac{\epsilon_o W}{l}\frac{kT}{euaL} \qquad (5.2.17)$$

$$c = \frac{euLd_a}{kT} \qquad (5.2.18)$$

We get

$$I_D = B[\exp(aV_G)(1-\exp(-aV_D)) + acV_D] \qquad (5.2.19)$$

[B] Exponential Localized-State-Density Distribution Case

Let us assume that the localized state density N(E) in the semiconductor falls exponentially with respect to energy E from the conduction band edge to the midgap as

$$N(E) = N_G \exp\frac{E-E_c}{kT_G} \qquad (5.1.20)$$

Where N_G is the localized state density just under the conduction band edge

and T_G is the characteristic temperature.

(1) $T_G >> T$

When T_G is much higher than the ambient temperature T, the zero kelvin approximation of Fermi-Dirac distribution function is satisfied. This is because the function decrease rapidly to zero with the increase of E from $E=E_F$ and because it approaches rapidly to 1 with the decrease of E from $E=E_F$.

From eq.(5.1.7), the charge density is

$$\rho(x,y)=(-e)\int_{E_F}^{E_F+eu} N(E)dE \tag{5.2.21}$$

Substituting eq.(5.2.20) into eq.(5.2.21), get

$$\rho(x,y)=(-e)\int_{E_F}^{E_F+eu} N_G \exp\frac{E-E_c}{kT_G}dE$$

$$=-eN_G kT_G \exp\frac{E_F-E_c}{kT_G}\left(\exp\frac{eu}{kT_G}-1\right) \tag{5.2.22}$$

From eq.(5.1.9), we obtain

$$\left.\frac{\partial u}{\partial x}\right]_{x=x}=-\left[\frac{2}{\epsilon_o K_s}\int_0^{eu(x,y)} N_G kT_G \exp\frac{E_F-E_c}{kT_G}\left(\exp\frac{eu}{kT_G}-1\right)d(eu)\right]^{\frac{1}{2}}$$

$$=-\left[\frac{2}{\epsilon_o k_s}N_G k^2 T_G^2 \exp\frac{E_F-E_c}{kT_G}\left(\exp\frac{eu}{kT_G}-\frac{eu}{kT_G}-1\right)\right]^{\frac{1}{2}} \tag{5.2.23}$$

when the gate voltage V_G is sufficiently large,

$$eu^a(y) >> kT_G$$

is satisfied. Eq.(5.2.23) can be approximated by

$$\left.\frac{\partial u}{\partial x}\right]_{x=x} = \pm\left[\frac{2N_G}{\epsilon_o k}\right]^{\frac{1}{2}} kT_G \exp\frac{E_F-E_c}{2kT_G}\exp\frac{eu}{2kT_G} \tag{5.2.24}$$

Eq.(5.1.11) can be approximated by

$$V_G-V_{bi}-V_o(y)=\frac{1}{C_i}\left[2\epsilon_o k_s N_G k^2 T_G^2 \exp\frac{E_F-E_c}{kT_G}\exp\frac{eu^a}{kT_G}\right]^{\frac{1}{2}}$$

$$=\left[\frac{2K_s d_{ox}^2 N_G k^2 T_G^2}{\epsilon_o k_{ox}^2}\right]^{\frac{1}{2}}\exp\frac{E_F-E_c}{2kT_G}\exp\frac{eu^a}{2kT_G} \tag{5.2.25}$$

Now solve eq.(5.2.25) for u^a.

$$\exp\frac{eu^a}{2kT_G}=\left[\left(\frac{\epsilon_o k_{ox}^2}{2k_s d_{ox}^2 N_G k^2 T_G^2}\right)^{\frac{1}{2}}\exp\frac{E_F-E_c}{2kT_G}\right](V_G-u_{bi}-V_o(y)) \tag{5.2.26}$$

From eq.(5.1.5), we have

$$I_D=\frac{\sigma_o W}{l}\left[d_a V_D \pm \int_0^{V_D}\left\{\int_0^{eu^a(y)}\left[\left(\frac{\epsilon_o K_s}{2e^2 N_G}\right)^{\frac{1}{2}}\left(\frac{1}{kT_G}\right)\exp\frac{E_c-E_F}{2kT_G}\right]\exp\left[\frac{eu}{2kT}\left(\frac{2T_G-T}{T}\right)\right]deu\right\}dV_o(y)\right]$$

$$=\frac{\sigma_o W}{l}\left[d_a V_D \pm \int_0^{V_D}\left(\frac{\epsilon_o K_s}{2eN_G}\right)^{\frac{1}{2}}\left(\frac{2T}{2T_G-1}\right)\exp\frac{E_c-E_F}{2kT_G}\right.$$

$$\left.\exp\left[\left(\frac{eu^a}{2kT_G}\right)\left(\frac{2T_G-1}{T}\right)\right]dV_o(y)\right] \tag{5.2.27}$$

Substituting eq.(5.2.26) into eq.(5.2.27) yields

$$I_D=\frac{\sigma_o W}{l}\left\{d_a V_D \pm \left[\frac{\epsilon_o k_s}{2eN_G}\right]^{\frac{1}{2}}\left[\frac{2T}{2T_G-1}\right]\left[\frac{\epsilon_o k_{ox}^2}{2K_s d_{ox}^2 N_G k^2 T_G^2}\right]^{\left(\frac{T_G}{T}-\frac{1}{2}\right)} \exp\left[\frac{E_c-E_F}{2kT_G}\right]^{\frac{2T_G}{T}}\right.$$

$$\left.\int_0^{V_D}[V_G-u_{bi}-V_o(y)]^{\frac{2T_G-T}{T}}\,dV_o(y)\right\} \qquad (5.2.28)$$

We define a device constant K_1 as

$$K_1=\left(\frac{2T}{2T_G-1}\right)\left(\frac{\epsilon_o K_s}{2eN_G}\right)^{\frac{1}{2}}\left[\frac{\epsilon_o K_{ox}^2}{2K_s d_{ox}^2 N_G K^2 T_G^2}\right]^{\left(\frac{T_G}{T}-\frac{1}{2}\right)}$$

$$\exp\left[\frac{E_c-E_F}{2KT_G}\right]^{\frac{2T_G}{T}} \qquad (5.2.29)$$

and obtain

$$I_D=\frac{\sigma_o W}{l}\left[d_a V_D \pm K_1\int_0^{V_D}[V_G-u_{bi}-V_o(y)]^{\frac{2T_G-T}{T}}\,dV_o(y)\right] \qquad (5.2.30)$$

Integrating eq.(5.2.30) yields

$$I_D=\frac{\sigma_o W}{l}\left[d_a V_D+\frac{T}{2T_G}K_1\left((V_G-u_{bi})^{\frac{2T_G}{T}}-(V_G-u_{bi}-V_D)^{\frac{2T_G}{T}}\right)\right] \qquad (5.2.31)$$

Especially in the case that $V_D \simeq 0$, I_D is given by

$$I_D=\frac{\sigma_o W}{l}\left[d_a V_D+K_1(V_G-u_{bi})^{\frac{2T_G}{T}-1}V_D\right] \qquad (5.2.32)$$

In the V_G-u_{bi}-$V_D<0$ case, i.e. the saturated condition, the same as in the MOS FET case, we have

$$I_D = \frac{\sigma_o W}{l}\left[d_a V_D + \frac{T}{2T_G} K_1 (V_G - u_{bi})^{\frac{2T_G}{T}}\right] \quad (5.2.33)$$

It is worth noting that the on-off transition is expressed not by $I_D \propto \exp(aV_G)$ like the weak inversion case of a MOS FET, but by $\log I_D \propto \log(V_G - u_{bi})$.

(2) $T_G < T$

When T_G is lower than T, the localized state density increases more rapidly with energy then the Fermi-Dirac distribution function decreases. Therefore, the zero kelvin approximation of Fermi-Dirac distribution function becomes invalid. since the number of electrons trapped by the localized states above E_F is larger than below E_F, from eq.(5.1.7), the charge density is

$$\rho(x,y) = -e \int_{-\infty}^{E_c - eu} N(E+eu)\exp\left(\frac{E_F - E}{kT}\right)dE$$

$$= -e \int_{-\infty}^{E_c - eu} N_G \exp\left(\frac{E - E_c + eu}{kT_G}\right)\exp\left(\frac{E_F - E}{kT}\right)dE$$

$$= eN_G\left[\frac{1}{kT} - \frac{1}{kT_G}\right]^{-1}\exp\left(\frac{E_F - E_c + eu}{kT}\right) \quad (5.2.34)$$

Substituting eq.(5.2.34) into eq.(5.1.9), we obtain

$$\left.\frac{\partial u}{\partial x}\right]_{x=x} = \pm\left[\frac{2}{\epsilon_o K_s} N_G kT\left(\frac{1}{kT} - \frac{1}{kT_G}\right)^{-1}\exp\left(\frac{E_F - E_c}{kT}\right)\left(\exp\frac{eu}{kT} - 1\right)\right]^{\frac{1}{2}} \quad (5.2.35)$$

$$\left.\frac{\partial u}{\partial x}\right]_{x=x} \simeq \pm\left[\frac{2}{\epsilon_o K_s} N_G K^2 T^2 T_G \frac{1}{T_G - T}\exp\left(\frac{E_F - E_c + eu}{kT}\right)\right]^{\frac{1}{2}} \quad (5.2.36)$$

Eq.(5.1.11) can be approximated by

$$V_G-u_{bi}-V_o(y)=\frac{1}{C_i}\left\{2\epsilon_o k_s N_G k^2T^2T_G\frac{1}{T_G-T}\exp\left(\frac{E_F-E_c+eu^a}{kT}\right)\right\}$$

and we obtain

$$\exp\frac{eu^a}{2kT}=\left\{\frac{\epsilon_o K_{ox}}{d_{ox}}\left(\frac{T_G-T}{2\epsilon_o K_s N_G k^2T^2T_G}\right)^{\frac{1}{2}}\exp\left(\frac{E_F-E_c}{2kT}\right)\right\}$$

$$[V_G-u_{bi}-V_o(y)] \tag{5.2.37}$$

Substituting eq.(5.2.36) into eq.(5.1.5) yields

$$I_D=\frac{\sigma_o W}{l}\left\{d_a V_D\pm\int_0^{V_D}\left[\frac{2\epsilon_o K_s(T_G-T)}{N_G T_G}\right]^{\frac{1}{2}}\right.$$

$$\left.\exp[\frac{E_c-E_F}{2kT}]\left[\exp\frac{eu^a(y)}{2kT}-1\right]dV_o(y)\right\} \tag{5.2.38}$$

Substituting eq.(5.2.37) into eq.(5.2.38) results in

$$I_D=\frac{\sigma_o W}{l}d_a V_D+K\frac{1}{2}[(V_G-u_{bi})^2-(u_G-u_{bi}V_D^2)] \tag{5.2.39}$$

Where K is defined as

$$K=\frac{\epsilon_o k_s}{d_{ox}N_G kT}\left[1-\frac{T}{T_G}\right]\exp\left[\frac{E_c-E_F}{kT}\right] \tag{5.2.40}$$

In the case where $V_D \simeq 0$,

$$I_D=\frac{\sigma_o W}{l}[d_a V_D+K(V_G-u_{bi})V_D] \tag{5.2.41}$$

In the case of a saturated device, $V_D>(V_G-u_{bi})$

$$I_D = \frac{\sigma_o W}{l}[d_a V_D + \frac{1}{2}K(V_G - u_{bi})^2] \tag{5.2.42}$$

The square root of I_D depends linearly on V_G and slightly depends on T_G and T. This feature is similar to that of a MOS FET in strong inversion. However the physical origins are quite different.

5.3 Experiment Results

Figure 5.2 [1] illustrates the drain current I_D vs drain voltage V_D for various values of gate voltage V_G. these data were obtained for a TFT made from a 560 Å thick amorphous silicon film deposited at 3.2 Å/sec onto the 3000Å thick SiO_2 substrate followed by a 400°C anneal for 4 hours. Note that the drain characteristics I_D vs V_D for a fixed value of V_G appear quite similar to an ordinary MOS FET. As the drain voltage, V_D, is increased I_D increases but begins to saturate at large values of V_D, indicating a channel pinch-off type condition. At these larger values of V_G and V_D there appears to be a channel shortening phenomenon or a leakage component giving the beyond pinch-off regin a slight slope to the "straight line" part of the plot.

Figure 5.3 shows the experimental plot of I_D vs V_G for a fixed value of V_D. For this device the "a" of eq.(5.2.3) obtained from the slop of Figure 5.3 is 0.1018 by at least squares fit to the experimental data points. The arbitray constant "B" was obtained from one point on Figure 5.2, by using

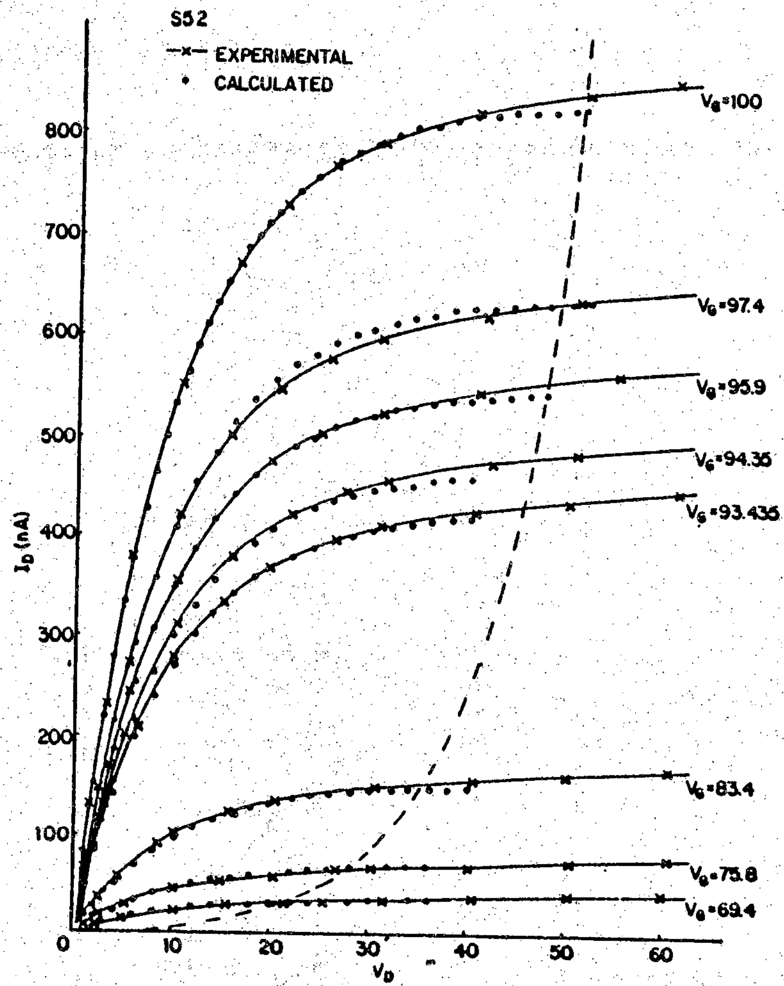

Figure 5.2 Experimental and calculated drain characteristics for an a-Si TFT (from Reference 1)

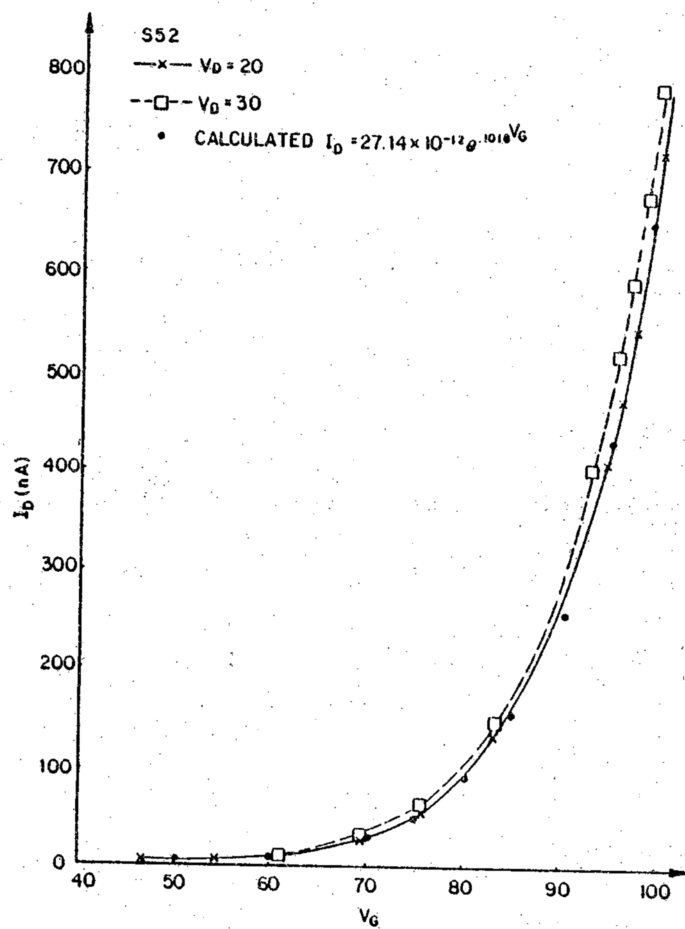

Figure 5.3 The drain current vs gate voltage for fixed values of V_D (from Reference 1)

$$I_D=31.2x10^{-12}e^{0.1018V_G}[1-e^{-0.1018V_D}] \quad (5.3.1)$$

The dots of Figure 5.2 were calculated from eq.(5.3.1). This derivation is based on below pinch-off operation and that the exponential relationship is valid. hence, for gate voltages less than 50V eq.(5.2.3) becomes invalid. Figure 5.4 illustrated a similar plot of the experimental and calculated data for gate voltage to as low as 54.6V and with an expanded scale near the origin.

The approximate expression of eq.(5.2.5) was verified by the following experimental results. Figure 5.5 illustrates the experimental plot of I_D vs V_G for a fixed value of V_D=1.5 volts for both positive and negative gate voltages. The contants a, B, and c can be obtained from Figure 5.5, which for this device is a=0.085, B=$1x10^{-8}$ A and c=3. Therefore, the static characteristics are given by eq.(5.3.2)

$$I_D=1x10^{-8}[e^{0.085V_G}(1-e^{-0.085V_D})+0.604V_D] \quad (5.3.2)$$

Figure 5.6 compares the experimental data with eq.(5.3.2) between $V.FG_D$=10V and 100V. Figure 5.7 compares experimental data with eq.(5.3.2) between V_D=1V and 10V, while Figure 5.8 compares the experimental data with eq.(5.3.3).

$$I_D=1x10^{-8}[e^{0.085V_G}(1-e^{-0.085V_D})] \quad (5.3.3)$$

These results prove that eq.(5.2.5) is more accurate than eq.(5.2.3). Eq.(5.2.5) provides a better fit to the data than eq.(5.2.3) when V_G is smaller then the straight-line portion of Figure 5.5.

when $V_G<20V$, the I_D vs V_D dependence is changed to a linear plot. The experimental plot of I_D vs V_D for V_G=0, 10V and 20V is given in Figure 5.9. Only for gate voltages larger than 20v can the channel be formed. We can

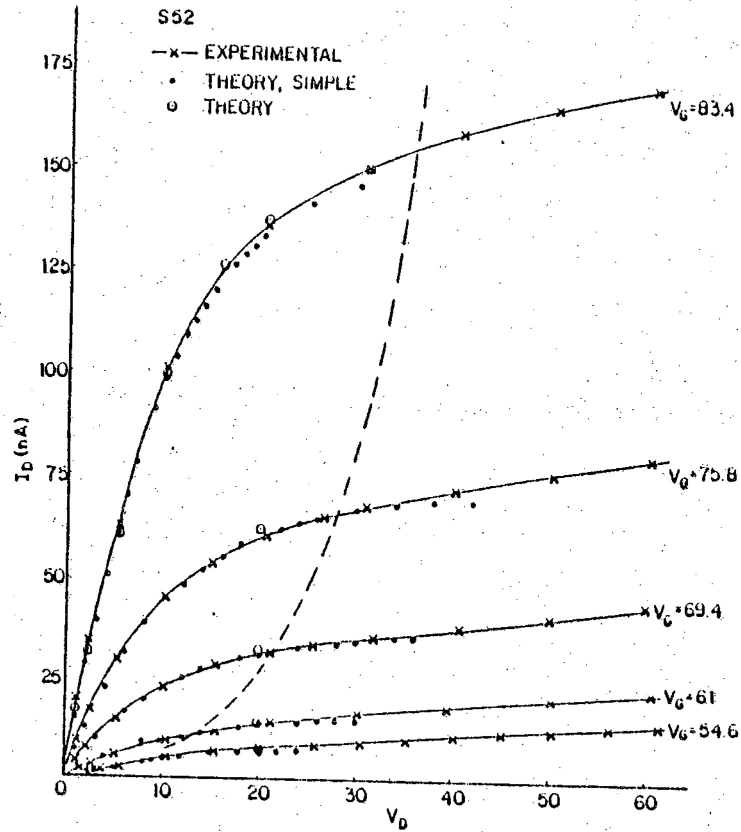

Figure 5.4 The drain characteristics for sample S52 (from Reference 1)

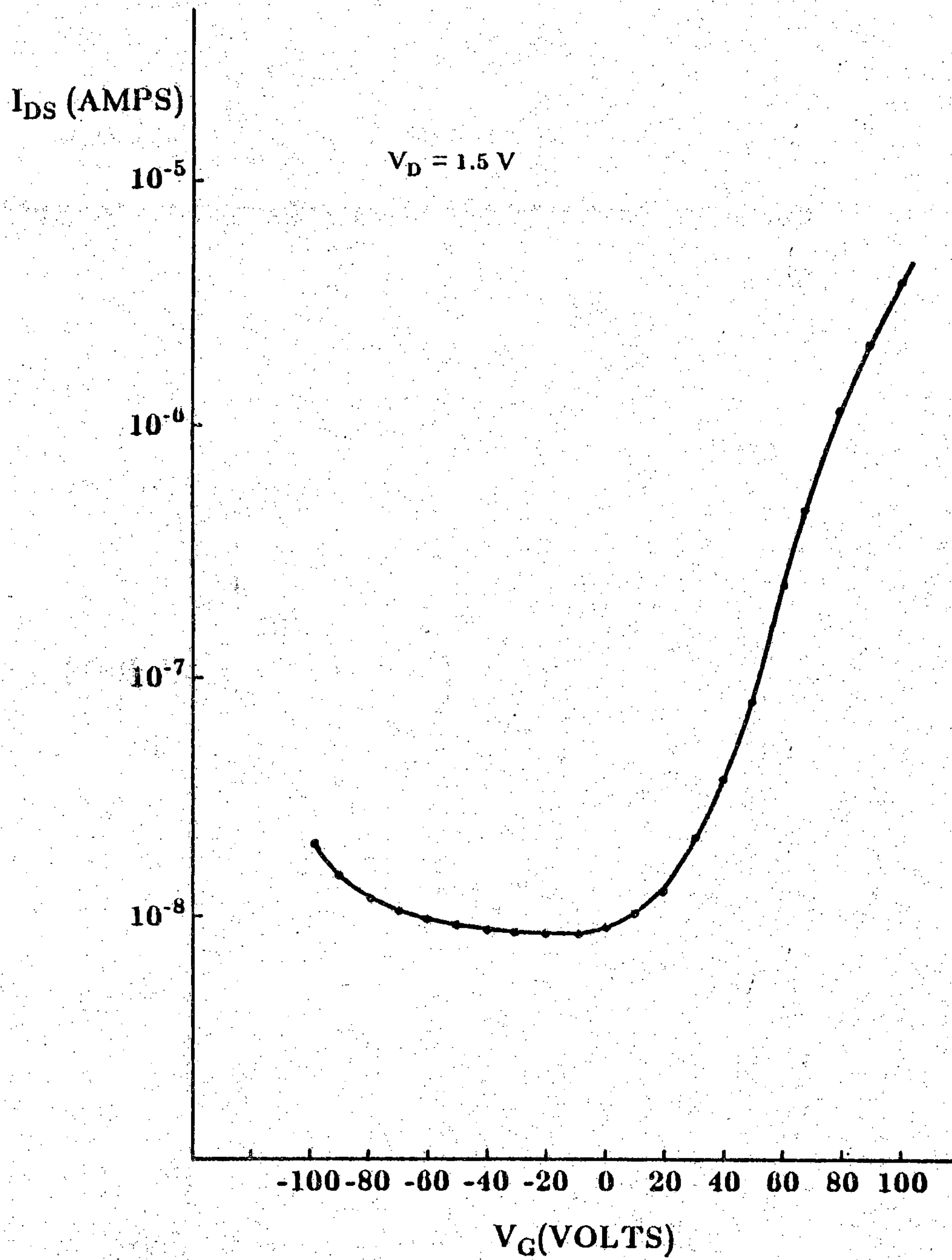

Figure 5.5 Experimental drain current vs gate voltage for sample 30*-(1)-[1], V_D=1.5V

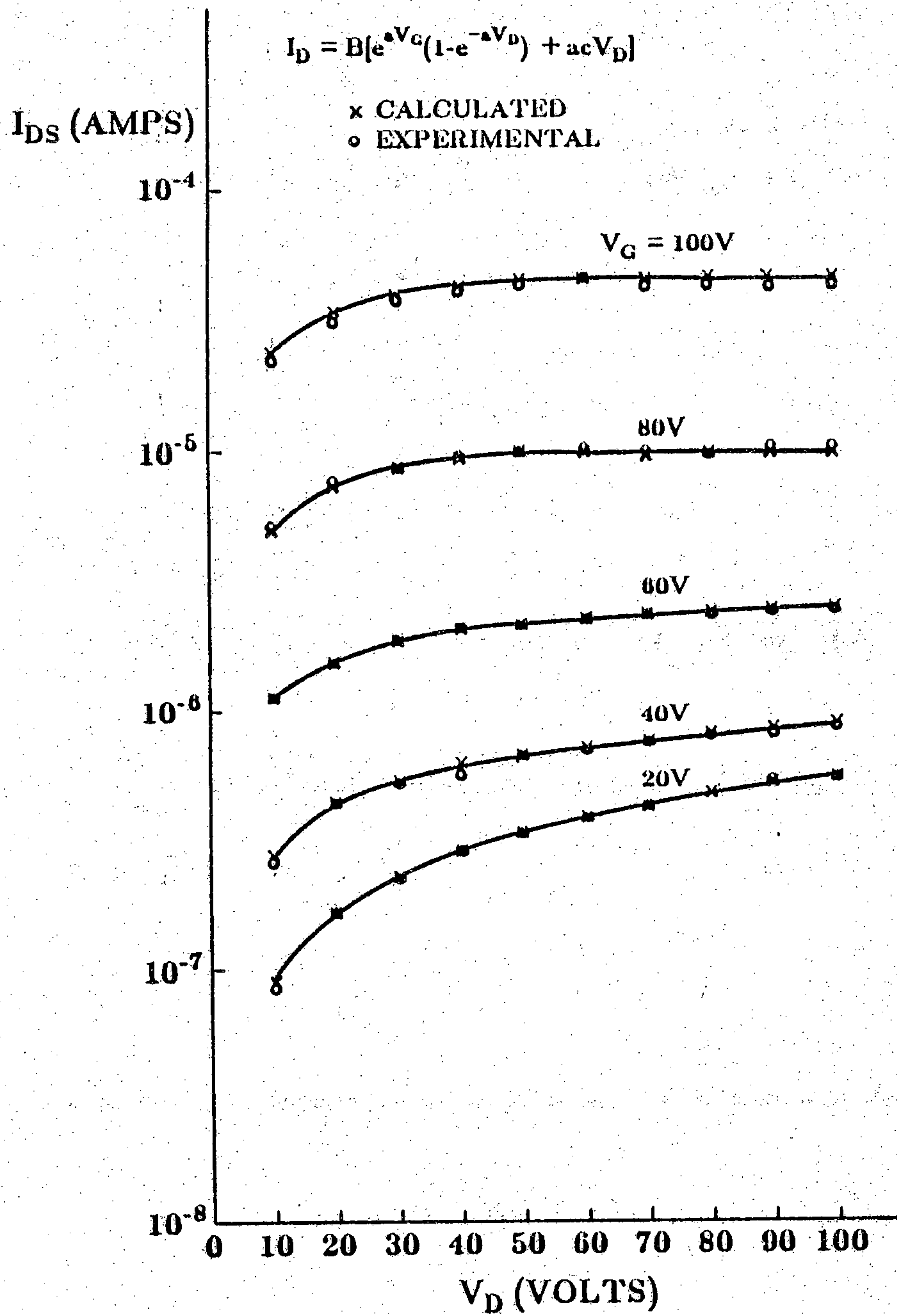

Figure 5.6 Experimental and calculated[eq.(5.3.2)] drain characteristics for sample 30*-(1)-[1], V_D=10 to 100V

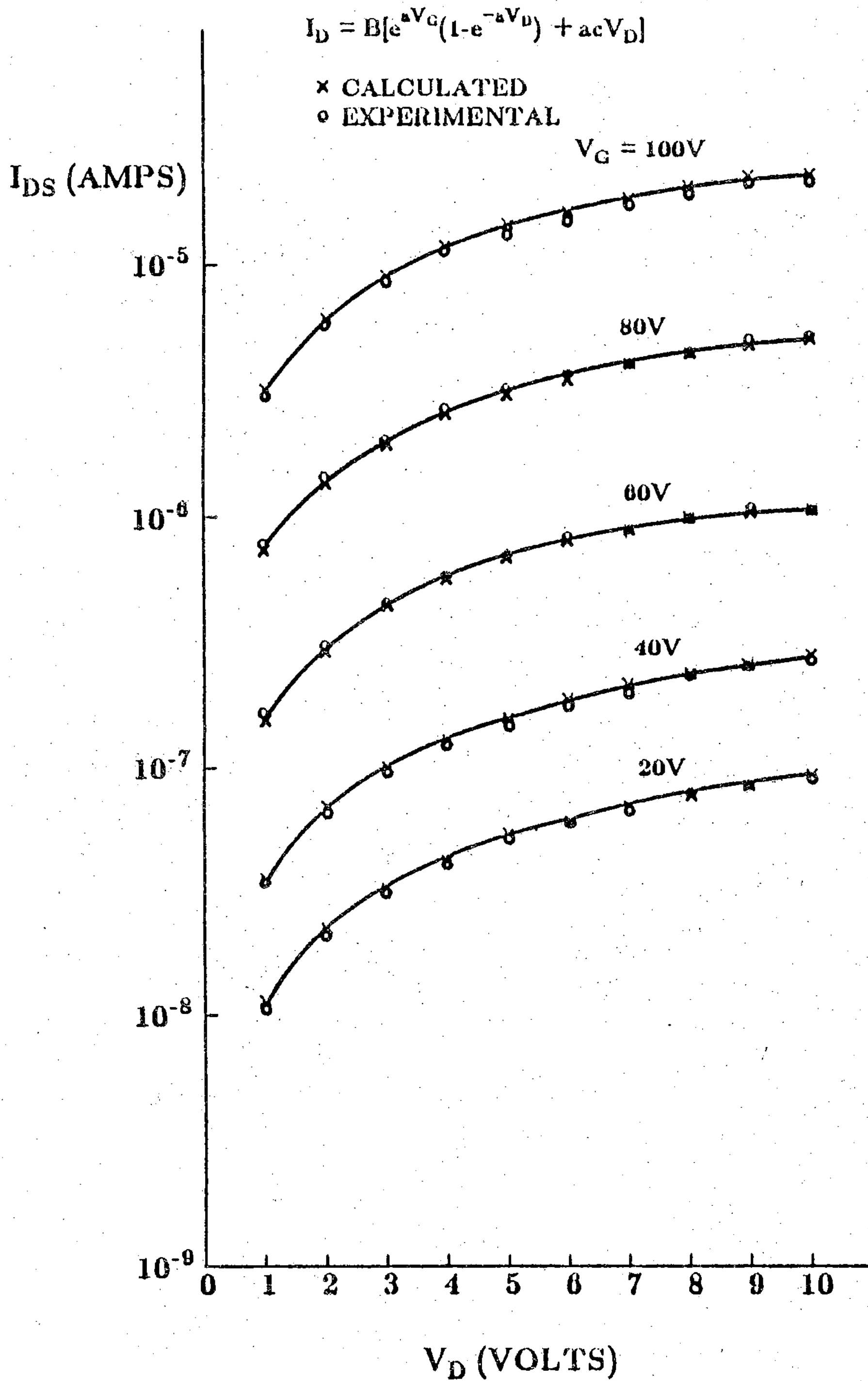

Figure 5.7 Experimental and calculated[eq.(5.3.2)] drain characteristics for sample 30*-(1)-[1], V_D=1 to 10V

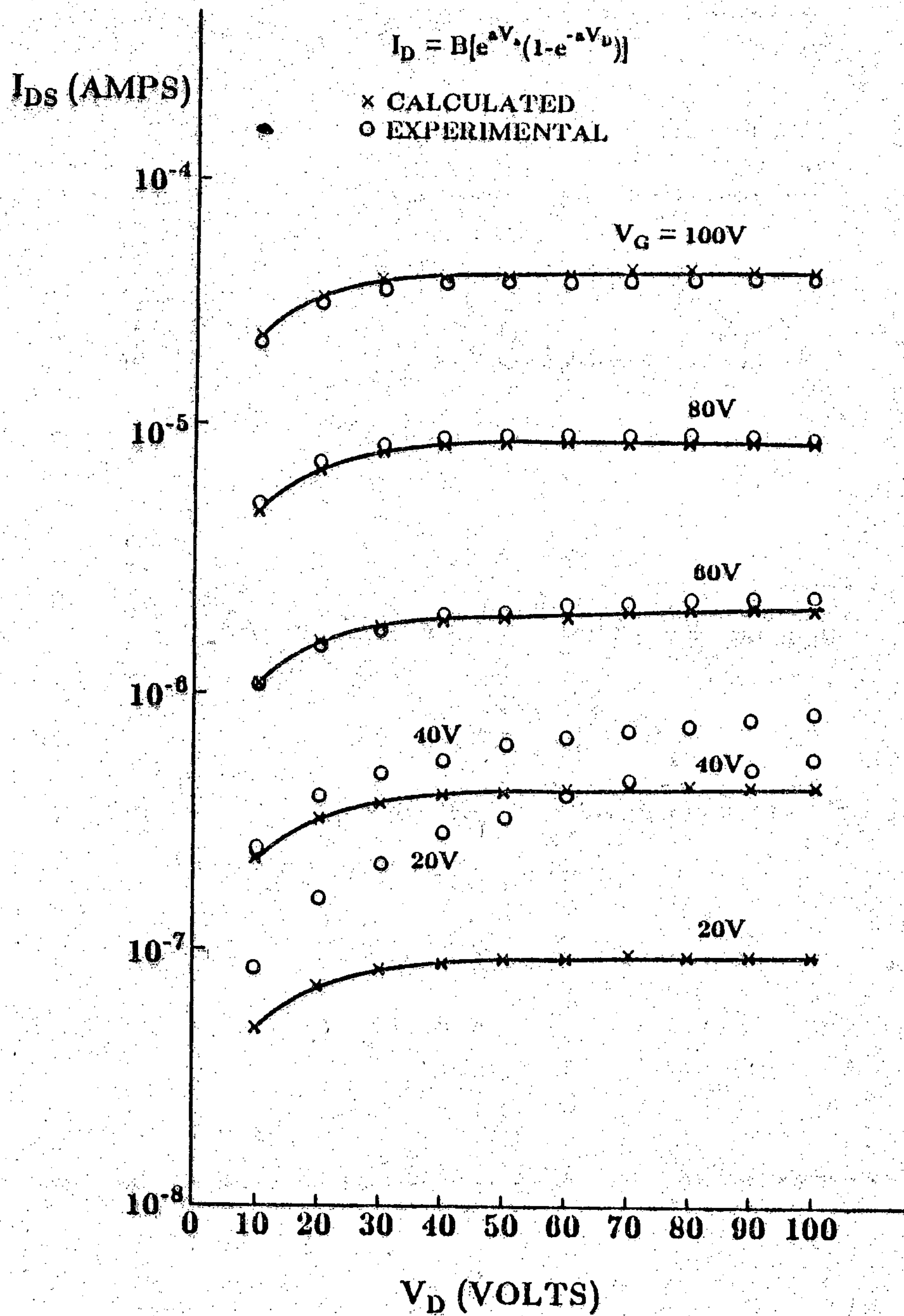

Figure 5.8 Experimental and calculated[eq.(5.3.3)] drain characteristics for sample 30°-(1)-[1], V_D=10 to 100V

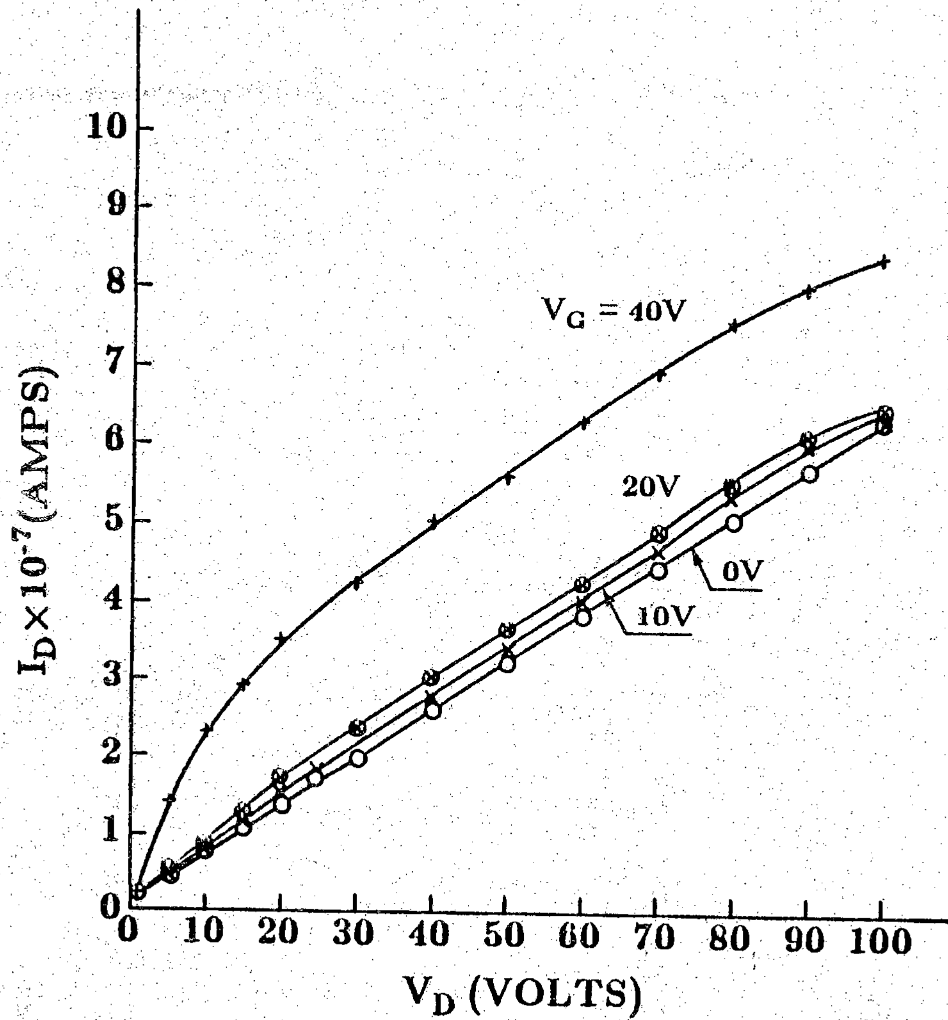

Figure 5.9 Experimental drain charateristics for sample 30*-(1)-[1], $V_G < V_{th}$

define a threshold voltage V_{th} for a-Si:H TFT. For $V_G<V_{th}$ the I_D vs V_D characteristic of a-Si:H TFT is linear. This is different from an IGFET which is in saturation. The channel of an a-Si:H TFT is formed slowly and never really is pinched-off. The I_D vs V_D characteristic of a-Si:H TFT is changed from linear ($V_G< V_{th}$) to saturation ($V_G>V_{th}$). This feature is controlled by the density of localized states and the stracture of a-Si:H TFT.

Curve A of Figure 5.10 shows the experimental results of voltage V_G versus drain current I_D characteristics[141]. In order to obtain reproducible results, a pulsed votage V_G was applied to the gate and the drain. Thus the FET operated in the saturated region. Clock frequency and the duty ratio of the pulse were 100 Hz and 50% respectively. The ambient temperature was 20°C. The TFT had 2300 Å and 2000 Å thick SiON and a-Si layers, respectively, both of which were deposited by the arc discharge decomposition method,and had a 50 μm long and 200 μm wide channel. It can be seen that $\log(I_D)$—$\log(V_G)$ data is approximated by a kinked line. For low values of V_G the slope of the approximate line was 5.2. This means that the localized state density far from the conduction band edge fall exponentially toward the midgap and that the characteristic temperature of the localized state density distribution is 762°K. For large V_G, the slope of the approximate line was about 2.4. This means that there are localized states of extremely high density near the conduction band edge and that the transition from the low density region near the midgap to the high density region near the band edge is very sharp.

The curve B of Figure 5.10, shows the experimental results of V_G vs I_D for a device which was made by electron beam evaporated a-Si and ion implanted with hydrogen. The structure of this device has been described in Section 3.1,

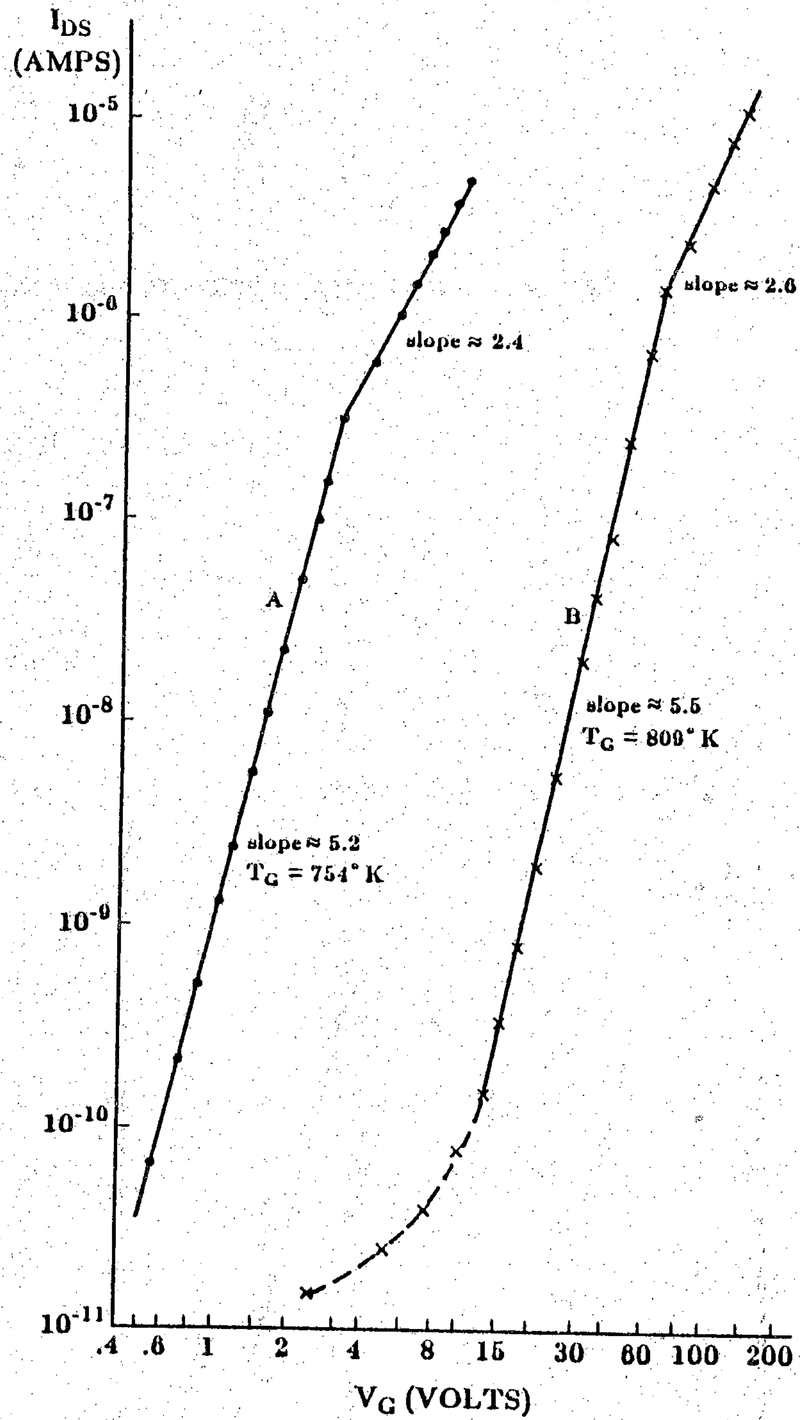

Figure 5.10 Drain current vs gate voltage for two samples: A, from Reference 141; B, for sample 30*-(2)-[3]

and the procedures of the measurements were been expressed in Section 3.2. Compared with curve A, the shape of curve B was nearly the same curve A, except in the low V_G area which was not a straight line. For medium values of V_G, the slope of the approximate line was 5.5. Therefore, the characteristic temperature of the LSDD is 806°K. For large V_G, the slope of the approximate line was 2.6.

5.4 Discussion of Results

Amorphous silicon field-effect-transistors has been found to have extremely high on-off current ratios and sharp on-off transitions. They are promising as non-linear devices for switching arrays in large area parel displays and image sensors. It is necessary to develop desige methodologies for devices and circuits. For this purpose, the relation between FET characteristics and the electrical properties of a-Si, i.e., the localized state density distribution, must be clarified during the early stages of development. An one-dimensional analyses of the FET characteristics was utilized in the field effect technique to charaxterize the localized state density distribution in a-Si[101]. The results of this work demonstrated the fact that N(E) conldn't be determined uniquely. Because of the Fermi factors in eq.(5.1.7), any structure finer than 2kT in the density of state cannot be resolved. Thus it is impossible to determine whether the density of states is a continuous distribution or whether it contains some narrow peaks.

The cumbersome numerical calculation for determining the localized state density distribution is not suitable or a design tool for devices and circuits. A coarse and simple theory which can express concisely the FET characteristics, is very important. The simple theory and experimental data can be used to abtain the localized state density distribution.

For high localized state density distribution, e.g. higher than 10^{19} /cm^3-ev, the uniform localized state density distribution may be used. Eq.(5.2.5) is a good aproximate formula for the a-Si TFT characteristic.

For lower localized state density distribution, e.g. lower than 10^{17} /cm^3-ev, the exponential localized state density distribution may be a suitable model. Figure 5.9 shows the experiment results. Glow- discharge a-Si:H TFT and an electron beam evaporated a-Si:H TFT all are good aproximation. The differences between the glow discharge a-Si:H TFT and the electron beam a-Si:H TFT are the insulater layer and the measurement conditions. In section 5.3, we have expressed the measurement condition and the insulater layer for a glow discharge a-Si:H TFT. The electron beam a-Si:H TFT is different. The insulator is SiO_2 and the thickness of SiO_2 is 3000 Å. The measurement conditions are a DC voltage instead of pulsed voltages. Furthermore, every point was measured 5 minutes after the operating voltage was applied.

In conclusion, if the density of localized states near Femi level is large, the density of localized states model can be uniform. If the density of localized states near Femi level is much lower, the model should be exponential.

CHAPTER 6

CONCLUSIONS AND RECOMMENDATIONS FOR FUTURE RESEARCH

6.1 Conclusions

The significant results of this study demonstrate that implanting hydrogen into a vacuum evaporated amorphous silicon film is effective in reducing the density of localized states in the mobility gap, as illustrated by the field effect measurements. The controllable hydrogenation of evaporated amorphous silicon has been performed by ion implantation followed by a low temperature thermal activation. The effects of hydrogenation and those of structure disorder from film fabrication can be independently controlled by separating the process of hydrogenation from that of amorphous film deposition. This technique, as compared with glow discharge or sputtering methods, minimizes the number of fabrication variables and hence facilitates the study of the hydrogenation phenomenon. Quantitatively controlled hydrogenation is achieved, while preserving some of the advantages of the evaporation method, such as fabricating large area samples with excellent uniformity and consistency. A

comparison of electrical properties of the evaporated films before and after hydrogenation provides valuable information on the effects of hydrogenation independent of fabrication.

After hydrogenation, a field effect conductance change of four orders of magnitude was observed on the devices which were not thermally annealed *in situ* following film deposition. Almost three orders of magnitude reduction in the density of localized states near the Fermi level had been achieved. The effect of hydrogen in reducing the density of localized states was quantified by varying the implant dosage. Analyses of the field effect data indicated that the density of localized states near the Fermi level decreased as the implant dosage was increased while all other experimental procedures were fixed. As more hydrogen is incorporated in the a-Si, more dangling bonds were passivated by the implanted hydrogen hence the density of localized states was further reduced.

The vacuum evaporated a-Si is quite porous and the internal surfaces can oxidize with the substantial oxygen incorporation when the films are exposed to the air. By performing a 400°C anneal for four hours the film porosity was greatly reduced. The effect of *in situ* thermal annealing on the evaporated a-Si films prior to hydrogen implantation reduced the voids, alleviated the internal oxidation and enhanced the effectiveness of the subsequent hydrogenation. A field effect conductance change of six orders of magnitude was observed which yielded a density of localized states near the Fermi level of $4 \times 10^{17}/cm^3$-eV, approaching that of high quality glow discharge produced films. The localized states have been further reduced by several orders of magnitude as compared to the results of non *in situ* anneal case. The effect of the *in situ* thermal annealing on vacuum evaporated a-Si prior to hydrogenation demonstrated the

capability of this technique.

6.2 Recommendations for Future Research

The following recommendations are for future research which involves the study of basic material properties of a-Si. Exploration of devices and applications of a-Si is not intended.

The most significant results of this study demonstrate that the density of localized states in the mobility gap has been reduced to $4x10^{17}/cm^3$-eV on the evaporated a-Si by combining the processes of *in situ* thermal anneal and hydrogenation with a high implant dosage. As indicated in Chapter 3 section 3.4, much of implanted hydrogen went through the a-Si film and was located in the silicon dioxide insulator due to the thin a-Si film and the minimum implant energy available at Purdue. In order to keep more implanted hydrogen in the a-Si film, to optimize the hydrogenation technique, a thin film (photoresist) overcoating the wafer is suggested. When the hydrogen species reach the photoresist-amorphous silicon interface, the energy will be reduced. The thickness of the thin masking photoresist should be carefully determined. The concentration profile of the implanted hydrogen in two different materials (i.e. photoresist and a-Si) with different stopping powers should be simulated beforehand. Care also should be taken to remove the post implanted photoresist. In some cases ion bombarded photoresist is hard to remove.

With the lower density of localized states, a-Si:H films produced by this technique should be able to be doped (by ion implantation) into n-type or p-type materials. In fact, seeking the possibility of doping evaporated a-Si should be a goal for the hydrogenated material. However several difficulties may occur in doping. It is speculated that radiation damage may be more serious than hydrogen implantation when the conventional dopants (Phosphorus for n-type and Boron for p-type) are used as the implant species; even with low acceleration voltages. This radiation damage which occurs due to the heavy implanted ions may partially break apart the already formed Si-H bonds in a-Si:H network in addition to breaking some Si-Si bonds. In crystalline silicon, radiation damage is removed by subsequent thermal annealing at a high temperature (800°C to 900°C). This is not possible for the a-Si since it crystallizes at about 620°C. In addition hydrogen starts to effuse out of the film at about 290°C as indicated in Chapter 4, section 4.5. Therefore how much radiation damage can be removed and how much activation of the implanted species can be achieved by low temperature annealing are two major concerns in the doping process. How serious the problem will be is unknown until some experiments have been performed.

If radiation damage is as serious as predicted, the following suggestions are recommended :

(1) Do some thermal annealing during the implant. The temperature should be below 260°C; 230°C is suggested. In this way, the damage produced by ion bombardment is annealed during irradiation, which may prevent the clustering of small defects into larger microvoid structures.

(2) Seek alternative lighter dopant species other than Phosphorus and Boron. Li^+ is recommended for a donor type dopant and should produces less

radiation damage.

(3) Try Laser annealing.

(4) Try using Fluorine as a bond terminator for unsatisfied silicon bonds in a-Si. As indicated in Chapter 2, section 2.2B, fluorine forms a single bond with silicon more tightly than hydrogen. Published reports [74,75] indicate that fluorine has remained in the a-Si film and kept their bonds with Si even after an annealing at 600°C. If the same reduction in the density of localized states can be achieved by this terminator, a higher temperature post-implant thermal anneal is possible.

Finally, it is suggested to use Molecular Beam Epitaxial (MBE) techniques to produce and study the material properties of a-Si and a-Si:H. High quality a-Si films, with very low density of localized states should be able to be produced on the amorphous substrate (SiO_2 for example). Also available is the "in process" analytical instruments to monitor the amorphous structure and hydrogen content during film deposition. If this technique is successful, many more research projects could be designed.

LIST OF REFERENCES

[1] G. W. Neudeck, A. K. Malhotra, "An Amorphous Silicon Thin Film Transistor : Theory and Experiment", Solid State Electronics, 19, 721 (1976)

[2] H. C. Tuan, M. J. Thompson, N. M. Johnson, R. A. Lujan, "Dual-gate a-Si:H Thin Film Transistors", IEEE Electron Device Letters, EDL-3, 357 (1982)

[3] A. I. Lakatos, "Promise and Challenge of Thin Film Silicon Approaches to Active Matrices", IEEE Trans. on Electron Devices, ED-30, 5, 525 (1983)

[4] D. G. Ast, "Materials Limitations of a-Si:H Transistors", IEEE Trans. on Electron Devices, ED-30, 5, 532 (1983)

[5] S. Kishida, Y. Nara, O. Kobayashi, M. Matsumura, "Amorphous Silicon Charge Coupled Devices", Applied Physics Letters, 41(12), 1154 (1982)

[6] M. Matsumura, H. Hayama, Y. Nara, K. Ishibashi, "Amorphous Silicon Image Sensor IC", IEEE Electron Device Letters, EDL-1, 182 (1980)

[7] D. Adler, Amorphous Semiconductors, (CRC press, Cleveland, Ohio) 1972

[8] W. E. Spear, P. G. Lecomber, "Investigation of the Localized State Distribution in a-Si Films", J. Non-Cryst. Solids, 8, 727 (1972)

[9] R. C. Chittic, J. H. Alexander, "The Preparation and Properties of Amorphous Silicon", J. Electrochem. soc., 116, 1,77 (1969)

[10] J. C. Knights, "Substitutional Doping in Amorphous Semiconductors, The As-Si System", Philos, Mag., 34, 663 (1976)

[11] D. E. Carlson, U. S. Patent No. 4064521 (1977)

[12] G. A. N. Connell, J. R. Pawlik, "Hydrogenation in Structural and Electronic Studies of Gap States in Amorphous Germanium", phys. Rev., B13, 787 (1976)

[13] M. Hirose, M. Taniguchi, T. Nakashita, Y. Osaka, T. Suzuki, S. Hasegawa and T. Shimizu, "Defect Compensation in Doped CVD Amorphous Silicon", J. Non-Crystalline Solids 35-36, 297 (1980)

[14] M. Akhtar, V. L. Dalal, K. R. Ramaprasad, S. Gau and J. A. Cambrige, "Electronic and Optical Properties of Amorphous Si:H Films Deposited by Chemical Vapor Deposition", Appl. Phys. Lett., 41, 12, 1146 (1982)

[15] Toshio Nakashita, Yukio Osaka, Masataka Hirose, Takeshi Imura and Akio Hiraki, "Defect State and Electronic Properties of Post-Hydrogenated CVD Amorphous Silicon", Appl. Phys., 22, 12, 1766 (1983)

[16] C. C. Schubert, P. H. Fany and J. H. Kinnier, "Electron-Beam Evaporated Amorphous Silicon Multiple Cascade Solar Cells", Jap. J. Appl. Phys., 20, 6, L437 (1981)

[17] J. I. Pankove, M. A. Lampert, and M. L. Tarng, "Hydrogenation and Dehydrogenation of Amorphous and Crystalline Silicon", Appl. Phys. Lett., 32, 7, 439 (1978)

[18] J. Jang, J. H. Kang and C. Lee, "Hydrogenation and Doping of Vacuum- Evaporated A-Si", J. Non-Cryst. Solids, 35-36, 313 (1980)

[19] P. S. Peercy, H. J. Stein, and D. S. Ginley, "Effect of Disorder on the Hydrogen Content in Si", Appl. phys. Lett., 36, 678 (1980)

[20] P.G. LeComber, A. Madan, W. E. Spear, "Electronic Transport and State Distribution in a-Si Films", J. Non-Cryst. Solids, 11, 219 (1972)

[21] D. E. Carlson, C. R. Wronski, J. Electron. Mater., 6, 95 (1977)

[22] H. Fritzsche, C. C. Tsai, P. Persans, "Amorphous Semiconducting Silicon-Hydrogen Alloys", Solid State Technol., 21, 55 (1978)

[23] A. Madan, P. G. LeComber, W. E. Spear, "Investigation of the Density of Localized States in a-Si Using the Field Effect Technique", J. Non-Cryst. Solids, 20, 239 (1976)

[24] N. B. Goodman, "Effect of Annealing and Light Exposure on the Field Effect Density of States in Glow Discharge a-Si:H", Philos. Mag., B45, 4, 407 (1982)

[25] C. C. Tsai, H. Fritzsche, "Effect of Annealing on the Optical Properties of Plasma Deposited a-Si:H", Sol. Energy Mater., 1, 29 (1979)

[26] D. Kaplan, N. Sol, G. Velaso, P. A. Thomas, "Hydrogenation of Evaporated Amorphous Silicon Films by Plasma Treatment", Appl. Phys. Lett., 33, 440 (1978)

[27] A. J. Lewis, "Use of Hydrogenation in the Study of the Transport Properties of Amorphous Germanium", Phys. Rev., B14, 658 (1976)

[28] M. Hirose, M. Taniguchi, Y. Osaka, in Amorphous and Liquid Semiconductors (edited by W. E. Spears, Dundee, Scotland) P.352 (1977)

[29] N. F. Mott, E. A. Davis, Electronic Processes in Non-Crystalline Materials, (Clarendon press, Oxford) 1971

[30] J. C. Knights, G. Lucovsky, Hydrogen in Amorphous Semiconductors, (CRC press, Critical Reviews in Solid State and Materials Sciences), vol. 9, issue 3, 1980

[31] M. H. Brodsky, editor, Amorphous Semiconductors, (Topics in Applied Physics, Springer-Verlag, Berlin), vol. 36, 1979

[32] M. H. Brodsky, R. S. Title, K. Weiser, G. D. Pettit, "Structure, Optical, and Electrical Properties of Amorphous Silicon Films", Phys. Rev. B1, 2632 (1970)

[33] R. Grigorovici, Chapter 5 in "Electronic and Structural Properties of Amorphous Semiconductors", edited by P. G. LeComber, (Academic press, London & New York), 1973

[34] R. Mosseri, C. Sella, J. Dixmier, "X-Ray Diffraction Study of the Effect of Hydrogen Atoms on the Si-Si Atomic Short-Range Order in Amorphous Silicon", Phys. Stat. Sol.(a) 52, 475 (1979)

[35] G. S. Cargill, "Structure of Metallic Alloy Glasses", Solid State Phys. 30, 227 (1975)

[36] L. Guttman, "Model of Hydrogenated Amorphous Silicon", Phy. Rev. B23, 4, 1866 (1981)

[37] A. C. Wright, A. J. Leadbetter, "Diffraction Studies of Glass Structure", Phys. Chem. Glasses, 17, 122 (1976)

[38] D. E. Polk, "Structural Model for Amorphous Silicon and Germanium", J. Non-Cryst. Solids, 5, 365 (1971)

[39] Handbook of Chemistry and Physics, (Chemical Rubber Co. press, Cleveland), 39th edition, 1957

[40] S. C. Moss, J. F. Graczyk, Proc. 10th Inter. Conf. Phys. Semiconductors, Cambridge, Mass., (1970)

[41] B. Kramer, D. Weaire, in ref. 20, p. 9 (op. cit.)

[42] E. A. Davis, in ref. 20, p. 41 (op. cit.)

[43] D. Weaire, M. F. Thorpe, "Electronic Properties of An Amorphous Solid. I. A Simple Tight-binding Theory", Phys. Rev., B4, 2508 (1971)

[44] M. F. Thorpe, D. Weaire, "Electronic Properties of An Amorphous Solid. II. Further Aspects of the Theory", Phys. Rev., B4, 3518 (1971)

[45] N. F. Mott, Chapter 1 in ref. 22 (op. cit.)

[46] P. W. Anderson, "Absence of Diffusion in Certain Random Lattices" , Phys. Rev., 109, 1492 (1958)

[47] N. F. Mott, "Conduction in Non-crystalline Systems. IV. Anderson Localization in a Disordered Lattice", Philos. Mag., 22, 7 (1970)

[48] M. H. Cohen, H. Fritzsche, S. R. Ovshinsky, "Simple Band Model for Amorphous Semiconducting Alloys", Phys. Rev. Lett. 22, 1065 (1969)

[49] E. A. Davis, N. F. Mott, "Conduction in Non-crystalline Systems. V. Conductivity, Optical Absorption and Photoconductivity in Amorphous Semiconductors", Philos. Mag., 22, 903 (1970)

[50] D. Emin, in ref. 22, p. 261 (op. cit.)

[51] D. T. Pierce, W. E. Spicer, "Electronic Structure of Amorphous Silicon from Photoemission and Optical Studies", Phys. Rev., B5, 3017 (1972)

[52] S. K. Bahl, S. M. Bhagat, "Properties of Amorphous Silicon Films Dependence on Deposition Conditions", J. Non-Cryst. Solids, 17, 409 (1975)

[53] G. W. Neudeck, A. K. Malhotra, "Field Effect Conductance Modulation in Vacuum Evaporated Amorphous Silicon Films", J. Appl. Phys., 46, 1, 239 (1975)

[54] G. W. Neudeck, A. K. Malhotra, "Theory and Interpretation of the Field Effect Conductance Experiment in Amorphous Silicon", J. Appl. Phys., 46, 6, 2662 (1975)

[55] M. H. Kriegel, Ph.D. Thesis, Purdue University (1978)

[56] T. Suzuki, M. Hirose, "Electrical Transport and Photoconductivity in Amorphous Silicon", Phys. Stat. Sol., (a), 42, 337 (1977)

[57] A. E. Owen, W. E. Spear, "Electronic Properties and Localized States in Amorphous Semiconductors", Phys. Chem. Glasses, 17, 174 (1976)

[58] A. Miller, E. Abrahams, "Impurity Conduction at Low Concentrations" Phys. Rev., 120, 3, 745 (1960)

[59] N. F. Mott, "Conduction in Non-crystalline Materials. III. Localized States in a Pseudogap and Near Extremities of Conduction and Valence Bands", Philos. Mag., 19, 835 (1969)

[60] H. Overhof, "Hopping Conductivity in Disordered Solids" in Advances in Solid State Physics, vol. 16, p. 239, (1976)

[61] P. Nagels, in ref. 20, p. 120 (op. cit.)

[62] P. A. Thomas, M. H. Brodsky, D. Kaplan, "Electron Spin Resonance of Ultrahigh Vacuum Evaporated Amorphous Silicon : in situ and ex situ Studies" Phys. Rev., B18, 3059 (1978)

[63] G. L. Pearson, J. Bardeen, "Electrical Properties of Pure Silicon and Silicon Alloys Containing Boron and Phosphorus", Phys. Rev., 75, 865 (1949)

[64] R. Grigorovici, "Amorphous Germanium and Silicon (Structure and Transport Phenomena)", Mat. Res. Bull., 3, 13 (1968)

[65] P. A. Walley, "Electrical Conduction in Amorphous Silicon and Germanium", Thin Solid Films, 2, 327 (1968)

[66] P. G. LeComber, A. Madan, W. E. Spear, "Electronic Transport and State Distribution in Amorphous Silicon Films", J. Non-Cryst. Solid, 11, 219 (1972)

[67] D. E. Carlson, C. R. Wronski, "Amorphous Silicon Solar Cell", Appl. Phys. Lett., 28, 671 (1976)

[68] J. C. Knights, in Structure and Excitation in Amorphous Solids, edited by G. Lucovsky, (AIP), p. 296, (1976)

[69] P. J. Zanzucchi, C. R. Wronski, "Optical and Photoconductive Properties of Discharge Produced Amorphous Silicon", J. Appl. Phys., 48, 5227 (1977)

[70] M. H. Brodsky, M. Cardona, "Infrared and Raman Spectra of the Silicon-Hydrogen Bonds in Amorphous Silicon Prepared by Glow Discharge and Sputtering", Phys. Rev., B16, 3556 (1977)

[71] J. C. Knights, G. Lucovsky, "Hydrogen Bonding in Silicon-Hydrogen alloys", Philos. Mag., B37, 467 (1978)

[72] G. Lucovsky, R. J. Nemanich, "Structural Interpretation of the Vibrational Spectra of a-Si:H Alloys", Phys. Rev., B19, 2064 (1979)

[73] V. Augelli, R. Murri, "Physical Characterization of Halogenated and Hydrogenated Amorphous Silicon Films", Thin Solid Film, 69, 315 (1980)

[74] H. Matsumura, Y. Nakagome, "A Heat-resisting New Amorphous Silicon", Appl. Phys. Lett., 36(6), 439 (1980)

[75] Y. Nakagome, H. Matsumura, "A Comparison of the Thermal Stabilities of Fluorinated and Hydrogenated Amorphous Silicon", Japanese Journal of Applied Physics, 19, 2, L87 (1980)

[76] CRC Handbook of Chemistry and Physics, 55th edition, P.F204 (1974)

[77] P. Potzinger, F. W. Lampe, "An Electron Impact Study of Ionization and Dissociation of Monosilane and Disilane", J. Phys. Chem. 73, 3912 (1969)

[78] D. A. Anderson, G. Moddel, M. A. Paesler, W. Paul, "Importance of Argon Pressure in the Preparation of RF Sputtered Amorphous Silicon-Hydrogen Alloys", Vac. Sci. Technol., 16, 906 (1979)

[79] J. I. Pankove, M. A. Lampert, M. L. Tang, "Hydrogenation and Dehydrogenation of Amorphous and Crystalline Silicon", Appl. Phys. Lett. 32, 439 (1978)

[80] P.221, in ref. 19 (op. cit.)

[81] H. Fritzsche, M. Tanielian, C. C. Tsai, P. J. Gaczi, "Hydrogen Content and Density of Plasma Deposited Amorphous Silicon-Hydrogen", J. Appl. Phys., 50, 3366 (1979)

[82] J. A. McMillan, E. M. Peterson, "Kinetics of Decomposition of Amorphous Hydrogenated Silicon Films", J. Appl. Phys., 50, 5238 (1979)

[83] K. J. Matysik, C. J. Mogab, "Hydrogen Evolution from Plasma Deposited Amorphous Silicon Film", J. Vac. Sci. Tech., 15, 2, 302 (1978)

[84] J. I. Pankove, D. E. Carlson, "Photoluminescence of Hydrogenated Amorphous Silicon", Appl. Phys. Lett., 31, 7, 450 (1977)

[85] J. C. Knights, I. Solomon, "Optically Induced Electron Spin Resonance in Doped Amorphous Silicon", Solid State Commu., 22, 133 (1977)

[86] J. R. Pawlik, W. Paul, "ESR and Photo-ESR in Doped and Undoped a-Si and Ge", Proceedings of the 7th International Conference on Amorphous and Liquid Semiconductors, (edited by W. E. Spear, Edinburgh, 1977) p. 437

[87] N. F. Mott, E. A. Davis, in ref. 18, p. 285 (op. cit.)

[88] A. J. Lewis, G. A. N. Connell, W. Paul, in AIP Conf. Proc., 20, 27 (1974)

[89] D. A. Anderson, T. Moustakas, W. Paul, "Effect of Hydrogen on the Transport Properties of a-Si", in ref. 77, p. 334, (op. cit.)

[90] N. Van Dong, T. Quoc Hai, "Electronic Transport in Doped a-Ge and a-Si Prepared by DC Cathodic Sputtering", Phys. Status Solidi, B, 88, 555 (1978)

[91] E. N. Economou, D. A. Papaconstantopoulos, "Theory of Hydrogenated Silicon", Phys. Rev., B23, 4, 2024 (1981)

[92] R. J. Loveland, W. E. Spear, "Photoconductivity and Absorption in Amorphous Silicon", J. Non-Cryst. Solid, 13, 55 (1973)

[93] M. H. Brodsky, J. J. Cuomo, F. Evangelisti, "Photoluminescence of Hydrogenated and Deuterated Sputtered a-Si", in ref. 77, p. 397 (op. cit.)

[94] A. Barna, "A Comparative Study of the Structure of Evaporated and Glow Discharged Silicon", Phys. Stat. Sol., (a), 41, 81 (1977)

[95] W. Y. Ching, D. J. Lam, "Electronic States and Bonding Configurations in Hydrogenated Amorphous Silicon", Phys. Rev., B21, 2378 (1980)

[96] W. Y. Ching, C. C. Lin, L. Guttman, "Structural Disorder and Electronic Properties of Amorphous Silicon", Phys. Rev., B16, 5488 (1977)

[97] W. Y. Ching, C. C. Lin , D. L. Huber, "Electronic Energy Structure of Amorphous Silicon", Phys. Rev., B14, 620 (1976)

[98] W. E. Spear, P. G. LeComber, "Substitutional Doping of Amorphous Silicon", Solid State Commun., 17, 1193 (1975)

[99] W. Paul, A. J. Lewis, G. A. N. Connell, T. D. Moustakas, "Doping, Schottky Barrier and p-n Junction Formation in Amorphous Germanium

and Silicon by RF Sputtering", Solid State Commun. 20, 969 (1976)

[100] W. E. Spear, P. G. LeComber, "Electronic Properties of Substitutionally Doped Amorphous Si and Ge", Philos. Mag. 33, 935 (1976)

[101] N. B. Goodman, H. Fritzsche, "Analysis of Field Effect and Capacitance Voltage Measurements in Amorphous Semiconductors", Philos. Mag., B42, 149 (1980)

[102] N. B. Goodman, H. Fritzsche, H. Ozaki, "Determination of the Density of States of a-Si:H Using the Field Effect", J. Non-Cryst. Solids, 35, 599 (1980)

[103] D. L. Staebler, C. R. Wronski, "Reversible Conductivity Changes in Discharge Produced Amorphous Silicon", Appl. Phys. Lett., 31, 292 (1977)

[104] A. J. Snell, K. D. Mackenzie, W. E. Spear, P. G. LeComber, "Application of Amorphous Silicon Field Effect Transistors in Addressable Liquid Crystal Display Panels", Appl. Phys., 24, 357 (1981)

[105] S. Kawai, N. Takagi, T. Kodama, K. Asama, S. Yangisawa, Proc. SID82 Digest, p. 42 (1982)

[106] M. LeContellec, F. Morin, J. Richard, P. Coissard, M. Morel, M. Bonnel, Proc. SID82 Digest, p.44 (1982)

[107] M. J. Thompson, N. M. Johnson, M. D. Moyer, R. Lujan, "Thin Film Transistors on a-Si:H", IEEE Electron Devices ED-29, 10, 1643 (1982)

[108] Y. Nara, M. Matsumara, "An Amorphous Silicon Integrated Inverter", IEEE Electron Devices, ED-29, 10, 1646 (1982)

[109] H. Fritzsche, Chapter 2 in ref. 22, "A Review of Some Electronic Properties of Amorphous Substances" (op. cit.)

[110] C. R. Wronski, D. E. Carlson, R. E. Daniel, "Schottky Barrier Characteristics of Metal-Amorphous Silicon Diodes", Appl. Phys. Lett. 29, 9, 602 (1976)

[111] P. J. Zanzucchi, C. R. Wronski, D. E. Carlson, "Optical and Photoconductive Properties of Discharge Produced Amorphous Silicon", J. Appl. Phys., 48, 5227 (1977)

[112] B. E. Deal, "The Current Understanding of Changes in the Thermally Oxidized Silicon Structure", J. Electrochem. Soc., 112, 198 (1974)

[113] R. J. Kriegler, Y. C. Cheng, D. R. Colton, "The Effect of HCl and Cl_2 on the Thermal Oxidation of Silicon", J. Electrochem. Soc., 119, 388

(1972)

[114] R. J. Kriegler, "Neutralization of Na^+ Ions in HCl-Grown SiO_2", Appl. Phys. Lett., 20, 449 (1972)

[115] E. H. Nicollian, A. Goetzberger, C. N. Berglund, "Avalanche Injection Currents and Charging Phenomena in Thermal SiO_2", Appl. Phys. Lett., 15, 174 (1969)

[116] R. J. Kutko "Ellipsometry for Semiconductor Process Control", Solid State Technology, February, 43 (1978)

[117] H. J. Stein, P. S. Peercy, "Controlled Hydrogenation of Amorphous Silicon at Low Temperature", Appl. Phys. Lett., 34, 604 (1979)

[118] W. S. Johnson, J. F. Gibbons, Projected Range Statistics in Semiconductors, 2nd edition, (Dowden, Hutchinson, Ross, Stroudsburg) 1975

[119] S. C. Mass, J. F. Graczyk, "Evidence of Voids within the As-Deposited Structure of Glassy Silicon", Phys. Rev. Lett., 23, 1167 (1969)

[120] M. H. Brodsky, in ref. 20, p. 3 (op. cit.)

[121] I. Soloman, in ref. 20, p. 193 (op. cit.)

[122] A. Triska, D. Denmison, H. Fritzsche, "Hydrogen Content in a-Ge and a-Si Prepared by RF Decomposition of GeH_4 and SiH_4", Bull. Am. Phys. Soc., 20, 392 (1975)

[123] M. H. Brodsky, M. A. Frisch, J. F. Ziegler, W. A. Lanford, "Quantitative Analysis of Hydrogen in Glow Discharge Amorphous Silicon", Appl. Phys. Lett., 30, 561 (1977)

[124] G. J. Clark, C. W. White, D. D. Allred, B. R. Appleton, C. W. Magee, D. E. Carlson, "The Use of Nuclear Reactions and SIMS for Quantitative Depth Profiling of Hydrogen in Amorphous Silicon", Appl. Phys. Lett., 31, 582 (1977)

[125] J. C. Knights, G. Lucovsky, in ref. 19, p. 211 (op. cit.)

[126] W. E. Spear, in Amorphous and Liquid Semiconductors, edited by J. Stuke and W. Brenig (Taylor and Francis, London 1974) p. 1-16

[127] D. K. Biegelsen, R. A. Street, C. C. Tsai, J. C. Knights, "Hydrogen Evolution and Defect Creation in Amorphous Si:H Alloys", Phys. Rev., B20, 4839 (1979)

[128] H. Fritzsche, "Characterization of Glow Discharge Deposited a-Si:H", Sol. Energy Mater., 3, 447 (1980)

[129] T. M. Donovan, K. Heineman, "High Resolution Electron Microscope Observation of Voids in Amorphous Ge", Phys. Rev. Lett., 27, 1794 (1971)

[130] F. L. Galeener, "Optical Evidence for a Network of Cracklike Voids in Amorphous Germanium", Phys. Rev. Lett., 27, 1716 (1971)

[131] H. Fritzsche, C. C. Tsai, "Porosity and Oxidation of Amorphous Silicon Films Prepared by Evaporation, Sputtering and Plasma Deposition", Sol. Energy Mater., 1, 471 (1979)

[132] C. C. Tsai, H. Fritzsche, "Sensitivity of Amorphous Silicon to Exposure to Air", Bul. Am. Phys. Soc., 24, 399 (1979)

[133] M. Tanielian, H. Fritzsche, C. C. Tsai, E. Symbalisty, "Effect of Adsorbed Gases on the Conductance of Amorphous Films of Semiconducting Silicon-Hydrogen Alloys", Appl. Phys. Lett., 33, 353 (1978)

[134] J. C. Bean, J. M. Poate, "Evidence for Void Interconnection in Evaporated Amorphous Silicon from Epitaxial Crystallization Measurements", Appl. Phys. Lett., 36, 59 (1980)

[135] M. Kuhn, "A Quasi-Static Technique for MOS C-V and Surface States Measurements", Solid State Electronics, 13, 873 (1970)

[136] Private work with J. A. Shields

[137] J. W. Mayer, L. Eriksson, J. A. Davis, Ion Implantation in Semiconductors (Academic press, New York 1970), p. 67

[138] R. H. Williams, R. R. Varma, W. E. Spear, P. G. LeComber, "The Fermi Level Position in Doped Amorphous Silicon", J. Phys. C12, L209 (1979)

[139] P. G. LeComber, W. E. Spear and A. Ghaith, "Amorphous-Silicon Field-Effect Device and Possible Application", Electron. Lett., 15, 179 (1979)

[140] Tohru Suzuki, Masataka Hirose and Yukio Osaka, "Influence of Gap States on Basic Characteristics of A-Si:H Thin Film Transistors", Jap. J. Appl. Phys., 21, 5, L315 (1983)

[141] Satoru Kishida, Yasuo Naruke, Yasutaka Uchida and Masakiyo Matsumura, "Theoretical Analysis of Amorphous-Silicon Field-Effect-Transistors", Jap. J. Appl. Phys., 22, 3, 511 (1983)

[142] A. C. Tickle, Thin Film Transistors, Wiley, New York (1969)

[143] Zhi Li and G. W. Neudeck, "The Static Characteristics of Hydrogenated Amorphous Silicon Thin-Film Transistors", Unpublished, (1983)

Appendix 1

Initial Wafer Cleaning Procedures

(1) Rinse in D.I. water 5 times

(2) Ultrasonic clean in Acetone for 5 minutes

(3) Ultrasonic clean in TCE for 10 minutes

(4) Ultrasonic clean in Acetone for 10 minutes

(5) Rinse in D.I. water 15 to 20 times

(6) Soak in Piranha (H_2O_2:H_2SO_4=1:1) for 10 minutes

(7) Rinse in D.I. water 15 times

(8) Etch in HF:D.I.=1:20 for 2 minutes (no ultrasonic)

(9) Rinse in D.I. water 15 to 20 times

Appendix 2

Computer Program for Evaluating the Density of States Distribution in a-Si

A computer program was employed to transcribe the field effect experimental data into the distribution of the localized states in a-Si. To run the computer program in the Purdue University Computer Center, the following job cards were used :

```
Account #, ID, MF100000, L5000, T1024, PR.
RFL (100000)
MNFFTN (U,N)
LDSET (PRESET=ZERO)
LGO.
#EOR
```

At the bottom of the main program, the required parameters and constants are first read in according to the order assigned in the program. The experimental data are read next. The initial guess of the distribution of the density of states are put at the end. It should be noted that an initial guess which is too far away may result in divergent results.

```
C * * * THIS VERSION OF FIELDEFF MODIFIES G(E) ITSELF TO FIT DATA * * *
C * * * FIELDEFF * * * FIRST SOLVES A SECOND ORDER DIFFERENTIAL EQUATION LIKE:
C *****          YDOTDOT=FUNCTION(X,Y,YDOT)             WHERE YDOT=DY/DX
C ***** GIVEN INITIAL VALUES OF Y AND YDOT AT THE FIRST VALUE OF X  (X=0.0)
C ***** THESE ARE YO, YDO AND ARE CALCULATED IN THE PROGRAM.
C ***** IT USES THE SOLUTION FOR POTENTIAL AS A FUNCTION OF DISTANCE
C ***** INTO THE SAMPLE TO COMPUTE THE CONDUCTANCE VERSUS VOLTAGE CURVE
C ***** IT ASSUMES T>O IN STATISTICAL WEIGHTS TO COMPUTE CHARGE DENSITY
C ***** VFIELD IS THE FIELD VOLTAGE (AWAY FROM VFBP) IN KILOVOLTS
C ***** VFBP IS APPLIED FIELD VOLTAGE THAT YIELDS NO BAND BENDING
C ***** IF TERSE=.TRUE. MUCH OF THE POSSIBLE OUTPUT IS OMITTED
C ***** TEMP IS TEMPERATURE OF SAMPLE IN DEGREES K
C ***** ALPHA IS RATIO OF ELECTRON TO HOLE CONDUCTANCES AT VFBP
C ***** SIGO IS THE CONDUCTANCE AT THE FLAT BAND POSITION
C ***** DELX IS STEP SIZE IN X FOR SOLVING DIFF. EQ'N ... DELX=DELXO AT X=O
C ***** THICK IS THE SAMPLE THICKNESS IN CM.
C ***** DSUB IS THE THICKNESS OF THE SUBSTRATE IN CM.
C ***** ESAM & ESUB ARE DIELECTRIC CONSTANTS OF SAMPLE AND SUBSTRATE
C ***** ESAM=12.0 FOR SILICON; ESUB=3.70 FOR QUARTZ; ESUB=9.3 FOR SI3N4
C ***** YMIN & YMAX ARE LIMITS ON PLOT OF VFIELD
C ***** IF ERROR=.TRUE. PROGRAM COMPUTES SIGMA FOR 1% ERROR IN YO
C ***** IF PLOTS=.TRUE. PROGRAM PLOTS SIGMA-CALCULATED VERSUS VFIELD
C ***** NDATA IS THE NUMBER OF DATA POINTS SPECIFIED
C ***** NALTER IS THE NUMBER OF DIFFERENT G(E)'S TO BE TRIED
C ***** MODIFIED DENSE(NN) IS IRONED OUT OVER (NN +/- IRON) EACH TIME
C ***** AMN IS THE "A" IN THE MEYER-NELDEL RULE:  SIG=SIGO*EXP(A*V)
C ***** (VDATA,SDATA) ARE PAIRS OF (VFIELD,SIGMA) DATA POINTS
C ***** SIGMA IS THE CONDUCTANCE IN INVERSE OHMS AT APPLIED VOLTAGE, VFIELD
C ***** NTOT IS THE TOTAL NUMBER OF ENERGY VALUES SEPARATED BY
C ***** DELE, AT WHICH DENSITY OF STATES, G(E), IS READ IN.
C ***** BOLTZ IS THE BOLTZMAN K FACTOR IN EV/DEGREE K
C ***** OEA IS THE SURFACE ELECTRON DENSITY ON THE SAMPLE (Q/(E*A))
0001          LOGICAL TERSE, ERROR, PLOTS
0002          DIMENSION EX(3000),V(3000),VD(3000),TITLE(20),DEX(3000),ROW(3000)
0003          DIMENSION VDATA(50),VCALC(50),PHIØ(50),SIGMA(50)
0004          DIMENSION GRAPH(2000),NSCALE(5),SLAST(50),SDATA(50),SCALC(50)
0005          DIMENSION RHO(200),EN(200),DENSE(200),DTEMP(200),DUNSE(200)
0006          COMMON/CHARGE/RHO,EN,NTOT,DELE,L,ROW,ESAM,ESUB
0007          DATA ITER/2/
0008          DATA NSCALE/1,0,3,0,3/
0009      100 READ(5,*,END=999) TEMP, ALPHA, SIGO, DELXO, THICK, DSUB,
             1 ESAM, ESUB, VFBP, TERSE
0010          READ(5,*)  XMAX, XMIN, YMAX, YMIN, ERROR, PLOTS
0011          READ(5,104) TITLE
0012      104 FORMAT(20A4)
0013          READ(5,*) NDATA, NALTER, IRON, AMN
0014          WRITE(6,106)
0015      106 FORMAT('1  DATA:',5X,'VFIELD (KV.)',5X,'SIGMA (MHO)')
```

```
                C  *
                C *** READ IN DATA FOR VFIELD AND SIGMA FROM VFBP TO MAXIMUM VFIELD,
                C *** THEN FROM VFBP TO MINIMUM VFIELD
                C  *
0016                  DO 110 N=1,NDATA
0017                  READ(5,*) VDATA(N),SDATA(N)
0018                  WRITE(6,108) VDATA(N),SDATA(N)
0019              108 FORMAT(' ',15X,F7.3,7X,E11.4)
0020                  SLAST(N)=1.0
0021              110 CONTINUE
0022                  READ(5,*) NTOT, DELE, ECEF
0023                  WRITE(6,112) NTOT
0024              112 FORMAT('1   THE DENSITY OF STATES (THE ARRAY,"DENSE") IS DEFINED A
                     1T ',I3,' VALUES OF THE ENERGY:',/,'O    I      ENERGY (EV.)      G(E
                     2) (EV-1 * CM-3)       RHO (ELECTRONS PER CC)')
                C  *
                C *** READ IN DENSITY OF STATES FOR ALL ENERGIES (E-FERMI IS ZERO)
                C *** BE CAREFUL TO READ IN DENSE(NN) IN ORDER OF INCREASING ENERGY
                C  *
0025                    IAMN=AMN
0026                  DO 115 NN=1,NTOT
0027                     READ(5,*) EN(NN), DENSE(NN)
0028                   IF(IAMN.EQ.15) DENSE(NN)=DENSE(NN)/3.
0029                   IF(IAMN.EQ.22) DENSE(NN)=DENSE(NN)/5.
0030                     EN(NN)=ECEF-EN(NN)
0031              115    DTEMP(NN)=DENSE(NN)
0032                  FACTOR=DSUB*1.81182E-9/ESUB
                C *** FACTOR=(4*PI*DSUB*E/ESUB) * (9.E11 CM/FARAD * .001 KV/VOLT)
                C *** FACTOR IS USED TO COMPUTE VCALC; I.E.:  CALCULATED V-FIELD
0033                  INALT=0
0034                  ALTER=AMINO(10,NALTER)
0035                  BOLTZ=8.617E-5
0036                  IF(TEMP.EQ.O.) TEMP=273.
0037                  TK=1./(BOLTZ*TEMP)
0038              121 YOO=O.
0039                  ELAST=0.0
0040                  INALT=INALT+1
0041                  AVEDFF=O.
                C  *
                C *** COMPUTE CHARGE DENSITY FROM DENSITY OF STATES
                C *** USING T.NE.O STATISTICAL WEIGHTS
                C  *
0042                  NSUB = NTOT-1
0043                  DO 124 NN=1,NTOT
0044                     DTEMP(NN)=DENSE(NN)
0045                     RHO(NN)=0.5*DELE*(DENSE(1)*(1./(1.+EXP((EN(1)-EN(NN))*TK))-
                     1   1./(1.+EXP(EN(1)*TK))) + DENSE(NTOT)*(1./(1.+EXP((EN(NTOT)-
                     2   EN(NN))*TK))-1./(1.+EXP(EN(NTOT)*TK))))
```

```
0046          DO 123 IN=2,NSUB
0047   123       RHO(NN)=RHO(NN)+DELE*DENSE(IN)*
          1      (1./(1.+EXP((EN(IN)-EN(NN))*TK))-1./(1.+EXP(EN(IN)*TK)))
0048   124    WRITE(6,131) NN, EN(NN), DENSE(NN), RHO(NN)
0049   131    FORMAT('   ',I3,8X,F7.3,10X,E11.4,14X,E11.4)
0050       SLOPE=0.01
0051       VALUE=0.020
0052       WRITE(6,149) TITLE, INALT, NALTER
0053   149 FORMAT('-      ',20A4,/,'0  TRIAL #',I2,' OF ',I2,' FOR G(E)')
0054       WRITE(6,150) THICK, DSUB, TEMP, ALPHA, VFBP, SIGO, DELXO, AMN
0055   150 FORMAT('0    SAMPLE THICKNESS =',E11.4,' CM.',/,'       SUBSTRATE TH
          1ICKNESS =',E11.4,' CM.',/,'      SAMPLE TEMPERATURE =',F6.1,' DEGRE
          2ES KELVIN',/,'      ALPHA =',E10.3,/,'      FIELD VOLTAGE NEEDED FOR
          3 NO BAND BENDING (VFBP) IS ',F7.3,' KV.',/,'      CONDUCTANCE AT VF
          4BP IS ',E11.4,' MHO',/,'      FIRST STEP SIZE IN X ',
          5'(DELXO) IS ',E11.4,' CM.',/,'0      MEYER-NELDEL PARAMETER (SIG =
          6SIGO*EXP(A*V)) IS A =',F5.1,/,'-     ')
0056       WRITE(6,152) VALUE, SLOPE, IRON
0057   152 FORMAT('0  ACCEPTABLE LIMITS FOR CONVERGENCE OF SOLUTION ARE:'
          1 ,/,'    POTENTIAL MUST BE LESS THAN',F7.4,' TIMES THAT AT X=0'
          2 ,/,'    SLOPE MUST BE LESS THAN',F7.4,' TIMES THAT AT X=0'
          3 ,/,'    THE ARRAY DENSE(N) IS SMOOTHED OUT OVER N +/-'
          4 ,I2,' EACH TIME IT IS MODIFIED')
0058       WRITE(6,153)
0059   153 FORMAT('- VFIELD  CONDUCTANCE  DIFF.CAP.     Q/E*A  NTRY   DELVO'
          1,7X,'VO',6X,'VDOTO',7X,'XLAST',6X,'VLAST',4X,'VDOTLAST  LMAX',3X,
          2'VCALC  PCT.',/,'    (KV)',7X,'(MHO)    (FD*CM-2)   ELEC*CM-2',6X,
          32('(VOLTS)   '),2X,'(V/CM)',8X,'(CM)',6X,'(VOLTS)',4X,'(V/CM)',10X,
          4'(KV)  ERROR')
       C  *
       C *** SET UP TO SOLVE POISSON'S EQUATION
       C  *
0060       DO 971 NVF=1,NDATA
0061       VFIELD=VDATA(NVF)-VFBP
0062       MISS=0
0063       IF(NVF.EQ.1) GO TO 161
0064       IF((VDATA(NVF)-VFBP)*(VDATA(NVF-1)-VFBP).LE.0.) QEA=0.0
0065       GO TO 162
0066   161 QEA=0.0
0067   162 IF(VALUE.LE.0.02.AND.MISS.EQ.0) QLAST=QEA
0068       QEA=VFIELD/FACTOR
0069       SLOPE=0.01
0070       VALUE=0.020
0071   163 NTRY=0
0072       IF(VALUE.GT.0.02) WRITE(6,164)VALUE, VFIELD
0073   164 FORMAT('0 =>=>=> ACCEPTABLE LIMITS FOR CONVERGENCE HAVE BEEN RAISE
          1D SO THAT:',/,'           POTENTIAL MUST BE LESS THAN',F7.4,' TIMES
          2THAT AT X=0',/,'           FOR VFIELD=',F7.4,'KILOVOLTS ONLY')
```

```
      C   *
      C *** SEARCH FOR VALUE OF YO THAT GIVES SOLUTION TO POISSON'S
      C *** EQUATION CONSISTANT WITH BOUNDARY CONDITIONS
      C   *
0074        IF(ABS(VFIELD).GT.1.E-5) GO TO 168
0075    165 YDO=0.
0076        YO=0.
0077        DELYO=1.E-15
0078        VFIELD=1.E-20
0079        AREA=0.
0080        LMAX=2
0081        DO 166 L=1,2
0082        ROW(L)=0.
0083        DEX(L)=DELXO
0084        EX(L)=0.0
0085        V(L)=0.
0086    166 VD(L)=0.
0087        ELAST=0.
0088        GO TO 502
0089    168 IF(VALUE.LE.0.02.AND.MISS.EQ.0) ELAST=YOO
0090        NDXO=0
0091        IF(NVF.EQ.1) GO TO 169
0092        IF((VDATA(NVF)-VFBP)*(VDATA(NVF-1)-VFBP).LT.0.)
           1 ELAST=SIGN(DELE/100.,VFIELD)
0093    169 DELYO = SIGN(0.03,VFIELD)
0094        IF(ELAST*VFIELD.LT.0.) ELAST=-ELAST
0095        YO=ELAST
0096    171 ITIME=1
0097    175 CONTINUE
      C   *
      C *** SOLVE FOR Y(X) GIVEN YO=Y(O) AND YDO=YDOT(O)
      C *** USING A PREDICTOR CORRECTOR METHOD
      C   *
0098        IF(NTRY.GE.1.AND.VALUE.GT.0.02) WRITE(6,180) VFIELD, L, V(L),
           1 VD(L), EX(L), DEX(L), YL, DELYO, NTRY
0099    180 FORMAT(' ......VFIELD=[illegible]3,'   L=',I3,'   V=',E10.3,
           1 '   VD=',E10.3,'   [illegible]E10.3,'   DELX=',E10.3,'   YO=',F7.4,
           2 '   DELYO=',F7.4,'  [illegible]RY=',I3)
0100    190 NTRY=NTRY+1
0101        IF(NTRY.GT.25) GO TO 955
0102        L=1
0103        DELX=DELXO
0104        DEX(1)=DELXO
0105        IF(MISS.EQ.1) YO=YO*.99
0106        IF(MISS.EQ.2) YO=YO*1.01/.99
0107        YDO=-((1000.*VFIELD-YO)/DSUB)*(ESUB/ESAM)
0108        EX(1) =0.0
0109        V(1)=YO
```

```
0110           VD(1)=YDO
0111           IF(VALUE.LE.0.02) YOO=YO
0112           AY=YO
0113           AYD=YDO
0114           AX=0.0
0115           IF(ABS(YDO).LE.1.E-50) YDO=.1E-50
0116           IF(ABS(YO).LE.1.E-50) YO=.1E-50
0117       200 L=L+1
0118           IF(L.GE.2999) GO TO 948
0119           IF(L.LE.2) GO TO 210
0120           DELX=DELX*(VD(L-2)/VD(L-1))*(VD(L-2)/VD(L-1))
0121           IF(DELX.LT.DELXO/100.) DELX=DELXO/100.
0122           IF(DELX.GT.0.005*THICK) DELX=THICK*0.005
0123           IF(AX.LT.THICK.AND.AX+DELX.GT.THICK) DELX=THICK-AX
0124       210 DEX(L)=DELX
0125           BY=AY+DELX*AYD
0126           CX=AX+DELX/2.
0127           CY=.5*(AY+BY)
0128           BYDD=DEON(CX,CY,AYD)
0129           BYD=AYD+DELX*BYDD
0130           I=1
0131       250 I=I+1
0132           DY=AY+DELX*.5*(AYD+BYD)
0133           DX=AX+DELX
0134           CYDD=DEON(CX,.5*(AY+DY),BYD)
0135           DYD=AYD+DELX*CYDD
0136           DYDD=DEON(DX,DY,DYD)
0137           BY=DY
0138           BYD=DYD
0139           BYDD=CYDD
0140           IF(I.LT.ITER) GO TO 250
0141           EX(L) =DX
0142           V(L)=DY
0143           VD(L)=DYD
0144           AX=DX
0145           AY=DY
0146           AYD=DYD
0147           YL=YO
0148           IF(MISS.NE.0) GO TO 494
          C  *
          C *** CHECK TO SEE IF Y(X) FITS BOUNDARY CONDITIONS
          C  *
0149           IF(AY/VFIELD.LT.0.) GO TO 490
0150           IF(AYD/YDO.LT.0.) GO TO 492
0151           IF(AY/YO.LE.VALUE.AND.(AYD/YDO.LE.SLOPE.OR.ABS(AYD).LE.100.))
              1 GO TO 500
0152           IF(AX.LT.THICK) GO TO 200
0153           IF(AY/YO.GE.0.) GO TO 492
```

```
0154         490 CONTINUE
            C  *   VALUE OF POTENTIAL HAS CHANGED SIGN
0155               IF(ITIME.EQ.2) DELYO=DELYO/2.
0156               IF(DELYO/YO.LT.1.E-5) GO TO 955
0157               YO=YO+DELYO
0158               GO TO 175
0159         492 CONTINUE
            C  *   SLOPE OF POTENTIAL HAS CHANGED SIGN
0160               IF(VD(L-1)/YDO.GT.O..AND.ABS(V(L-1)/YO).LE.VALUE) GO TO 496
0161               DELYO=DELYO/2.
0162               IF(DELYO/YO.LT.1.E-5) GO TO 955
0163               YO=YO-DELYO
0164               ITIME=2
0165               GO TO 175
0166         494 IF(AY/YO.GT.VALUE.AND.AYD/YDO.GT.SLOPE.AND.AX.LT.THICK)
                  1GO TO 200
0167               IF(AY/YO.GT.O..AND.AYD/YDO.GT.O.) L=L+1
0168         496 L=L-1
0169         500 LMAX=L
0170         502 YOO=YO
0171               LMAXI=LMAX-1
            C  *
            C ***  COMPUTE V-CALCULATED AS INSPIRED BY MADAN AND LE-COMBER
            C ***  COMPUTE DIFFERENTIAL CAPACITANCE (DCAP) ALSO
            C  *
0172               YOEL=YO-ELAST
0173               IF(ABS(YOEL).LT.1.E-10) YOEL=1.E-10
0174               DCAP=(1.602E-19)*(QEA-QLAST)/(YOEL)
0175               PHIO(NVF)=YO
0176               VCALC(NVF)=O.5*FACTOR*(DEX(1)*ROW(1)+DEX(LMAX)*ROW(LMAX))
0177               DO 565 L=2,LMAXI
0178         565     VCALC(NVF)=VCALC(NVF)+(DEX(L)*ROW(L))*FACTOR
0179               VCALC(NVF)=(VCALC(NVF)+VFBP)
            C  *
            C  ***
            C *****  THIS PART OF THE PROGRAM COMPUTES THE CONDUCTANCE OF A SAMPLE
            C *****  GIVEN THE POTENTIAL AS A FUNCTION OF DISTANCE INTO THE  SAMPLE
            C *****  WHERE EX(L) IS THE DISTANCE FROM THE SUBSTRATE SURFACE;
            C *****          V(L) IS THE POTENTIAL AT EX(L) IN UNITS OF EV.
            C *****  V(L) IS COMPUTED IN THE FIRST PART OF THE PROGRAM AS A FN OF EX(L)
            C  ***
            C   *
0180               IF(.NOT.TERSE.AND.MISS.EQ.O) WRITE(6,570)
0181         570 FORMAT('-',125('='),/,'O  L  ',9X,'X',12X,'SIGMA',11X,'DELI',
                  1 12X,'V',13X,'VDOT',11X,'DELX',7X,'VFIELD')
0182               AREA=O.5*ALPHA*(DEX(1)*(EXP((TK-AMN)*V(1))-1.)-DEX(LMAX)*
                  1 (EXP((TK-AMN)*V(LMAX))-1.))  +  O.5*(DEX(1)*(EXP(-(TK-AMN)*
                  2 V(1))-1.) - DEX(LMAX)*(EXP(-(TK-AMN)*V(LMAX))-1.))
```

```
0183          XXX=DEX(1)/2
0184          DO 620 L=2,LMAX
0185             IF(ABS((TK-AMN)*V(L)).GT.174.5) GO TO 965
0186             AREA=AREA+DEX(L)*(EXP((TK-AMN)*V(L))-1.)* ALPHA/2.
              1    +DEX(L)*(EXP(-(TK-AMN)*V(L))-1.)
0187             XXX=XXX+(DEX(L))
0188             IF(XXX.GT.THICK) GO TO 630
0189             DELI=AREA/((1.+ALPHA)*THICK)
0190             SIG=SIGO*(DELI+1.)
0191             IF(.NOT.TERSE.AND.MISS.EQ.O.AND.((L-1)/5.NE.L/5.OR.L.EQ.LMAX.
              1    OR.L.EQ.2)) WRITE(6,610) L,XXX,SIG,DELI,V(L),VD(L),DEX(L),
              2    VFIELD
0192      610 FORMAT(' ',I4,6(4X,E11.4),4X,F7.3)
0193      620    CONTINUE
0194      630 AVEOFF=AVEOFF+ABS(ALOG(SIG/SDATA(NVF)))/FLOAT(NDATA)
0195          SCALC(NVF)=SIG
0196          SIGMA(NVF)=ALOG10(SIG)
0197          IF(ABS(VDATA(NVF)).LT.1.E-15) VDATA(NVF)=1.E-15
0198          IF(ABS(VCALC(NVF)).LT.1.E-15) VCALC(NVF)=1.E-15
0199          VERR=(VCALC(NVF)-VDATA(NVF))/VDATA(NVF)*100.
0200          IF(.NOT.TERSE) WRITE(6,153)
0201          WRITE(6,625) VDATA(NVF),SIG,DCAP,QEA,NTRY,DELYO,YO,YDO,
             1 EX(LMAX),V(LMAX),VD(LMAX),LMAX,VCALC(NVF),VERR
0202      625 FORMAT('O',F7.3,3(2X,E10.3),1X,I2,1X,E10.3,2X,F7.3,2(2X,E10.3),
             1 2X,F7.4,2X,E10.3,1X,I4,2X,F6.3,1X,F6.2)
        C   *
        C *** MODIFY DENSE(NN) TO FIT DATA BETTER
        C   *
0203          IF(MISS.NE.O) GO TO 970
0204          IF(NALTER.LE.1) GO TO 970
0205          IF((SCALC(NVF)-SDATA(NVF))*(SLAST(NVF)-SDATA(NVF)).LT.O..AND.
             1 INALT.GT.1) GO TO 650
0206          DO 640 NN=1,NTOT
0207          IF(ABS(EN(NN)).GT.FLOAT(2*INALT)/ALTER) GO TO 640
0208          IF(YO.LT.O.) GO TO 635
0209          IF(ELAST-1./TK.LE.EN(NN).AND.EN(NN).LE.YO+3./TK.AND.
             1 SDATA(NVF).LT.SIGO) DTEMP(NN)=DTEMP(NN)*SQRT(SDATA(NVF)/SIG)
0210          IF(ELAST-1./TK.LE.EN(NN).AND.EN(NN).LE.YO+3./TK.AND.
             1 SDATA(NVF).GE.SIGO) DTEMP(NN)=DTEMP(NN)*SQRT(SIG/SDATA(NVF))
0211          GO TO 640
0212      635 IF(ELAST+1./TK.GE.EN(NN).AND.EN(NN).GE.YO-3./TK.AND.
             1 SDATA(NVF).LT.SIGO) DTEMP(NN)=DTEMP(NN)*SQRT(SDATA(NVF)/SIG)
0213          IF(ELAST+1./TK.GE.EN(NN).AND.EN(NN).GE.YO-3./TK.AND.
             1 SDATA(NVF).GE.SIGO) DTEMP(NN)=DTEMP(NN)*SQRT(SIG/SDATA(NVF))
0214      640 CONTINUE
0215          GO TO 970
0216      650 DO 660 NN=1,NTOT
0217          IF(ABS(EN(NN)).GT.FLOAT(2*INALT)/ALTER) GO TO 660
```

```
0218          IF(YO.LT.O.) GO TO 655
0219          IF(ELAST-1./TK.LE.EN(NN).AND.EN(NN).LE.YO+3./TK) DTEMP(NN) =
             1 EXP((ABS(ALOG(SCALC(NVF)/SDATA(NVF)))*ALOG(DUNSE(NN))
             2 + ABS(ALOG(SLAST(NVF)/SDATA(NVF)))*ALOG(DENSE(NN)))
             3 / ABS(ALOG(SCALC(NVF)/SLAST(NVF))))
      C  *
      C ***    WE HAVE MADE USE OF THE FACT THAT:
      C ***       ABS(ALOG(SCALC/SDATA))+ABS(ALOG(SLAST/SDATA))
      C ***         = ABS(ALOG(SCALC/SDATA)-ALOG(SLAST/SDATA))
      C ***         = ABS(ALOG(SCALC/SLAST))
      C  *
0220          GO TO 660
0221      655 IF(ELAST+1./TK.GE.EN(NN).AND.EN(NN).GE.YO-3./TK) DTEMP(NN) =
             1 EXP((ABS(ALOG(SCALC(NVF)/SDATA(NVF)))*ALOG(DUNSE(NN))
             2 + ABS(ALOG(SLAST(NVF)/SDATA(NVF)))*ALOG(DENSE(NN)))
             3 / ABS(ALOG(SCALC(NVF)/SLAST(NVF))))
0222      660 CONTINUE
0223          GO TO 970
      C  *
      C *** DIAGNOSTIC WRITE STATEMENTS FOLLOW: DO NOT DELETE
      C  *
0224      948 WRITE(6,949) VFIELD, L, AX, AY, DELXO
0225      949 FORMAT('    VFIELD=',F7.3,' KV . . .  L=',I4,'    AT X=',E10.3,
             1' CM. .  V=',E10.3,' VOLTS    DELXO =',E10.3,
             2 ' CM . . . INCREASE FIRST STEP SIZE')
0226          DELXO=2.0*DEX(1)
0227          YO=ELAST
0228          NTRY=0
0229          NOXO=NOXO+1
0230          IF(NOXO.LT.50) GO TO 169
0231          GO TO 971
0232      955 IF(NTRY.GT.25) WRITE(6,960) NTRY,AX,AY,AYD,L,VFIELD,YO,YDO,OEA
0233      960 FORMAT('-**AFTER',I4,' ITERATIONS, E*V DID NOT CONVERGE ... LAST V
             1ALUES WERE:',/,'     X=',E11.4,9X,' Y=',E11.4,'    YDOT=',E11.4,
             2'     L=',I4,/,'          VFIELD=',F8.3,' KV       YO=',E11.4,'    YDOTO
             3=',E11.4,'      OEA=',E11.4)
0234          VALUE=VALUE+0.020
0235          IF(VALUE.LE.0.10) GO TO 163
0236          IF(ABS(AY/YO).LE.VALUE.AND.(NTRY.GT.25.OR.DELYO/YO.LT.SLOPE))
             1WRITE(6,962)
0237      962 FORMAT('0>>>>>> POTENTIAL IS SMALL ENOUGH IN ABSOLUTE VALUE TO CON
             1SIDER SOLUTION CONVERGED')
0238          IF(ABS(AY/YO).LE.VALUE) GO TO 502
0239          GO TO 970
0240      965 WRITE(6,968) L, V(L), VFIELD
0241      968 FORMAT(' =>=>=> ABS(TK*V(L)) > 174.6 .... THERE WOULD HAVE BEEN AN
             1 OVERFLOW OR UNDERFLOW',/,' =>=>=> V(',I4,') = ',E11.4,/,' =>=>=>
             2VFIELD =',F8.3,' KILOVOLTS')
```

```
0242          970 CONTINUE
0243              IF(.NOT.ERROR) GO TO 971
0244              MISS=MISS+1
0245              IF(MISS.LE.2.AND.ABS(VFIELD).GT.1.E-5) GO TO 171
0246          971 CONTINUE
        C   *
        C *** THIS REMOVES UNPHYSICAL BUMPS AND WIGGLES IN G(E) THAT MIGHT APPEAR
        C   *
0247              NORI=IRON
0248              IF(INALT.EQ.1) NORI=MAXO(IRON,3)
0249              IF(INALT.EQ.2.AND.NALTER.GE.3) NORI=MAXO(IRON,2)
0250              DO 972 NN=1,NTOT
0251                 DUNSE(NN)=DENSE(NN)
0252                 IF(DTEMP(NN).LT.3.E15) DTEMP(NN)=3.E15
0253          972    IF(DTEMP(NN).GT.3.E21) DTEMP(NN)=3.E21
0254              DO 974 NN=1,NTOT
0255                 IRONY=1+2*MINO(NN-1,NTOT-NN,NORI)
0256                 DLOG=0.0
0257                 DO 973 I=1,IRONY
0258                    IADD=-(IRONY-1)/2+I-1
0259          973       DLOG=DLOG+ALOG(DTEMP(NN+IADD))/FLOAT(IRONY)
0260          974    DENSE(NN)=EXP(DLOG)
0261          980 IF(.NOT.PLOTS) GO TO 985
        C   *
        C *** PLOT LOG SIGMA (CONDUCTANCE) AGAINST VFIELD (APPLIED FIELD VOLTAGE)
        C *** AND ALSO AGAINST VCALC (CALCULATED VFIELD) ON SAME GRAPH
        C   *
0262              WRITE(6,983) TITLE, INALT, NALTER
0263          983 FORMAT('1',25X,'PLOT OF CONDUCTANCE IN MHO VERSUS APPLIED FIELD VO
                 1LTAGE IN KILOVOLTS',/,'O    ',20A4,/,'   TRIAL #',I2,' OF',I2,' FOR
                 2 G(E)')
0264              CALL PLOT1(NSCALE,6,8,5,20)
0265              CALL PLOT2(GRAPH,4.00,-4.0,YMAX,YMIN)
0266              CALL PLOT3('O',SIGMA,VCALC,50)
0267              CALL PLOT3('*',SIGMA,VDATA,50)
0268              CALL PLOT4(21,'APPLIED FIELD VOLTAGE')
0269              WRITE(6,984)
0270          984 FORMAT('O',55X,'LOG OF CONDUCTANCE',/,'O      *:  V-APPLIED
                 1   O:  V-CALCULATED')
0271          985 CONTINUE
0272              DO 987 I=1,NDATA
0273          987    SLAST(I)=SCALC(I)
0274              WRITE(6,995) AVEOFF
0275          995 FORMAT('-',/,'-==>==>==> AVERAGE OF ABS(LN(SIGMA-CALCULATED / SIGM
                 1A-DATA)) IS',F7.3)
0276              IF(INALT.GE.NALTER.OR.ABS(AVEOFF).LE..05) GO TO 100
0277              WRITE(6,112) NTOT
0278              GO TO 121
```

```
0279           999 STOP
0280               END
```

DEON

```
0001               FUNCTION DEON(X,Y,YD)
0002               DIMENSION RHO(200),EN(200),ROW(3000)
0003               COMMON/CHARGE/RHO,EN,NTOT,DELE,L,ROW,ESAM,ESUB
0004               DO 400 J=2,NTOT
0005                  IF(Y.LE.EN(J)) GO TO 450
0006           400    CONTINUE
0007           450 ROW(L)=RHO(J-1)+(RHO(J)-RHO(J-1))*(Y-EN(J-1))/DELE
0008               DEON=(1.8096E-6)*ROW(L)/ESAM
             C *** 1.8096E-6 = (4*PI*E*E)*(1. EV/1.602E-12 ERGS)
0009               RETURN
0010               END
```